Structural, electronic and optical properties of group-IV honeycomb crystals from first principles

Dissertation

zur Erlangung des akademischen Grades

doctor rerum naturalium (Dr. rer. nat.)

seit 1558

vorgelegt dem Rat der Physikalisch-Astronomischen Fakultät

der Friedrich-Schiller-Universität Jena

von Dipl.-Phys. Lars Matthes

geboren am 17.02.1986 in Zwickau

Gutachter:

1. Prof. Dr. sc. nat. Friedhelm Bechstedt (Friedrich-Schiller-Universität Jena)

2. Prof. Dr. rer. nat. Thomas Heine (Jacobs University Bremen)

3. Prof. Dr. rer. nat. Lara Kühl Teles (Instituto Tecnológico de Aeronáutica, São Paulo)

Tag der Disputation: 2. Juni 2015

I have yet to see any problem, however complicated, which, when you looked at it in the right way, did not become still more complicated.

Poul Anderson

Contents

Preface

Nature has always been inspiration and resource for new technical developments that otherwise would not have been possible. Taking a close look at almost every aspect of daily life and technology it is obvious that, even nowadays, most of the materials are based on natural occurring raw materials and concepts. The rise of quantum mechanics, which is the theory of objects compared to the size of atoms, allowed an in-depth understanding of the physical properties of materials, and also paved the way for optimized or even tailored properties of specific technological applications.

The naturally occurring graphite is a highly anisotropic allotrope of carbon. It is built from stratified atomically thin layers of carbon atoms, which are strongly bonded in a honeycomb lattice within each layer. In contrast, the bonding between the layers is only weak due to van der Waals interactions. The theoretical study of the electronic properties of graphite was initiated by *Wallace* back in the 1940s [1]. Surprisingly, the calculations also revealed remarkable electronic properties of single layer graphite, which was later called graphene. In particular, it was shown that due to the hexagonal symmetry of the carbon atoms within the layer the valence electrons resemble the linear dispersion of massless particles, which led to a strong interest in this material. The first known extraction of a graphene layer has been achieved in 1962 by *Boehm* [2], but the reliable production is possible only since 2004 due to *Geim* and coworkers [3–6]. For this achievement, *Andre Geim* and *Konstantin Novoselov* have been granted the Nobel prize of physics in 2010. Indeed, very recently the large-scale production of graphene by shear-exfoliation has begun [7].

Since graphene is broadly available, manifold developments and predictions have been made for this new "wonder material". It is well known that the massless valence electrons propagate with a finite (Fermi-) velocity of about 300 times smaller than the speed of light [8–10]. The electronic bandgap between electrons and holes as well as the density of states vanishes at the Fermi level, which makes graphene a zero-gap semiconductor. Consequently, graphene can be considered as an analog to ultrafast spin-1/2-particles observed in a solid-state system. Since the speed of the electrons is comparably low, predictions of high-energy physics can be studied in a material that is now easily accessible. Among them are, e.g., minimal conductivity [4], Zitterbewegung [11], universal optical

absorbance [12–16], and perfect transmission of carriers at normal incidence through a potential barrier, called the Klein paradox [17–19]. For graphene a very high electron mobility of about 200 times higher than in bulk-diamond structure silicon has been predicted [6] and consequently, its usefulness as a very fast switch in a transistor has been demonstrated [20], which is about three orders of magnitude higher than currently available switches based on bulk silicon. Recently, the research on graphene has been heavily supported by one of the flagships of European research, funded with one billion euro for the next ten years [21], which shows the huge interest in this new material.

By all advantages of graphene mentioned so far, there are of course also fundamental problems [22]. Even if graphene can be produced on the large scale, all common technology today is based on silicon. The integration of carbon-based electronics into silicon-based circuits is challenging due to deviations of the lattice constants and electronegativities [17]. For that reason silicene, the silicon-based analog of graphene, which does not exist in nature, has been suggested theoretically [23, 24] and experimentally realized as adsorbate layer [25, 26]. It has been shown that the structural and electronic properties of silicene are very similar to that of graphene, in particular the appearance of massless electrons. The first experimental realization of silicene or at least a monolayer of silicon with hexagonal symmetry on Ag(111) has been achieved by *Vogt* and coworkers in 2012 [25]. However, the strong interaction with the silver surface results in structural distortions of the honeycomb lattice and consequently, the disappearance of massless Dirac fermions in the silicon layer. The fabrication of freestanding silicene or at least silicene with weak substrate interactions is still an open quest and subject of intense research.

The experimental realization of graphene and silicene has initiated work on the entire field of two-dimensional (2D) crystals like the elemental crystals germanene and stanene (also called tinene) as well as many compounds like boron nitride (BN), molybdenum disulfide (MoS_2) or SiGe alloys. In particular stanene, the tin-based analog to graphene and silicene, has attracted attention due to the predicted appearance of a new state of matter at its one-dimensional edges, called topological edge states [27]. These edge states are relevant for the realization of the quantum spin Hall effect [28–30].

In this work we mainly focus on the elemental 2D group-IV honeycomb crystals graphene, silicene, germanene and stanene (or tinene). Starting from a general treatment based on parameter-free first-principles methods in the framework of density functional theory (DFT) [31–34] the structural properties for all freestanding group-IV honeycomb crystals are determined on equal footing. Under ambient conditions, silicon, germanium and tin tend to form sp^3 bonds in crystals instead of planar sp^2 bonds as carbon atoms in graphite. Hence, we study the formation of covalent bonds in the associated 2D honeycomb crystals

and their impact on lattice constants and bond angles, which give rise to buckled structures with a broken sp^2 hybridization.

The electronic ground-state properties are investigated by means of the electronic band structure and compared to available experiments on graphene and silicene. A reliable description of the electronic band structure in agreement with experiments also requires an improved description of the complex many-body electron-electron interaction. Hence, quasiparticle effects are approximately taken into account by means of the nonlocal exchange-correlation hybrid functional HSE06 [35–39]. In particular for the heavier elements Si, Ge and Sn the increasing impact of spin-orbit coupling (SOC) on the electronic band structure is incorporated into the theory. Without SOC all group-IV honeycomb crystals are rendered as zero-gap semiconductors like graphene, however, SOC opens a bandgap turning these crystals into insulators.

According to *Fu* and *Kane* all insulators in two and three dimensions can be classified into trivial and topological ones by means of a $\mathbb{Z}_2$ topological index [40, 41]. The 2D group-IV honeycomb crystals silicene, germanene and stanene are also examined with regard to their topological character and identified as topological insulators within the DFT. We investigate the topological phase transition to a trivial insulator due to an applied external electric field perpendicular to the sheet plane as predicted by simpler model calculations [42]. Since theory predicts topologically nontrivial edge states in topological insulators [42, 43], we further investigate exemplarily the edge states of germanene nanoribbons.

Particularly interesting is also the optical absorption of the two-dimensional group-IV honeycomb crystals. Experiments by the group of *Geim* revealed a comparable high absorbance of $A = 2.3$ % of graphene in a broad frequency range up to infrared light [44]. Based on a model, this value has also been determined theoretically and revealed a surprising connection to the Sommerfeld fine-structure constant α via the formula $A = \pi\alpha$. The main focus of this work is the accurate description of the frequency-dependent reflection, transmission and absorption of the 2D group-IV honeycomb crystals in order to explain and extend the observations of the universal infrared absorbance in graphene over the entire optical spectra. For that reason, the complex optical conductivity of the sheet crystal over the entire frequency axis is computed beyond the common Dirac cone approximation. As a benchmark the infrared absorption of graphene is determined numerically with remarkable accuracy and compared to experiments and analytical calculations. Besides the optical infrared absorption, the numerical treatment also allows an accurate description of the frequency dependent reflection, transmission and absorption of such 2D crystals at arbitrary angles of incidence and polarization of the incident light. We address the question how atomically thin 2D crystals are incorporated in the theory of classical electrodynamics.

Thereby, we also explore in detail the limit beyond the description as infinitely thin 2D sheet crystals commonly applied in literature and support our findings with numerical and analytical calculations.

The problem of the 2D group-IV honeycomb crystals is their preparation, which is usually achieved by deposition on a substrate [25, 45–47]. While the majority of results are presented for freestanding 2D sheet crystals we also address the possible impact of metallic and insulating substrates. Therefore, we provide detailed insights in the interaction between the substrate and the overlayer, for which we consider silicene due to recent experimental progress. Based on these findings, we also investigate several new substrates for the growth of silicene with the goal, that even in the presence of a substrate the 2D sheet crystal may be treated as basically freestanding. The calculations are based on total-energy DFT calculations including van der Waals interactions.

Chapter 1

Many-body theory

1.1 Many-electron problem

Solids are composed of electrons and ions interacting with each other. Neglecting relativistic effects, the full many-body Hamiltonian of electrons and ions mutually interacting can be written as [32, 48]

$$\hat{H} = \sum_i \frac{\boldsymbol{p}_i^2}{2m} + \sum_I \frac{\boldsymbol{P}_I^2}{2M_I} - \sum_{i,I} \frac{Z_I e^2}{|\boldsymbol{r}_i - \boldsymbol{R}_I|} + \frac{1}{2} \sum_{i \neq j} \frac{e^2}{|\boldsymbol{r}_i - \boldsymbol{r}_j|} + \frac{1}{2} \sum_{I \neq J} \frac{Z_I Z_J e^2}{|\boldsymbol{R}_I - \boldsymbol{R}_J|}, \quad (1.1)$$

where the cgs system of units (e.g. $4\pi\epsilon_0 \equiv 1$ to characterize charges) is used here and throughout this work. In this equation ions at positions $\boldsymbol{R}_I$ carry momenta $\boldsymbol{P}_I$ and charge $+Z_I e$ whereas electrons at coordinates $\boldsymbol{r}_i$ carry momenta $\boldsymbol{p}_i$ and charge $-e$. The first two terms refer to the kinetic energy of the electrons and ions, respectively. The third, fourth end fifth term denotes the electron-ion, electron-electron and ion-ion interactions. The ground state of the system can be obtained by minimizing the total energy given by the expectation value of Hamiltonian (1.1) with respect to the electronic and ionic degrees of freedom. However, the practical computation is not possible for realistic systems.

The first obvious fact that can be exploited for the simplification of the problem is suggested by the large difference between electron and ion masses of about three orders of magnitude. It can be assumed, that the electrons are moving much faster than the ions and follow their movement more or less instantaneously. This so-called Born-Oppenheimer approximation effectively decouples the ionic and electronic degrees of freedom. The ionic positions $\boldsymbol{R}_I$ become classical variables and can be considered fixed. Consequently, the kinetic energy of the ions in Eq. (1.1) can be safely neglected. In this regard the last term in Eq. (1.1) is a constant for any fixed configuration of ions and does not influence the electronic states and can be neglected as well. It is, however, needed to determine the correct total energy of

moving electrons and fixed ions. The many-body Hamiltonian of N interacting electrons in a solid can finally be written in the form

$$\hat{H} = \sum_i \frac{\boldsymbol{p}_i^2}{2m} - \sum_{i,I} \frac{Z_I e^2}{|\boldsymbol{r}_i - \boldsymbol{R}_I|} + \frac{1}{2} \sum_{i \neq j} \frac{e^2}{|\boldsymbol{r}_i - \boldsymbol{r}_j|} = T + \sum_i V_{\text{nucl}}(\boldsymbol{r}_i) + V_{\text{e-e}}, \qquad (1.2)$$

$$T = \sum_i \frac{\boldsymbol{p}_i^2}{2m}, \qquad V_{\text{nucl}}(\boldsymbol{r}_i) = -\sum_I \frac{Z_I e^2}{|\boldsymbol{r}_i - \boldsymbol{R}_I|}, \qquad V_{\text{e-e}} = \frac{1}{2} \sum_{i \neq j} \frac{e^2}{|\boldsymbol{r}_i - \boldsymbol{r}_j|}. \qquad (1.3)$$

The solution of this problem is still a demanding task. An approach to solve the eigenvalue problem for the Hamiltonian (1.2) for the ground-state of the electrons is the Hartree theory, where the N-electron ground-state wave function is represented by the best product of N one-electron spin-orbitals. However, the product wave functions do not take into account the correct antisymmetry character of space and spin coordinates and neglects any correlation of the electrons [48]. A better approach is discussed in the next section.

1.2 Hartree-Fock theory

In the Hartree-Fock theory the ground state $\boldsymbol{\Psi}_0$ of a non-relativistic N-electron system described by Hamiltonian (1.2) is approximated by the best single determinantal state (Slater determinant)

$$\boldsymbol{\Psi}_0(\boldsymbol{r}_1\sigma_1 \ldots \boldsymbol{r}_N\sigma_N) = \frac{1}{\sqrt{N!}} \begin{vmatrix} \psi_1(\boldsymbol{r}_1\sigma_1) & \cdots & \psi_1(\boldsymbol{r}_N\sigma_N) \\ \vdots & \ddots & \vdots \\ \psi_N(\boldsymbol{r}_1\sigma_1) & \cdots & \psi_N(\boldsymbol{r}_N\sigma_N) \end{vmatrix}. \qquad (1.4)$$

According to a variational principle, the "best" N-electron wave function is obtained by minimizing the total energy $E_0 = \langle \boldsymbol{\Psi}_0 | \hat{H} | \boldsymbol{\Psi}_0 \rangle$ at the ground state with respect to the contributing single-particle Pauli spinors ψ_i $(i = 1, \ldots, N)$ and under the constraint, that the Pauli-spinors ψ_i are orthonormal $\langle \psi_i | \psi_j \rangle = \delta_{ij}$. The constraint introduces Lagrange multipliers ε_i into the functional that has to be minimized. The resulting system of non-linear integro-differential equations to determine ψ_i are the canonical Hartree-Fock equations

$$\left[\frac{\boldsymbol{p}^2}{2m} + V_{\text{nucl}}(\boldsymbol{r}) + V_{\text{coul}}(\boldsymbol{r}) + V_{\text{exch}} \right] \psi_i = \varepsilon_i \psi_i \qquad (1.5)$$

with the Coulomb term

$$V_{\text{coul}} \psi_i(\boldsymbol{r}\sigma) = \sum_j^{(\text{occ})} \psi_i(\boldsymbol{r}\sigma) \int \psi_j^*(\boldsymbol{r}_2\sigma_2) \frac{e^2}{|\boldsymbol{r} - \boldsymbol{r}_2|} \psi_j(\boldsymbol{r}_2\sigma_2) \, d(\boldsymbol{r}_2\sigma_2) \qquad (1.6)$$

and exchange contribution

$$V_{\text{exch}}\psi_i(\boldsymbol{r}\sigma) = -\sum_j^{(\text{occ})} \psi_j(\boldsymbol{r}\sigma) \int \psi_j^*(\boldsymbol{r}_2\sigma_2) \frac{e^2}{|\boldsymbol{r}-\boldsymbol{r}_2|} \psi_i(\boldsymbol{r}_2\sigma_2)\, d(\boldsymbol{r}_2\sigma_2)\,. \qquad (1.7)$$

In the latter term the exchange potential is a non-local integral operator since the wave function on which it acts appears under the integral. The solutions ψ_i and corresponding eigenvalues ε_i of Eq. (1.5) must be determined self-consistently. Most importantly, the many-body ground state problem has been traced back to a single-particle problem. However, although Eq. (1.5) appears as a classical Schrödinger equation, special care must be taken about the connection between the eigenstates and eigenenergies of the many-electron system under investigation and the auxiliary wave functions and energies (=Lagrange multipliers) incorporated in the Hartree-Fock equations (1.5). Koopmans' theorem [49] at least reveals the connection between the physical meaning of the single-particle excitation energies of the many-electron system and the Hartree-Fock eigenenergies.

In agreement with the variational principle it is clear, that the Hartree-Fock energy E_0 is always higher than the exact ground-state energy of the system. The difference is due to correlation effects. The representation of the many-body wave function (1.4) as a single Slater determinantal state is only a poor representation of the complex many-body wave function. The correlation energy can be calculated essentially exactly by configuration interaction methods where the exact ground state is expanded in a weighted sum of Slater determinants built from spin orbitals [50]. However, in practice the computational effort is very high even for atoms or small molecules. Another drawback becomes apparent if the integration over the spin degrees of freedom is taken in the exchange operator. The only contributions to the exchange energy are due to spin orientation parallel to $\psi_i(\boldsymbol{r}\sigma)$. It can be concluded, that in the Hartree-Fock equations the depletion of parallel spin particles is nearly correctly taken into account. The main issue of the Hartree-Fock approach is that electrons with opposite spin remain uncorrelated.

In the next section we will see, that density functional theory allows us or the ground state to take into account also correlation effects in principle exactly.

1.3 Density functional theory

It has been shown in the previous section that the ground state of a many-electron system can be tackled by means of a Slater determinant. If the ground state wave function is known for a given atomic configuration the ground state properties are easily derived as

expectation values of the corresponding quantum mechanical operators representing an observable. The main aspect of density functional theory (DFT) is a dramatic change of view. It is stated, that the ground state energy of the many-body system is a functional of the ground state density of the system. Since the density is a scalar function of the position in principle a tremendous simplification of the many-electron problem can be achieved. However, the construction of the appropriate exchange-correlation functional is still part of ongoing research and only approximations are known up to date. Despite some seemingly rough assumptions in its derivation, the success of DFT in predicting ground-state properties such as atomic geometries is remarkable and for many molecular and solid-state systems it has been proven to be in good agreement with experiments. Thus, nowadays DFT is the state-of-the-art method for the prediction of structural, elastic and thermodynamic properties of materials.

1.3.1 Hohenberg-Kohn theorem

The Hohenberg-Kohn theorem (HKT) is the core statement of the DFT. For its formulation it is useful to decompose the many-body Hamiltonian (1.2) in internal and external contributions

$$\hat{H} = \hat{H}_{\text{int}} + \hat{V}_{\text{ext}} \tag{1.8}$$

where

$$\hat{H}_{\text{int}} = \hat{T} + \hat{V}_{\text{e-e}} \;\text{ and }\; \hat{V}_{\text{ext}}(\boldsymbol{r}) = \sum_i v_{\text{ext}}(\boldsymbol{r}_i), \qquad v_{\text{ext}}(\boldsymbol{r}) \equiv V_{\text{nucl}}(\boldsymbol{r}) \,. \tag{1.9}$$

In the work of Hohenberg and Kohn [51] it was shown that the knowledge of the external potential V_{ext} determines exactly the ground-state density $n(\boldsymbol{r})$ of the system. Here 'external' means that the potential does not depend on electron coordinates but, e.g., may depend on atomic coordinates. For that reason $\hat{V}_{\text{nucl}}$ can be replaced by v_{ext}. The proof of this rather trivial statement can be found in the original paper or in standard literature about DFT [32, 48, 52]. More precisely, there exists a functional that links the external potential to the ground-state density of the system. Surprisingly, in the same work it was also claimed that the knowledge of the ground-state density determines uniquely (to within a constant) the external potential v_{ext}, and consequently, the full Hamiltonian of the system. If the Hamiltonian was known, its eigenenergies and eigenfunctions are the solutions of the many-electron problem. Of course, the ground-state density is not known a-priori, but a variational principle can be formulated which allows for the self-consistent calculation of the ground-state density. It is important to note, that e.g. the total energy of the system in its ground state is determined by the external potential mediated by a functional. Due to the HKT, this functional depends on the ground-state density of the

system. Thus, the Hohenberg-Kohn functional of the ground-state energy in general has the following form

$$E^{(\text{HK})}[n(\boldsymbol{r}), v_{\text{ext}}(\boldsymbol{r})] = \langle \Psi_0[n] | \hat{T} + \hat{V}_{\text{e-e}} + \hat{V}_{\text{ext}} | \Psi_0[n] \rangle \, , \tag{1.10}$$

which can be rewritten in the form

$$E^{(\text{HK})}[n(\boldsymbol{r}), v_{\text{ext}}(\boldsymbol{r})] = T[n(\boldsymbol{r})] + V_{\text{e-e}}[n(\boldsymbol{r})] + \int v_{\text{ext}}(\boldsymbol{r}) n(\boldsymbol{r}) d\boldsymbol{r} \, . \tag{1.11}$$

This functional exists and is unique thanks to the HKT and takes its minimum at the exact ground-state density $n(\boldsymbol{r})$ leading to the ground-state energy. The ansatz of Kohn and Sham [53] assumes that the ground-state density of the original interacting system is equal to that of some chosen system of non-interacting particles. This leads to independent-particle equations for the non-interacting system that can be considered exactly soluble with all the difficult many-body terms incorporated into an exchange-correlation functional of the density.

Following the idea of Kohn and Sham the electron density can be decomposed in a complete system of orthonormal orbitals $|\phi_i\rangle$

$$n(\boldsymbol{r}) = \sum_i f_i \phi_i^*(\boldsymbol{r}) \phi_i(\boldsymbol{r}) \, , \tag{1.12}$$

where f_i is the occupation number of the corresponding state (the spin degree of freedom is not yet included). The first two terms depend on the ground-state density of the interacting system. It is reasonable to assume that the kinetic energy of a noninteracting electron gas is already a good approximation for that of the fully interacting system. And it is also reasonable to to assume that $V_{\text{e-e}}$ is already well represented by the classical Coulomb interaction. It is therefore common to rewrite Eq. (1.11) into the form

$$E^{(\text{HK})}[n(\boldsymbol{r}), v_{\text{ext}}(\boldsymbol{r})] = T_0[n(\boldsymbol{r})] + E_{\text{H}}[n(\boldsymbol{r})] + \int v_{\text{ext}}(\boldsymbol{r}) n(\boldsymbol{r}) d\boldsymbol{r} + E_{\text{XC}}[n(\boldsymbol{r})] \, . \tag{1.13}$$

with the functional of the kinetic energy of a non-interacting electron system of the same density $n(\boldsymbol{r})$

$$T_0[n(\boldsymbol{r})] = \sum_i \langle \phi_i | - \frac{\hbar^2 \nabla^2}{2m} | \phi_i \rangle \tag{1.14}$$

and the classical long-range Hartree-energy

$$E_{\text{H}}[n(\boldsymbol{r})] = \frac{1}{2} \int n(\boldsymbol{r}) \frac{e^2}{|\boldsymbol{r} - \boldsymbol{r}'|} n(\boldsymbol{r}') d\boldsymbol{r} d\boldsymbol{r}' = \frac{1}{2} \sum_{ij} \langle \phi_i \phi_j | \frac{e^2}{|\boldsymbol{r}_i - \boldsymbol{r}_j|} | \phi_i \phi_j \rangle \, . \tag{1.15}$$

The last remaining term in Eq. (1.13) includes all interaction terms between the electrons of the fully interacting system and is called the exchange-correlation functional

$$E_{\mathrm{XC}}[n(\boldsymbol{r})] = T[n(\boldsymbol{r})] - T_0[n(\boldsymbol{r})] + V_{\mathrm{e\text{-}e}}[n(\boldsymbol{r})] - E_{\mathrm{H}}[n(\boldsymbol{r})]. \tag{1.16}$$

While T_0 and E_{H} are given by exact expressions, E_{XC} is unknown and may be understood as the error made by approximating the fully interacting system as a Hartree-Fock system as mentioned before. Moreover, E_{XC} becomes a relatively small part of the total energy. Since the long-range Hartree potential is already separated out from the XC potential, it can mostly be well approximated as local or nearly-local functional. If the standard variational procedure is applied to Eq. (1.13) with respect to the orbitals ϕ_i the Kohn-Sham equations [53] are obtained

$$\left[-\frac{\hbar^2 \nabla^2}{2m} + V_{\mathrm{nucl}}(\boldsymbol{r}) + V_{\mathrm{coul}}(\boldsymbol{r}) + V_{\mathrm{XC}}(\boldsymbol{r}) \right] \phi_i(\boldsymbol{r}) = \varepsilon_i \phi_i(\boldsymbol{r}) \tag{1.17}$$

where V_{XC} is the functional derivative of $E_{\mathrm{XC}}[n(\boldsymbol{r})]$ with respect to the density

$$\delta E_{\mathrm{XC}}[n(\boldsymbol{r})] = \int V_{\mathrm{XC}}(\boldsymbol{r}) \delta n(\boldsymbol{r}) d\boldsymbol{r}. \tag{1.18}$$

The equation reveals that instead of dealing with the fully interacting system, the electrons can be viewed as independent particles moving in an effective potential

$$V_{\mathrm{eff}}(\boldsymbol{r}) = V_{\mathrm{nucl}}(\boldsymbol{r}) + V_{\mathrm{coul}}(\boldsymbol{r}) + V_{\mathrm{XC}}(\boldsymbol{r}). \tag{1.19}$$

The original many-electron problem has been replaced by an auxiliary single-particle problem. All issues related to the complex many-electron problem are left to the determination of a reasonable XC potential V_{XC} or finding E_{XC}. The next section gives an overview over some of the most common approaches for the approximation of V_{XC} or E_{XC}.

1.3.2 Local (spin) density approximation (L(S)DA) and generalized gradient approximation (GGA)

In general the XC energy functional in nonlocal, however, it is reasonable to approximate it as a local functional, since the long-range Hartree potential has been separated. Therefore, the easiest approach is to assume that the XC-energy density at each point is the same as for the homogeneous electron gas of the same density, which is famous the local density

approximation (LDA)

$$E_{\mathrm{XC}}^{\mathrm{LDA}}[n(\boldsymbol{r})] = \int \epsilon_{\mathrm{XC}}^{\mathrm{hom}}[n(\boldsymbol{r})]n(\boldsymbol{r})d\boldsymbol{r}\,, \qquad (1.20)$$

where $\epsilon_{\mathrm{XC}}^{\mathrm{hom}}[n(\boldsymbol{r})]$ is the XC energy density per particle for an electron density n. The exchange-correlation energy for the homogeneous electron gas at various densities can be obtained with very high precision by numerical Monte-Carlo simulations (see Ceperly and Alder [54]). Their results have been parametrized by e.g. Perdew and Zunger [55] and are widely used in numerical DFT programs. It must be noted, that in LDA the XC-energy density is split into a sum of contributions of exchange and correlation $\epsilon_{\mathrm{XC}} = \epsilon_{\mathrm{X}} + \epsilon_{\mathrm{C}}$. In the previous discussion spin has not been considered. In a collinearly spin-polarized system the XC energy is a functional of spin-up and spin-down densities, i.e., $E_{\mathrm{XC}}(n_\uparrow(\boldsymbol{r}), n_\downarrow(\boldsymbol{r}))$. Within the local spin-density approximation (LSDA) the XC energy density is taken from the polarized homogeneous electron gas. The Kohn-Sham equations (1.17) become a pair of equations

$$\left[-\frac{\hbar^2 \nabla^2}{2m} + V_{\mathrm{nucl}}(\boldsymbol{r}) + V_{\mathrm{coul}}(\boldsymbol{r}) + V_{\mathrm{XC}}^{\sigma}(\boldsymbol{r}) \right] \phi_{i\sigma}(\boldsymbol{r}) = \varepsilon_{i\sigma}\phi_{i\sigma}(\boldsymbol{r}) \qquad (1.21)$$

for each spin polarization $\sigma = \uparrow, \downarrow$. Although its rather crude approximations, the usefulness of L(S)DA has been proven in particular for systems with slowly varying density. Therefore, there has been much effort spent in the improvement of the LDA functional.

The first obvious approach is the inclusion of powers of the gradient of the density by means of an expansion of the XC functional of the homogeneous electron gas and by fulfilling certain sum rules. The generalized-gradient approximation (GGA) denotes a variety of such functionals, which are also called semilocal approximations due to the inclusion of gradients. The most widely used functional is the one proposed by Perdew, Burke and Ernzerhof [56] known as the PBE functional, which will also be used in this work and which has further importance for the development of functionals including quasi-particle corrections. The functional form of the XC energy functional incorporates dimensionless enhancement factors $F_{\mathrm{X}}(n(\boldsymbol{r}), \nabla n(\boldsymbol{r}))$ and $F_{\mathrm{C}}(n(\boldsymbol{r}), \nabla n(\boldsymbol{r}))$

$$E_{\mathrm{XC}}^{\mathrm{GGA}}[n(\boldsymbol{r})] = \int \left(\epsilon_{\mathrm{X}}^{\mathrm{hom}}[n(\boldsymbol{r})]F_{\mathrm{X}}[n(\boldsymbol{r}), \nabla n(\boldsymbol{r})] + \epsilon_{\mathrm{C}}^{\mathrm{hom}}[n(\boldsymbol{r})]F_{\mathrm{C}}[n(\boldsymbol{r}), \nabla n(\boldsymbol{r})] \right) d\boldsymbol{r}\,. \quad (1.22)$$

It is well known that binding energies in LDA are typically too large and bond lengths are 1-2% too short compared to experimental values. On the other hand, GGA corrects this error but predicts binding energies which are smaller and, thus, bond lengths are slightly too large compared to experiments, but the overall agreement is much better than for LDA. Electronic properties like the band dispersion and bandgaps are very similar,

however not described correctly within both approximations. The apparent reason is that in particular bandgaps are not ground-state properties of the system. It can be only measured by exciting the electron system. Compared to the Hartree-Fock approach LDA and GGA in general yield a good description of chemical bonds, where GGA works even better for e.g. ionic systems, surfaces, interfaces and whenever large density gradients appear or are expected. Further improvement based on the optimization of parameters used in the PBE functional has been given by Zhang et *al.* [57], known as the revPBE functional, where "rev" simply stands for "revised". Systems which are only kept together by intermediate-range interactions like water (hydrogen-bridge bonds), graphite (interlayer van der Waals bonding) or rare gas dimers (van der Waals bonding) are only poorly described.

1.3.3 Non-collinear magnetization and spin-orbit interaction

The Kohn-Sham equations can be generalized to include the effect of non-collinear magnetization and the coupling between spin and orbital moments starting from the Dirac-equation [58]. Spin-orbit coupling (SOC) effectively couples the spin to the gradient of the crystal potential leading to new understanding of magnetism in solids, like the magnetocrystalline anisotropy [59, 60].

Density functional theory including non-collinear magnetism is expressed in terms of a 2×2 density matrix (cf. the density introduced in (1.12)) with elements $n_{\alpha\beta}(\boldsymbol{r})$ $(\alpha, \beta = 1, 2)$ defined as [61–63]

$$n_{\alpha\beta}(\boldsymbol{r}) = \sum_i f_i \phi_{\alpha i}^*(\boldsymbol{r}) \phi_{\beta i}(\boldsymbol{r}) \,, \tag{1.23}$$

where the two $\phi_{\alpha i}(\boldsymbol{r})$ correspond to the components of the spinor $\Phi_i(\boldsymbol{r}) = (\phi_{1i}(\boldsymbol{r}), \phi_{2i}(\boldsymbol{r}))$ of the i-th state with occupation number f_i. The electron density $n(\boldsymbol{r})$ determined from the diagonal elements of the density matrix by means of

$$Tr[n_{\alpha\beta}(\boldsymbol{r})] \equiv n(\boldsymbol{r}) = \sum_\alpha n_{\alpha\alpha}(\boldsymbol{r}) \,, \tag{1.24}$$

whereas the magnetization density $\boldsymbol{m}(\boldsymbol{r})$ can be obtained from the off-diagonal elements of the density matrix. In terms of the Pauli spin matrices $\boldsymbol{\sigma} = (\sigma_x, \sigma_y, \sigma_z)$ the density matrix (1.23) reads

$$n_{\alpha\beta}(\boldsymbol{r}) = [n(\boldsymbol{r})\delta_{\alpha\beta} + \boldsymbol{m}(\boldsymbol{r}) \cdot \boldsymbol{\sigma}_{\alpha\beta}] / 2 \,. \tag{1.25}$$

The exact Kohn-Sham energy functional becomes

$$E = \sum_\alpha \sum_i f_i \langle \phi_{\alpha i} | \frac{\boldsymbol{p}^2}{2m} | \phi_{\alpha i} \rangle + E_{\mathrm{H}}[n(\boldsymbol{r})] + E_{\mathrm{XC}}[n(\boldsymbol{r}), |\boldsymbol{m}(\boldsymbol{r})|] . \tag{1.26}$$

The spin-orbit coupling stemming from the Dirac equation is added to the energy functional 1.26 according to Hobbs et *al.* [63]. Since SOC mostly affects the inner core electrons, it is evaluated only for the all-electron part of the wave functions within the PAW spheres (see Sec. 1.5) of the atoms.

1.3.4 Van der Waals corrections

The van der Waals interaction actually is an intermediate-range correlation effect, which is not captured in the short-range XC functionals discussed before. An improvement over the LDA and GGA approximations of XC in order to include also long-range correlation effects has been derived by Dion et *al.* [64], which nowadays belong to an entire group of van der Waals density functionals (vdW-DF). The key ingredient is the computation of a non-local long-range correlation-energy extension $E_{\mathrm{c}}^{\mathrm{nl}}$. It can be traced back to the random-phase approximation (RPA) of the correlation energy of the form

$$E_{\mathrm{c}}^{\mathrm{nl}} = \frac{1}{2} \int d^3\boldsymbol{r} d^3\boldsymbol{r}' n(\boldsymbol{r}) \Phi(\boldsymbol{r}, \boldsymbol{r}') n(\boldsymbol{r}') \tag{1.27}$$

and is added to the aforementioned DFT functionals, where $\Phi(\boldsymbol{r}, \boldsymbol{r}')$ is some functional (or kernel) depending on $\boldsymbol{r} - \boldsymbol{r}'$. It is possible to show that the remaining local-correlation part of the full XC functional is reasonable approximated within the LDA. The exchange-energy functional is approximated by that of the revPBE [57] functional. According to Dion et *al.* this choice is motivated by the observation, that a more standard GGA predicts substantial binding in rare gas dimers from exchange alone, a feature absent for exact Hartree-Fock exchange. It was shown that the optimization of the correlation part substantial improves the description of weakly-bonded systems. The numerical implementation of several vdW-DF functionals has become accessible due to the works of Soler et *al.* [65] and Klimeš et *al.* [66, 67]. In this work the vdW interaction will be included for the computation of silicene monolayers on metallic and nonmetallic substrates.

1.3.5 Hellmann-Feynman forces

Due to the Born-Oppenheimer approximation the ionic degrees of freedom in the many-body Hamiltonian are considered as classical variables. For a given atomic structure the

ground-state density and all properties can be calculated thanks to the Hohenberg-Kohn theorem and the methods introduced in the last sections. The lattice constant, atomic structure and symmetry of a crystal therefore has to be taken from experiments, which is of course a source of error in subsequent computations. Naturally the question arises if it is possible to determine also the exact atomic positions of a certain atomic geometry if only e.g. the composition of the crystal is known, or only approximate lattice constants are available?

It is obvious that the force on each ion in an arbitrary crystal in its ground state (at zero temperature) must vanish. If the force on an ion does not vanish, the ion will move until all acting forces disappear. The Hellmann-Feynman theorem allows the calculation of the forces acting on the ions if the ground-state electron density is known for this atomic (non-equilibrium) configuration. If the forces are known, the ions are slightly moved along the direction of the acting forces and the electronic ground state is determined again. The procedure is repeated until the forces vanish, which is equivalent to the equilibrium structure of the crystal. The force acting on an the ions is defined as the gradient of the total energy with respect to the ionic coordinates

$$\boldsymbol{F}_I = -\boldsymbol{\nabla}_{\boldsymbol{R}_I}(E + E_{\mathrm{II}}). \tag{1.28}$$

It follows from the total energy $E = \langle\Psi|\hat{H}|\Psi\rangle$ (with Hamiltonian (1.2) and adding the ion-ion repulsion energy E_{II}) that the forces can be calculated by means of [52]

$$\boldsymbol{F}_I = -\int d^3\boldsymbol{r}\, n(\boldsymbol{r})\boldsymbol{\nabla}_{\boldsymbol{R}_I} v_{\mathrm{ext}}(\boldsymbol{r}) - \boldsymbol{\nabla}_{\boldsymbol{R}_I} E_{\mathrm{II}}(\boldsymbol{r}), \tag{1.29}$$

where the last term is the classical contribution of the ion-ion interaction to the energy, which has been taken into account. The forces are given in terms of the charge density and thus, particularly useful in DFT calculations. Expression (1.29) goes back to the Hellmann-Feynman theorem, in practice, an additional term is taken into account, the so-called variational forces, which appear as long as the energetic minimum with respect to the electron density is not reached.

1.3.6 Hybrid functionals

For the solution of the many-electron problem two approaches have been presented, namely the Hartree-Fock approach and the DFT in local or semilocal approximation for XC or even including van der Waals interaction. Both of them have advantages and disadvantages which can be traced back to the different treatment of exchange and

correlation. Hartree-Fock theory provides an exact treatment of exchange, it scales well with molecular size and scales well even for large chemical systems [68]. On the other hand chemical bonding is not well described and correlation effects are not included. On the other hand, density functional theory takes also into account correlation effects which is moreover easily to calculate. Bonding of atoms is described very reliably in DFT. Therefore, there has been a strong interest in mixing Hartree-Fock with DFT for non-local correlation and, in the end, a more accurate description of atoms, molecules and solids.

The approach proposed by Becke [68] mixes the exact exchange of HF theory with the XC contribution of LSDA in the ratio 1:1, therefore it became popular as the half-and-half hybrid. However, the choice of the mixing ratio is arbitrary and not motivated by physical means. Perdew, Ernzerhof and Burke further investigated the mixing ratio by exploiting the coupling-constant method [35]. The mixing has been optimized with respect to the exchange part of the PBE functional. A mixing ratio of 1:3 as the most reasonable choice has been found:

$$E_{\text{XC}}^{\text{PBE0}} = \frac{1}{4} E_{\text{X}}^{\text{HF}} + \frac{3}{4} E_{\text{X}}^{\text{PBE}} + E_{\text{C}}^{\text{PBE}}. \tag{1.30}$$

The functional is known as PBE0 [36]. It has been used for the calculation of atomization energies of various molecules and led to a significant improvement towards the experimental values. Furthermore, even electronic bandgaps and widths are well described [35,36,69,70]. The bottleneck of the calculation is the slow convergence of the long-range nature of the HF exact exchange contribution in periodic systems in particular for metals due to the large number of $\boldsymbol{k}$ points required for the sampling of the Fermi surface.

Heyd *et al.* [37,39] proposed the decomposition of the exchange contribution into short and long-range components

$$E_{\text{XC}}^{\text{HSE06}} = \frac{1}{4} E_{\text{X}}^{\text{HF,sr}}(\mu) + \frac{3}{4} E_{\text{X}}^{\text{PBE,sr}}(\mu) + E_{\text{X}}^{\text{PBE,lr}}(\mu) + E_{\text{C}}^{\text{PBE}} \tag{1.31}$$

where a screened Coulomb potential is applied only to the exchange interaction in order to screen the long-range part of the HF exchange. Therefore, the division of the Coulomb potential in long- and short-range contributions is achieved by means of

$$\frac{1}{r} = \underbrace{\frac{1 - \text{erf}(\mu r)}{r}}_{\text{short range}} + \underbrace{\frac{\text{erf}(\mu r)}{r}}_{\text{long range}} \tag{1.32}$$

where $\text{erf}(x)$ denotes the Gaussian error function and μ is an adjustable parameter which can be interpreted as a Thomas-Fermi screening parameter. All other Coulomb interactions remain unscreened. The short-range part of HF is treated exactly based on the DFT wave functions, while the long-range part is treated by approximate DFT. The For $\mu = 0$

the PBE0 functional is recovered, whereas the PBE functional is recovered in the limit $\mu \to \infty$. An extensive study of the μ dependence of various properties showed only a slight dependence in a certain range [37]. In the original published work in 2003 the parameter $\mu = 0.15a_{\mathrm{B}}^{-1}$ (a_{B} denotes the Bohr radius) was suggested and the functional was named HSE03 for obvious reasons. This parameter has been used in many publications and many groups. However, in 2006 an erratum was published concerning this value. It was stated, that the original parameter used in the work of 2003 was $\mu = 0.15/\sqrt{2}\, a_{\mathrm{B}}^{-1}$ instead. In order to account for the correction the functional today is known as HSE06 [39]. Although the choice of μ does not change the results obtained by Heyd et *al.*, any publication that used one of the HSE functionals has to be checked precisely for which variant was used in order to reproduce their results.

Compared to the L(S)DA and GGA the HSE functional offers improved lattice constants and fundamental bandgaps toward experimental values [38, 71] for many mid-gap and some large gap insulators as displayed in Fig. 1.1. Although there is no reason why density
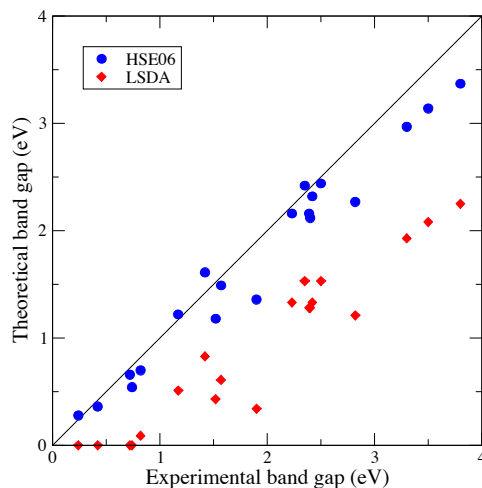
Figure 1.1: Comparison of experimental energy bandgaps of several semiconductors (SC40 solid test set [38]) within the LSDA and the hybrid functional HSE06 [71].

functional theory should provide accurate fundamental bandgaps the hybrid functionals are remarkably successful. It is stated that the non-locality of exchange and correlation present in the exact XC potential offers an improved description of the many-body wave function compared to (semi-)local DFT functionals, in particular in terms of their spatial localization. Fundamental bandgaps are determined experimentally based on a combination of angle-resolved photoemission spectroscopy (ARPES) and $\boldsymbol{k}$-resolved inverse photoemission spectroscopy (KRIPES [72]). However, electron removal leaves oppositely charged holes in the material which attract electrons and form quasiparticles. These charged excitations are obviously not a ground-state property. Typically, many-body perturbation

theory, e.g., within the GW approximation, take into account such quasiparticle effects, where the HSE06 wave functions and energies serve as a good starting point. However, since the HSE functional already performs well in the prediction of fundamental bandgaps it is claimed, that HSE partially covers such quasiparticle effects as well.

Optical absorption experiments create interacting electron-hole pairs, called excitons. Consequently, optical bandgaps are usually even smaller by about the exciton binding energies than the fundamental quasiparticle bandgaps. Excitons are well-described theoretically through the solution of the Bethe-Salpeter equations (BSE), which couples the electron and the hole. Excitons are particularly important in insulators. However, according to Louie et *al.* [73] and Pulci [74] excitonic effects give rise to a redshift of the optical absorption peaks, but the low-energy part of the spectrum is not affected. Therefore, excitonic effects are not taken into account.

A nice review and outlook of historical and recent developments of DFT can be found in the literature [33, 34].

1.4 Optical properties

The optical properties of matter are determined by the strength of the coupling of electromagnetic fields, e.g. light, to some kind of excitations in the material. Possible excitations are e.g. atomic vibrations, rotations or transitions between electronic states. The strength of the coupling strongly depends on the energy or wavelength of the photons. In this work we are mainly interested in the optical properties related to the infrared, visible, and ultraviolet electromagnetic spectrum and above, starting from the mid-infrared with an energy of about 25 meV up to 30 eV (strong ultra-violet). Usually low temperatures are investigated. Therefore, the complicated coupling to lattice vibrations will not be considered and the main focus lies on the transition between electronic states ruled by quantum mechanics.

In order to investigate the response of an electronic system to en external electromagnetic field one starts with a Hamiltonian of the underlying system and replace the momentum operator $\hat{\boldsymbol{p}}$ by the generalized momentum operator $\hat{\boldsymbol{p}} + \frac{e}{c}\hat{\boldsymbol{A}}(\boldsymbol{r}, t)$, where $\hat{\boldsymbol{A}}(\boldsymbol{r}, t)$ is the vector potential of the electromagnetic field in the Coulomb gauge div $\boldsymbol{A} = 0$, which is related to the electric field by means of $\boldsymbol{E} = -\frac{1}{c}\partial_t \boldsymbol{A}$. The probability, that an electron is transferred between two quantum mechanical states can be calculated by Fermi's golden rule (known from time-dependent perturbation theory) [48]. The electromagnetic field induces currents in the medium, thus, leading to energy dissipation. If we assume a linear

response of the medium to the applied field, the induced current $\boldsymbol{j}(\boldsymbol{r},t)$ depends linearly on the electric field (Ohm's law)

$$\boldsymbol{j}(\boldsymbol{r},t) = \int d\boldsymbol{r}'d\,t'\,\sigma(\boldsymbol{r}-\boldsymbol{r}',t-t')\boldsymbol{E}(\boldsymbol{r}',t') \tag{1.33}$$

by means of the conductivity function assumed to be $\sigma(\boldsymbol{q},\omega)$ for a homogeneous system. Local-field effects are neglected. Its Fourier transform only depends on the frequency ω and momentum $\boldsymbol{q}$ of the incident light. In general, the conductivity is a complex quantity, its real part describes dissipation due to transitions in the material and is connected to the transitions between electronic states. Therefore, only the real part of the conductivity can be calculated directly if the corresponding transition matrix elements are known.

From Maxwells equations a linear dependence between the displacement field $\boldsymbol{D}$ and the electric field $\boldsymbol{E}$ is assumed by means of $\boldsymbol{D} = \epsilon\boldsymbol{E}$. From Ampere's law and Ohm's law the conductivity σ is related to the dimensionless dielectric function ϵ

$$\epsilon(\boldsymbol{q},\omega) = 1 + 4\pi i \frac{\sigma(\boldsymbol{q},\omega)}{\omega}\,, \tag{1.34}$$

where a harmonic time dependence $\sim \exp(-i\omega t)$ of the fields is assumed. Therefore, the imaginary part of the dielectric function is determined by the real part of the conductivity function. A very early approach for the determination of the dielectric constant in solids goes back to Ehrenreich and Cohen [75], Adler [76], Wiser [77] and Baroni [78]. In this work, the description of the optical response of the interacting many-body system to an external electromagnetic field is based on the independent-quasiparticle approximation (often called random-phase approximation) and the description of the electronic and atomic structure within the (semi-)local DFT as well as nonlocal functionals like HSE06 introduced before. In practice, already the effective potential in the Kohn-Sham equations contains nonlocal contributions attributed to the use of pseudopotentials in the description of the electron-electron interaction, that requires a careful treatment of the optical transition operators [79].

In general, the density response of a solid may be derived by means of an applied external longitudinal microscopic perturbation. Neglecting local-field effects it can be shown that the dielectric function in the longitudinal approach for $\hat{\boldsymbol{q}} \to 0$ ($\hat{\boldsymbol{q}} = \boldsymbol{q}/|\hat{\boldsymbol{q}}|$)is given by [79]

$$\epsilon(\hat{\boldsymbol{q}},\omega) = 1 + \frac{4\pi e^2}{V}\sum_{c,v}\sum_{\boldsymbol{k}}|M_{cv}(\boldsymbol{k},\boldsymbol{q})|^2 \sum_{\beta=\pm}\frac{1}{\varepsilon_c(\boldsymbol{k})-\varepsilon_v(\boldsymbol{k})-\beta(\hbar\omega+i\eta)} \tag{1.35}$$

with the optical matrix elements

$$M_{cv}(\boldsymbol{k}, \boldsymbol{q}) = \lim_{\boldsymbol{q} \to \boldsymbol{0}} \frac{1}{|\boldsymbol{q}|} \langle c\,\boldsymbol{k}|e^{i\boldsymbol{q}\boldsymbol{r}}|v\,\boldsymbol{k} + \boldsymbol{q}\rangle \;. \tag{1.36}$$

A semiconductor with fully occupied (unoccupied) valence (conduction) bands at zero temperature is assumed. The dielectric function depends on the volume V of the primitive cell in a periodic crystal and the sign β accounts for resonant and antiresonant contributions to positive and negative energies $\hbar\omega$. The parameter η is a small broadening parameter. In general, the wave functions in Eq. (1.36) are two-component spinors. Consequently, if the system is described within a non-spin polarized approximation the wave functions are scalars and an additional factor of 2 in Eq. (1.35) in front of the sum over conduction and valence bands might be introduced for convenience to account for the spin degeneracy of the electronic bands $\varepsilon_\nu(\boldsymbol{k})$. If the corresponding wave functions $|\nu\,\boldsymbol{k}\rangle$ of the many-electron problem are known, basically the optical transition matrix elements (1.36) can be computed.

The result in the limit $\boldsymbol{q} \to 0$ can be related to matrix elements of the components of the velocity operator v_α ($\alpha = x, y, z$) in a certain cartesian direction α by means of the relation

$$\boldsymbol{v} = \frac{i}{\hbar}[H, \boldsymbol{r}] \tag{1.37}$$

with the governing Hamiltonian H of the system under consideration. In the DFT the wave functions are determined as the solution of an effective single particle Kohn-Sham equation (1.17) within a local, semilocal or nonlocal approximation of the XC functional. As will be discussed later, in practice the core electrons of the many-body system are treated within a pseudopotential approach, that introduces non-local contributions to the effective Kohn-Sham potential (1.19) into the Hamiltonian. In general, non-local contributions V_{nl} have to be taken into account in the commutator (1.37). Thus, the velocity operator $\boldsymbol{v}$ is related to the momentum operator $\boldsymbol{p}$ by [79]

$$\boldsymbol{v} = \frac{\boldsymbol{p}}{m} + \frac{i}{\hbar}[V_{\mathrm{nl}}, \boldsymbol{r}] \,. \tag{1.38}$$

However, within the projector-augmented wave methodology (PAW), that is used for the construction of the pseudopotentials of the valence electrons, their wave functions are all-electron-like and thus, can be treated as based on a local Hamiltonian [80]. Furthermore, the explicit non-local HSE06 functional introduces non-local contributions to the Hamiltonian only very close to the cores of the atoms and thus, is practically local. Therefore, it is allowed not to consider the non-local contribution to the Hamiltonian and

the relation $\boldsymbol{v} = \boldsymbol{p}/m$ holds. Exploiting the relation

$$\langle c\,\boldsymbol{k}|e^{i\boldsymbol{qr}}|v\,\boldsymbol{k}'\rangle = \frac{\langle c\,\boldsymbol{k}|[H,e^{i\boldsymbol{qr}}]|v\,\boldsymbol{k}'\rangle}{\varepsilon_c(\boldsymbol{k}') - \varepsilon_v(\boldsymbol{k})} \tag{1.39}$$

from Eq. (1.36) and expanding the exponential for $\boldsymbol{q} \to 0$, for local potentials one obtains

$$M_{cv}(\boldsymbol{k},\boldsymbol{q}) = \frac{\hbar}{m} \sum_{\alpha=x,y,z} \frac{q_\alpha}{q} \frac{\langle c\,\boldsymbol{k}|p_\alpha|v\,\boldsymbol{k}\rangle}{\varepsilon_c(\boldsymbol{k}) - \varepsilon_v(\boldsymbol{k})} . \tag{1.40}$$

The appearance of the momentum operator in the matrix elements can also be interpreted as using the transversal gauge of the electromagnetic field. Thus, in the limit $\boldsymbol{q} \to 0$ the longitudinal and the transversal description of the optical response of the charge density to an external perturbation are equivalent. It is also convenient to rewrite the longitudinal expression of the dielectric function (1.35) which yields

$$\epsilon(\boldsymbol{q},\omega) = \sum_{\alpha,\beta=x,y,z} \frac{q_\alpha q_\beta}{q^2} \epsilon_{\alpha\beta}(\omega) \tag{1.41}$$

where we introduced the dielectric tensor

$$\epsilon_{\alpha\alpha'}(\omega) = \delta_{\alpha\alpha'} + \frac{4\pi e^2 \hbar^2}{m^2 V} \sum_{c,v} \sum_{\boldsymbol{k}} \frac{\langle c\,\boldsymbol{k}|p_\alpha|v\,\boldsymbol{k}\rangle \langle v\,\boldsymbol{k}|p_{\alpha'}|c\,\boldsymbol{k}\rangle}{[\varepsilon_c(\boldsymbol{k}) - \varepsilon_v(\boldsymbol{k})]^2} \sum_{\beta=\pm} \frac{1}{\varepsilon_c(\boldsymbol{k}) - \varepsilon_v(\boldsymbol{k}) - \beta(\hbar\omega + i\eta)} . \tag{1.42}$$

The dielectric function $\epsilon(\hat{\boldsymbol{q}},\omega)$ and also the dielectric tensor derived within the afore-mentioned approximations obey the symmetry relation $\epsilon(-\omega) = \epsilon(\omega)^*$. Equations (1.35) and (1.42) can be understood as a sum of independent Lorentz oscillators with resonant ($\beta = +$) and anti-resonant ($\beta = -$) contributions. In this work only hexagonal lattices are considered, for which the dielectric tensor is diagonal and optical isotropic in the x-y-plane, i.e., $\epsilon_{xx} = \epsilon_{yy} \neq \epsilon_{zz}$.

The complex dielectric function (1.35) can be separated in real and imaginary parts by means of the known relation

$$\frac{1}{x - x_0 + i\eta} \overset{\eta \to 0^+}{=} \frac{1}{x - x_0} - i\pi\delta(x - x_0) , \tag{1.43}$$

where the imaginary part is readily obtained

$$Im\,\epsilon(\boldsymbol{q},\omega) = \frac{4\pi^2 e^2}{V} \sum_{c,v} \sum_{\boldsymbol{k}} |M_{cv}(\boldsymbol{k},\boldsymbol{q})|^2 \sum_{\beta=\pm} \beta\,\delta(\varepsilon_c(\boldsymbol{k}) - \varepsilon_v(\boldsymbol{k}) - \beta\hbar\omega)) . \tag{1.44}$$

For $\omega > 0$ only the resonant contributions $\beta = +$ contribute and the anti-resonant

contributions to the imaginary part of the dielectric function can be neglected.

In this work of particular interest is the (optical) conductivity given in Eq. (1.34). For reasons that become clear in the corresponding chapter, the simultaneous evaluation of real and imaginary part of the conductivity is not always useful. If the optical transition matrix elements M_{cv} are known the direct evaluation of

$$Re\,\sigma(\boldsymbol{q},\omega) = \frac{\omega}{4\pi} Im\,\epsilon(\boldsymbol{q},\omega) \tag{1.45}$$

is easily possible due to the appearance of the Dirac delta function in (1.44). The imaginary part of the optical conductivity is then obtained by a Kramers-Kronig transformation

$$Im\,\sigma(\boldsymbol{q},\omega) = -\frac{1}{\pi}\mathcal{P}\int_{-\infty}^{\infty}\frac{Re\,\sigma(\boldsymbol{q},\omega')}{\omega'-\omega}d\omega'\,. \tag{1.46}$$

It will be necessary to compute the Kramers-Kronig transformation numerically. Therefore, in the next section a short overview is given on the method.

1.4.1 Numerical Kramers-Kronig transformation

For a complex function $\sigma(\omega) = Re\,\sigma(\omega) + i\,Im\,\sigma(\omega)$ (for simplicity the wave-vector dependence is dropped) that is analytic in the upper half-plane and on the real axis and if $\lim_{|\omega|\to\infty}|\sigma(\omega)|$ then the real and imaginary part of σ are related to each other by means of the Hilbert (or Kramers-Kronig) transformation [81]

$$\begin{aligned}
Im\,\sigma(\omega) &= -\frac{1}{\pi}\mathcal{P}\int_{-\infty}^{\infty}\frac{Re\,\sigma(\omega')}{\omega'-\omega}d\omega' \\
Re\,\sigma(\omega) &= \frac{1}{\pi}\mathcal{P}\int_{-\infty}^{\infty}\frac{Im\,\sigma(\omega')}{\omega'-\omega}d\omega'
\end{aligned} \tag{1.47}$$

with $\mathcal{P}$ as the Cauchy principal value. The numerical treatment of the Hilbert transformation is rather difficult due to the singular integrand and the appearance of $\mathcal{P}$. Furthermore, $\sigma(\omega)$ is given numerically on a not necessarily equidistant mesh and thus, in general not known for arbitrary frequencies.

The basic idea for the numerical treatment of the Hilbert transform is taken from Weinberg [82]. First, the pole in the integrand is removed

$$Im\,\sigma(\omega) = -\frac{1}{\pi}\int_{-\infty}^{\infty}\frac{Re\,\sigma(\omega')-Re\,\sigma(\omega)}{\omega'-\omega}d\omega'\,. \tag{1.48}$$

17

This is possible since the integral over the principal value of $1/(\omega' - \omega)$ vanishes. Thus, the pole of the integrand at $\omega' = \omega$ has been turned into a removable singularity and also the calculation of the principal value $\mathcal{P}$ is avoided. Second, since $Re\,\sigma(\omega)$ is symmetric in the sense that $Re\,\sigma(-\omega) = Re\,\sigma(\omega)$ and is assumed to vanish outside the range of interest $|\omega| > \omega_c$, the integral further reduces to

$$Im\,\sigma(\omega) = -\frac{2}{\pi} \int_0^{\omega_c} \frac{\omega Re\,\sigma(\omega') - \omega Re\,\sigma(\omega)}{\omega'^2 - \omega^2} d\omega' + \frac{Re\,\sigma(\omega)}{\pi} \log \frac{\omega_c + \omega}{\omega_c - \omega}. \qquad (1.49)$$

In a last step for each frequency of interest ω the integrand is interpolated using e.g. linear interpolation, cubic splines or Akima splines (depending somewhat on the smoothness of the integrand) while of course respecting the symmetry. This procedure allows for an easy performance of the integral.

1.5 Numerical methods - VASP

Even after all the approximations and simplifications presented above, the solution of the many-electron problems remains a difficult task which for real materials can only be achieved numerically. We use the DFT implementation in the Vienna ab-initio simulation package (VASP) [83,84]. Some details about the implementation will be discussed in the following paragraphs.

VASP is a highly efficient numerical DFT tool written in FORTRAN language that allows the computation of structural, electronic, and optical properties of almost arbitrary materials ranging from single atoms, molecules, quasi one-dimensional nanowires, two-dimensional sheet crystals to three-dimensional bulk materials. The atoms are usually separated in core and valence electrons, since core electrons are not contributing to chemical bonds. They are treated within a pseudopotential (PP) approach [85]. Details on the pseudopotentials that are used in this work are summarized in Tab. 1.1.

VASP is based on the description of systems with periodic boundary conditions in all three spatial dimensions which suggests an expansion of the wave functions in terms of plane waves in-between the PAW spheres. The corresponding plane-wave cutoff energy for the truncation of the expansion coefficients mainly depend on the used pseudopotentials and are given in Tab. 1.1. If different types of atoms are present in the calculation, the largest energetic plane-wave cutoff of all contributing atoms is usually sufficient for fully converged results. However, the convergence of all properties of the system with respect to the energy cutoff has been confirmed in all computations. The ionic relaxation has been performed until the Hellmann-Feynman forces are smaller than 0.001 eV/Å.

element	atomic number	electrons included in PP	valence electrons	energy cutoff
H	1	-	$1s^1$	250 eV
C	6	$1s^2$	$2s^22p^2$	400 eV
F	9	$1s^2$	$2s^22p^5$	400 eV
Si	14	$1s^22s^22p^6$	$3s^23p^2$	245 eV
Cl	17	$1s^22s^22p^6$	$3s^23p^5$	280 eV
Ca	20	$1s^22s^22p^63s^23p^6$	$3d^2$	103 eV
Ge	32	$1s^22s^22p^63s^23p^63d^{10}$	$4s^24p^2$	174 eV
Ag	47	$1s^22s^22p^63s^23p^63d^{10}4s^24p^6$	$4d^{10}5s^1$	250 eV
Sn	50	$1s^22s^22p^63s^23p^63d^{10}4s^24p^64d^{10}$	$5s^25p^2$	103 eV
I	53	$1s^22s^22p^63s^23p^63d^{10}4s^24p^64d^{10}$	$5s^25p^5$	176 eV

Table 1.1: Core electrons included in the pseudopotentials, electrons treated as valence and plane-wave cutoff used throughout this work.

In this work two-dimensional systems are of great importance. In order to deal with them in VASP a superlattice arrangement of infinitely many sheets separated by an artificial vacuum is studied, which is commonly known as the supercell approach. Convergence of the desired properties with respect to this vacuum must be checked carefully, in particular in the presence of electric dipoles in the sheet which give rise to long-range Coulomb potentials. Numerically the long-range electric fields can be compensated by introducing a sufficiently large layer of artificial dipoles in the vacuum region.

Another important part of this work is the investigation of surfaces and edges of three- and two-dimensional crystals, respectively. A method similar to the superlattice method is applied. In the actual 3D calculation a slab of atoms corresponding to a crystal with finite thickness in z-direction and a periodic arrangement in x-y-direction is placed in a unit cell. A large vacuum region, sometimes of the order of 10-20 Å is introduced in the calculation for the separation of periodic images of the slab in z-direction. The size of the vacuum is dictated by the requirement that there is no interaction between adjacent slabs. A slab of finite thickness consists of two surfaces which are both present in the actual numerical calculations. Thus, both sides of the slab must be constructed symmetrically, otherwise two distinct surfaces may lead to a wrong description and interpretation of the electronic properties of the slab. It is also necessary to use slabs big enough so that any finite size effects ("particle in a box") and any interaction between the surfaces mediated by the interior of the crystal is excluded. At last, the surfaces of the slab are typically passivated by hydrogen atoms, where the bond angles and distances are optimized within the DFT scheme.

For the calculation of electronic properties integrals over the Brillouin zone must be

performed. Numerically a regular Γ-centered Monkhorst-Pack [86] $\boldsymbol{k}$-point grid is used. In VASP, only symmetry-reduced $\boldsymbol{k}$ points belonging to the irreducible BZ (IBZ) are used in the actual calculation, which tremendously increases the performance of the code. Each $\boldsymbol{k}$ point in the IBZ is associated with a weight corresponding to the number of equivalent $\boldsymbol{k}$ points in the full BZ. The convergence to the ground state with respect to the number of $\boldsymbol{k}$ points is crucial, in particular for metallic systems. The convergence of the optical spectra also depends strongly on the number of $\boldsymbol{k}$ point, hence, details will be discussed in the corresponding sections.

1.5.1 HSE06 calculations

Calculations with hybrid functionals are in general very demanding. In principle, it is possible to start calculations from atomic orbitals and obtain the correct ground state self-consistently, as it is done in DFT calculations with local or semilocal XC functionals. However, since DFT calculations are very fast it is apparently more efficient to start already from the converged Kohn-Sham wave functions obtained within the DFT-GGA framework, since the HSE functional is based on GGA. Furthermore, besides the total energy of the system the Fock exchange potential needs to be computed on a grid of $\boldsymbol{q}$ points. It has been shown that the Fock exchange energy converges more rapidly with the number of $\boldsymbol{q}$ points than the total energy [69, 70]. Therefore, in the calculations the sampling density of the $\boldsymbol{q}$ points can be reduced compared to the number of $\boldsymbol{k}$ points. For graphene, $24 \times 24 \times 1$ $\boldsymbol{k}$ points and $9 \times 9 \times 1$ $\boldsymbol{q}$ points are sufficient in order to converge the total energy and the Fock exchange energy below 1 meV. For well-converged ground-state properties we use $32 \times 32 \times 1$ $\boldsymbol{k}$ points for all 2D honeycomb crystals. The number of $\boldsymbol{k}$ points is comparable large to guarantee convergence while it is also circumventing numerical issues related to SOC. For numerical reasons that will be addressed in the corresponding section, it is not always possible to use a reduced $\boldsymbol{q}$-point mesh in the calculations, thus, $\boldsymbol{k}$ and $\boldsymbol{q}$ lattices are usually chosen identical.

It is important to note that due to the mixing with exact exchange the functional not only depends on the electron density, but also on the wave functions itself. Therefore, the ground-state density alone is not sufficient for the description of the system. Thus, it is not possible to calculate the energy eigenvalues of the Hamiltonian at an arbitrary momentum within the BZ starting from the charge density. However, it is possible to obtain these eigenvalues and also the full band structure using the following approach: First of all a regular $N \times N \times 1$ $\boldsymbol{k}$-point mesh according to Monkhorst and Pack is generated, where only the $\boldsymbol{k}$ points in the IBZ are considered. The weights at each $\boldsymbol{k}$ point in the IBZ are determined according to the symmetries of the system. In the actual computation

arbitrary $\boldsymbol{k}$ points may be included, e.g. along high-symmetry lines , if their $\boldsymbol{k}$-point weight is set to zero such that they do not contribute to the calculation of the density of states and thus, do not contribute to the self-consistent calculation of the ground-state density. The major drawback of this method is the fact that the number of $\boldsymbol{q}$ points is always identical to the number of $\boldsymbol{k}$ points in the IBZ. However, the method is very accurate in determining band energies, but very time consuming.

1.6 Light propagation in multilayer thin films

In this work of special interest are 2D sheet crystals with thickness much smaller than the wavelength of visible light. Thus, from the point of view of macroscopic electrodynamics they are infinitely thin. However, impinging light may lead to surface currents within the 2D sheet dictated by Ohm's law (1.33) in two dimensions. The corresponding continuity equation

$$\operatorname{div} \boldsymbol{j}_{2\mathrm{D}}(\boldsymbol{r}, t) + \frac{\partial}{\partial t} \rho_{2\mathrm{D}}(\boldsymbol{r}, t) = 0 \tag{1.50}$$

also requires an induced time-dependent surface charge density $\rho_{2\mathrm{D}}(\boldsymbol{r}, t)$. Here we address the question of reflection, transmission and absorption of multilayer thin films according to Berning [87], however, including also conducting interfaces.

Assuming a multilayer system composed of layers with (relative) dielectric constant $\tilde{\epsilon}_j = Re\,\tilde{\epsilon}_j + i\,Im\,\tilde{\epsilon}_j$ and layer thickness d_j $(j = 1, \ldots, m)$, where the index $j = 0$ corresponds to the medium of incident light and $j = m+1$ to the substrate. The layers are separated by, in general, conducting interfaces with a 2D surface (or interface) conductivity $\sigma_{2\mathrm{D},j} = Re\,\sigma_{2\mathrm{D},j} + i\,Im\,\sigma_{2\mathrm{D},j}$ $(j = 0, \ldots, m)$. Of course, an implicit frequency dependency $\sigma_{2\mathrm{D},j}(\omega)$ is assumed.

The in-plane 2D conductivity of a very thin conducting sheet crystal within the DFT and a supercell approach is related to the 3D one (Eq. (1.34)), that is computed within the supercell approach, by means of

$$\sigma_{2\mathrm{D}}(\boldsymbol{q}, \omega) = L \cdot \sigma(\boldsymbol{q}, \omega), \tag{1.51}$$

where L is the size of the artificial superlattice dimension, the lattice constant, introduced in the supercell approach.

At the conducting interface between two media with distinct dielectric constants the tangential components of the electric field $\boldsymbol{E}$ and the normal components of the magnetic induction $\boldsymbol{B}$ are continuous. In contrast, for the tangential components of the magnetic

field $\boldsymbol{H}$ according to Ohm's law (1.33) and the normal components of the displacement field $\boldsymbol{D}$ according to the continuity equation (1.50) it holds

$$\boldsymbol{n} \times (\boldsymbol{H}_{j+1} - \boldsymbol{H}_j) = \frac{4\pi}{c} \boldsymbol{n} \times (\sigma_{2\mathrm{D},j} \boldsymbol{E}_j \times \boldsymbol{n}) \left(\equiv \frac{4\pi}{c} \boldsymbol{j}_{2\mathrm{D,j}} \right) \tag{1.52}$$

$$\boldsymbol{n} \cdot (\boldsymbol{D}_{j+1} - \boldsymbol{D}_j) = 4\pi \rho_{2\mathrm{D,j}} \,, \tag{1.53}$$

where the normal vector $\boldsymbol{n}$ of the interface points in the direction of propagation of the incident wave and the electric field $\boldsymbol{n} \times (\boldsymbol{E}_j \times \boldsymbol{n})$ describes the component of the electric field tangential to the interface. For plane waves at the interfaces between isotropic media the boundary condition (1.53) is always satisfied if (1.52) is satisfied due to the continuity equation (1.50). The method developed in [87] has been modified and extended in order to conserve the correct analytical properties of the dielectric function, which in turn is related to the sign convention of the dielectric constants and conductivities. Furthermore, conducting interfaces have been included as mentioned before. An y-z-coordinate system has been chosen, where the (positive) z direction corresponds to the direction of the incident light.

In each medium and interface several quantities are defined depending on the wavelength λ (or frequency ω) and angle of incidence θ_0 of the incident light, which are all dimensionless:

$$\tilde{k}_j^2 = \tilde{\epsilon}_j \qquad\qquad \text{square of normalized wave number } \tilde{\boldsymbol{k}}_j \tag{1.54}$$

$$\tilde{k}_{j,y} = \sqrt{\tilde{\epsilon}_0} \sin\theta_0 \equiv \tilde{k}_{0,y} \qquad\qquad y\text{-component of } \tilde{\boldsymbol{k}}_j \tag{1.55}$$

$$\tilde{k}_{j,z} = \sqrt{\tilde{\epsilon}_j - \tilde{\epsilon}_0 \sin^2\theta_0} \qquad\qquad z\text{-component of } \tilde{\boldsymbol{k}}_j \tag{1.56}$$

$$\tilde{\Phi}_j = \frac{2\pi}{\lambda} \tilde{k}_{j,z} d_j = \frac{\omega}{c} \tilde{k}_{j,z} d_j \qquad\qquad \text{complex phase thickness} \tag{1.57}$$

$$\tilde{\sigma}_{2\mathrm{D},j} = \frac{4\pi}{c} \sigma_{2\mathrm{D},j} \qquad\qquad \text{normalized 2D surface conductivity.} \tag{1.58}$$

It is important to note that the root in the calculation of $\tilde{k}_{j,z}$ must be chosen in such a way that $Im\,\tilde{k}_{j,z} > 0$ in order to describe evanescent waves within the media. The incident light is polarized either within the plane of incidence (p) or perpendicular (s) taken into account by means of the expression

$$\tilde{\eta}_j = \begin{cases} \tilde{k}_{j,z} & (s\text{-pol}) \\ \tilde{\epsilon}_j/\tilde{k}_{j,z} & (p\text{-pol}) \end{cases}. \tag{1.59}$$

For s and p polarized light the electric field on either side of the jth interface boundary can be divided transmitted (t) and reflected (r) portions leading to the shorthand notations

$E_{j-}^{(t)}$, $E_{j+}^{(t)}$, $E_{j-}^{(r)}$, and $E_{j+}^{(r)}$, where the "+" and "−" designations serve to denote the fact that the individual wave functions are in general discontinuous at a boundary. The reflected and transmitted electric fields on either side of the interface are related to each other by means of the transfer matrix D_j

$$\begin{bmatrix} E_{j-}^{(t)} \\ E_{j-}^{(r)} \end{bmatrix} = D_j \begin{bmatrix} E_{j+}^{(t)} \\ E_{j+}^{(r)} \end{bmatrix} , \quad D_j = \begin{bmatrix} \frac{1}{2}\left(1 + \frac{\tilde{\eta}_{j+1} + \tilde{\sigma}_{2\mathrm{D},j}}{\tilde{\eta}_j}\right) & \frac{1}{2}\left(1 - \frac{\tilde{\eta}_{j+1} - \tilde{\sigma}_{2\mathrm{D},j}}{\tilde{\eta}_j}\right) \\ \frac{1}{2}\left(1 - \frac{\tilde{\eta}_{j+1} + \tilde{\sigma}_{2\mathrm{D},j}}{\tilde{\eta}_j}\right) & \frac{1}{2}\left(1 + \frac{\tilde{\eta}_{j+1} - \tilde{\sigma}_{2\mathrm{D},j}}{\tilde{\eta}_j}\right) \end{bmatrix} . \tag{1.60}$$

The propagation matrix P_j

$$\begin{bmatrix} E_{(j-1)+}^{(t)} \\ E_{(j-1)-}^{(r)} \end{bmatrix} = P_j \begin{bmatrix} E_{j-}^{(t)} \\ E_{j-}^{(r)} \end{bmatrix} , \quad P_j = \begin{bmatrix} e^{-i\tilde{\Phi}_j} & 0 \\ 0 & e^{i\tilde{\Phi}_j} \end{bmatrix} \tag{1.61}$$

mediates the free propagation of the electric field through a given material with dielectric constant ϵ_j. The optical properties of the multilayer system depend only on the ratio of the electric fields on either side of the entire slab system, where on the transmitted side only the transmitted wave $E_{m+}^{(t)}$ is present, thus, one may choose the initial values for the propagation simply as

$$\begin{bmatrix} E_{m+}^{(t)} \\ E_{m+}^{(r)} \end{bmatrix} = \begin{bmatrix} 1 \\ 0 \end{bmatrix} . \tag{1.62}$$

The Poynting vector finally yields reflection R, transmission T and absorption A of the multilayer system

$$R = \frac{\left|E_{0-}^{(r)}\right|^2}{\left|E_{0-}^{(t)}\right|^2} , \qquad T = \frac{Re\,\tilde{\eta}_{m+1}}{Re\,\tilde{\eta}_0}\frac{1}{\left|E_{0-}^{(t)}\right|^2} , \qquad A = 1 - R - T . \tag{1.63}$$

The above equations will be used to determine the reflection, transmission and absorption of (atomically thin) two-dimensional honeycomb crystals surrounded by air, but they may also be used for deposited sheet crystals on arbitrary substrates with a frequency-dependent dielectric function. In general, the framework of the transfer matrix approach [88] also allows calculations on (noninteracting) multilayers of e.g. graphene and the investigation of their photonic bandgaps and plasmon dispersion [89].

1.7 Topological insulators

1.7.1 Quantum (spin-) Hall effect and topological $\mathbb{Z}_2$ invariants

In the last decades topological invariants became increasingly important for the characterization of insulating crystals. They are strongly connected to the Berry phase, which has been used for the investigation of the quantum Hall effect (QHE) present in 2D electron gases subjected to strong magnetic fields [90–94]. The magnetic field is needed in order to break time-reversal symmetry. Nevertheless, even without an external magnetic field and in presence of time-reversal symmetry another quantum Hall-like effect has been measured [29]. In contrast to the QHE the latter one describes spin instead of charge currents and, consequently, is named the quantum spin Hall effect. The QSHE is driven by internal magnetic fields mediated by spin-orbit coupling. The quantum spin Hall phase is further associated with a $\mathbb{Z}_2$ topological invariant, which distinguishes it from an ordinary insulator [28]. In two-dimensional electron systems a single $\mathbb{Z}_2$ invariant governs the effect.

However, in contrast to the QHE, the QSHE also has a generalization in three dimensions. In general, there are two classes: the weak (WTI) and strong (STI) topological insulator. In two dimensions there may exist only the STI characterized by a single $\mathbb{Z}_2$ invariant. In three dimensions WTI and STI may exist, characterized by four $\mathbb{Z}_2$ invariants. The WTI in 3D are like layered 2D QSH states, but they may be destroyed by disorder. The STI are robust against weak disorder and passivation and lead to metallic states at the boundary to trivial insulators (including of course the vacuum) [41]. The surface or interface states possess peculiar properties which have potential applications in spintronics. The surface states resemble the dispersion of massless Dirac particles. Each momentum related to the surface state has only one single spin state, more precisely, the spin direction rotates as momentum moves around the Fermi surface [95, 96]. Therefore, they are called chiral states. The scattering between these states is forbidden by the selection rule leading to perfect transport. Adding defects or small disorder may allow scattering, however, due to the topological properties of the bulk the metallic surface state is not allowed to vanish. The bulk properties protect the surface state from disappearance [95]. The topological invariant of a system cannot change by an adiabatic change in the Hamiltonian (e.g. strain or electric fields) as long as the bulk remains insulating. Therefore, any adiabatic mechanism that closes and reopens the electronic bandgap may change the topological invariant of system and characterizes a possible phase transition.

Based on tight-binding calculations, one of the first systems that has been proposed

to exhibit a non-trivial topology was a 2D honeycomb structure with π orbitals like graphene [28]. In reality, the SOC in graphene is not strong enough leading to a zero-gap semiconductor and thus, violates the assumption of an insulating material. However, SOC opens a sizable electronic bandgap for honeycomb crystals based on the heavier atoms Si, Ge, and Sn (see Sec. 2.4.3). Therefore, in this work we apply a method that allows the computation of the $\mathbb{Z}_2$ invariant of arbitrary crystals, in particular the 2D group-IV honeycomb crystals. The method is based on the electronic band structure and the associated Bloch wave functions expressed as Pauli spinors obtained within the framework of the DFT.

In general, the calculation of the $\mathbb{Z}_2$ invariant as presented in the work of Fu and Kane [40] requires a fixed phase relation (gauge) between the wave functions throughout the entire Brillouin zone. The gauge is naturally fixed in e.g. calculations based on the tight-binding method. However, the DFT solves the Kohn-Sham equations at distinct $\boldsymbol{k}$ points independently. Fixing the gauge in the DFT is in general a complicated problem. Recently, equivalent approaches for the determination of the $\mathbb{Z}_2$ invariant based on the idea of Wannier charge centers have been proposed [97–100], which are completely gauge invariant. In the subsequent sections we present two methods used in this work for two-dimensional systems. The first method is restricted to systems possessing a spatial inversion center, the second one is applicable to arbitrary insulators. Finally, the extension to three dimensions is briefly discussed in each section, which finally completes the introduction on topological insulators.

A code has been developed that allows the usage of both methods based on VASP. In particular the general method for crystals without inversion symmetry required some modifications to the VASP code itself, since it implies the calculation of the overlap between wave functions within the PAW framework.

1.7.2 Insulators with inversion symmetry

For insulators with time-reversal symmetry the presence of inversion symmetry greatly simplifies the problem of evaluating the $\mathbb{Z}_2$ invariant. There exist special momenta $\boldsymbol{k} = \boldsymbol{\Gamma}_i$ in the BZ which are time-reversal invariant (TRIM) that satisfy the relation

$$-\boldsymbol{\Gamma}_i = \boldsymbol{\Gamma}_i + \boldsymbol{G} \tag{1.64}$$

for a reciprocal-lattice vector $\boldsymbol{G}$. Each point $\boldsymbol{\Gamma}_i$ is represented as a linear combination of basis vectors of the reciprocal lattice $\boldsymbol{b}_i$ according to $\boldsymbol{\Gamma}_i = \sum_i \mu_i \boldsymbol{b}_i$, where the coefficients

$\mu_i \in (-0.5, 0.5]$ are within the first BZ. Any $\boldsymbol{G}$ vector is represented by $\boldsymbol{G} = \sum_i n_i \boldsymbol{b}_i$ with arbitrary integers n_i. Eq. (1.64) can easily be solved for the TRIM points, since $n_i = 0$ requires $\mu_i = 0$, and $n_i = -1$ requires $\mu_i = 1/2$. Other solutions do not exist within the aforementioned restrictions on n_i and μ_i. Therefore, for any reciprocal lattice in two dimensions there exist four TRIM points as displayed in Table 1.2, and likewise there exist eight TRIM points in three dimensions. It can be shown [101] that for an insulator with

Table 1.2: Relative coordinates of the four TRIM points for arbitrary crystals in two dimensions. The denotation of the TRIM points in a hexagonal lattice is given in brackets.

μ_1	μ_2	label
0	0	Γ (Γ)
1/2	0	M_1 (M)
0	1/2	M_2 (M)
1/2	1/2	M_3 (M)

$2N$ occupied bands all bands come in Kramers-degenerate pairs, which means, for each energy $\varepsilon_\nu(\boldsymbol{k})$ obtained as solution of the Schrödinger (or Kohn-Sham) equation there exists a solution with the same energy but with opposite momentum $\epsilon_{\nu'}(-\boldsymbol{k})$. Furthermore, at each TRIM point the energy bands $\varepsilon_\nu(\boldsymbol{\Gamma}_i)$ are degenerate. According to Ref. [101] the $\mathbb{Z}_2$ invariant can be deduced from the knowledge of the parity of each pair of Kramers degenerate occupied energy bands at the time-reversal and inversion invariant points. The parity of any band at these points is calculated as the expectation value of the parity operator P

$$\xi_i(\boldsymbol{\Gamma}_i) = \langle u_{\boldsymbol{\Gamma}_i,n}|P|u_{\boldsymbol{\Gamma}_i,n}\rangle = \int_{\mathrm{BZ}} \begin{pmatrix} u^{\uparrow*}_{\boldsymbol{\Gamma}_i,n}(\boldsymbol{r}) & u^{\downarrow*}_{\boldsymbol{\Gamma}_i,n}(\boldsymbol{r}) \end{pmatrix} \begin{pmatrix} u^{\uparrow}_{\boldsymbol{\Gamma}_i,n}(-\boldsymbol{r}) \\ u^{\downarrow}_{\boldsymbol{\Gamma}_i,n}(-\boldsymbol{r}) \end{pmatrix} d^3\boldsymbol{r}\,, \tag{1.65}$$

where the Bloch functions $|u_{\boldsymbol{\Gamma}_i,n}\rangle$ are of course two-component spinors. In two dimensions the $\mathbb{Z}_2$ invariant ν_0 is then given by

$$(-1)^{\nu_0} = \prod_{i=1}^{N} \delta_i \tag{1.66}$$

where each δ_i is the product of the parities of all occupied Kramers degenerate bands

$$\delta_i = \prod_{m=1}^{N} \xi_{2m}(\boldsymbol{\Gamma}_i)\,. \tag{1.67}$$

The method is easily generalized to three-dimensional systems [41, 101]. The parities at all eight TRIM points according to Eq. (1.65) are needed for the calculation of the δ_i's as in two dimensions, which lead to four independent $\mathbb{Z}_2$ invariants labeled ν_i ($i = 0, 1, 2, 3$).

One of these invariants is the product over all eight points. The other three invariants are given as the product over four δ_i's, for which all contributing momenta $\mathbf{\Gamma}_i$ reside in the same plane:

$$(-1)^{\nu_0} = \prod_{i=1}^{8} \delta_i \tag{1.68}$$

$$(-1)^{\nu_k} = \prod_{n_k=1;n_{j\neq k}=0,1} \delta_{i=(n_1 n_2 n_3)}. \tag{1.69}$$

The topological index ν_0 is robust against disorder and is thus named the strong topological index. In three dimensions the ν_k ($k = 1, 2, 3$) depend on the choice of the reciprocal lattice vectors and thus, indicate possible topological nontrivial surface states in certain crystal orientations. They are weak topological invariants, since they are not robust in the presence of disorder.

1.7.3 Insulators without inversion symmetry

For insulators without inversion symmetry the parity of states is not well defined and the method described in Sec. 1.7.2 fails. The method we use in this work is based on the approach presented by Yu et *al.* [97], although many similar proposals exist [98, 99]. The advantage of all the aforementioned methods is their gauge invariance, since they do not rely on a fixed gauge between the wave functions at distinct $\mathbf{k}$ points in the BZ. As already stated by Fu and Kane [40] the virtual spin pumping that defines a quantum spin Hall state is strongly related the evolution of the charge center of the Wannier functions (WCC) constructed from the subspace of the $2N$ occupied states. The information on the WCC is encoded in the position operator projected on this occupied subspace, which in turn is related to the Bloch eigenstates of the associated Hamiltonian (for details see Ref. [97]). In two dimensions the eigenvalue problem of the position operator of the WCC can be solved by introducing the $2N \times 2N$ matrix product

$$D(k_y) = F_{0,1}F_{1,2}\ldots F_{N_x-2,N_x-1}F_{N_x-1,0}, \tag{1.70}$$

where the $2N \times 2N$ overlap matrices between the Bloch states $F_{j,j+1}$ are defined as

$$F_{j,j+1}^{mn}(k_y) = \langle m, k_{x,j}, k_y | n, k_{x,j+1}, k_y \rangle. \tag{1.71}$$

In an arbitrary 2D lattice the momentum $k_{x,j} = j/N_x$ ($j = 0, \ldots, N_x - 1$) is the fraction of the reciprocal lattice vector $\mathbf{b}_1$ in the interval $[0, 1)$ (entire length of the BZ excluding

the right boundary) with discrete spacing $\Delta_x = 1/N_x$. The momentum k_y is equivalently the fraction of the reciprocal lattice vector $\boldsymbol{b}_2$. The method seems to favor one direction in the BZ over another, however, in the end the wave functions in the entire 2D BZ are taken into account and thus, the method can be formulated with $\boldsymbol{b}_1$ and $\boldsymbol{b}_2$ exchanged. It has to be stressed, that k_x and k_y are not Cartesian coordinates but relative coordinates in a (not necessarily orthogonal) coordinate system spanned by $\boldsymbol{b}_1$ and $\boldsymbol{b}_2$.

For any given k_y the matrix $D(k_y)$ is unitary and thus, all its $2N$ complex eigenvalues

$$\lambda_m^D(k_y) = \left|\lambda_m^D\right| e^{i\theta_m^D(k_y)}, \qquad (m = 1, \ldots, 2N) \tag{1.72}$$

are on the unit circle $\left|\lambda_m^D\right| = 1$. Following the procedure of Yu et *al.* [97], the phase of the eigenvalues

$$\theta_m^D(k_y) = \mathrm{Im}\left[\ln \lambda_m^D(k_y)\right] \tag{1.73}$$

is computed as a function of k_y along the BZ starting at $k_y = 0$ and ending at the BZ boundary $k_y = 0.5$ (in terms of $\boldsymbol{b}_2$). At $k_y = 0$ the eigenvalues of the D matrix appear in degenerate pairs due to time-reversal symmetry, which results in pairs of Wannier centers sitting at $k_y = 0$. However, when k_y is varied between the endpoints of the interval the Wannier centers may split and recombine at $k_y = 0.5$. The $\mathbb{Z}_2$ topological index is related to the number of intersections of an arbitrary reference line $\theta_R = \mathrm{const.}$ with the lines $\theta_m^D(k_y)$. An odd number of intersections immediately identifies a topological insulator, while an even number of intersections defines a trivial one. An odd number of intersections can only occur, if the WCCs switch partners when their phase is traced between $k_y = 0$ and $k_y = 0.5$, which is related to a non-trivial topology of the insulating system. An example for the two-band first-nearest neighbor tight-binding Hamiltonian with one transfer integral representing the symmetry of hexagonal systems is depicted in Fig. 1.2. The reference line $\theta_R/(2\pi) = -0.3$ crosses the line one (zero) times indicating a topological (trivial) insulator in Fig. 1.2(a) (Fig. 1.2(b)).

The generalization of the method to three dimensions is straightforward and very similar to systems with inversion symmetry. A good description can be found in Ref. [98]. In 3D there are eight TRIM points which might be thought of as the vertices of a parallelepiped in reciprocal space having six faces. At each face the Bloch Hamiltonian $H(\boldsymbol{k})$ can be regarded as a fictitious 2D system function of two k variables, whereas the third one is fixed. The method described above is then applied to each of the six faces separately. The three weak indices $\nu_{i=(1,2,3)}$ are associated with the $\mathbb{Z}_2$ invariant in the three outer faces that do not contain the Γ point. The strong index ν_0 is the sum (mod 2) of the $\mathbb{Z}_2$ invariants of all phases.
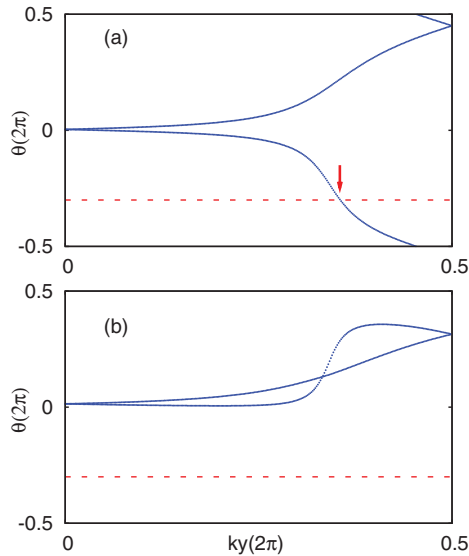
Figure 1.2: Evolution of Wannier charge centers for hexagonal systems in (a) the QSH phase and (b) the normal insulating phase. (Image taken from [97]).

1.8 Coincidence lattices

The investigation of surfaces of solids is a very interesting task from the theoretical and experimental point of view since it can strongly alter properties of the bulk [102]. The crystal surface also represents the interface between the environment as well as measuring devices, typically positioned outside the crystal, and the interior of the crystal. In this work of particular interest are group-IV honeycomb crystals grown on top of metals [103–105] and insulators [106, 107]. A lattice that describes the primitive cell of the substrate and the overlayer is called the coincidence lattice which provides the corresponding lattice vectors of the 2D surface cell. The surface of a crystal corresponds to a well-defined crystal plane in the bulk, where the plane is characterized by a normal vector $\boldsymbol{n}$. Energetically favorable cleavage faces are typically known from experiment and often correspond to highly symmetric surfaces. In this work silicene on the (111) surface of Ag is studied. Ag bulk crystallizes in an cubic face-centered lattice. The normal vector $\boldsymbol{n} = [111]$ corresponds to the direction along the space diagonal in a cube. Consequently, a proper primitive cell for the description of the surface should consist of two lattice vectors perpendicular to $\boldsymbol{n}$ and a third vector parallel to $\boldsymbol{n}$. It is common to choose the z-axis of the surface lattice parallel to the direction of $\boldsymbol{n}$.

If the surface of a bulk crystal is known and another crystal is, e.g., grown epitaxially on top, the question arises, what are possible coincidence lattices. In order to find the coincidence lattice between honeycomb crystals and an arbitrary substrate a two-step procedure is applied. First, the proper surface cell of the bulk crystal is constructed. Second, the lattice vectors of this cell and the overlayer are matched to each other in terms of shape and size. Both steps are explained in more detail below.

1.8.1 Smallest irreducible slab cell

Any 3D bulk crystal is described by the three primitive basis vectors $\boldsymbol{a}_1$, $\boldsymbol{a}_2$, and $\boldsymbol{a}_3$ of its Bravais lattice. The three vectors span the smallest cell (primitive cell) of the periodic crystal. However, an necessarily non-primitive cell S_1 may be generated by any possible linear combinations of the three lattice vectors $\boldsymbol{a}_1$, $\boldsymbol{a}_2$, and $\boldsymbol{a}_3$. The smallest irreducible slab cell S_2 is defined as the smallest primitive cell consisting of lattice vectors $\boldsymbol{a}'_1$, $\boldsymbol{a}'_2$, and $\boldsymbol{a}'_3$ with the requirement that it is another representation of the lattice S_1 and it additionally holds $\boldsymbol{a}'_3 \parallel \boldsymbol{n}$ and $\boldsymbol{a}'_1, \boldsymbol{a}'_2 \perp \boldsymbol{n}$.

If there exists at least one crystal cell S_2 with the aforementioned properties, there also exist cells S_3, S_4, ... with lattice vectors of double, triple, ... the length in each direction leading to infinitely many possible lattices. Furthermore, S_2 may be described equally well by different Bravais lattices with the same volume, though. We are thus interested in the lattice S_2 with the smallest possible volume and the highest symmetry with regard to its describing 2D Bravais lattice. If a 2D Bravais lattice is found, the length of vector $\boldsymbol{a}_3$ to describe the full bulk in the new cell is to be determined.

Numerical implementation

An algorithm has been implemented that can handle arbitrary lattices while it requires only a minimal input. Here we give an overview over the basic ideas. In order to satisfy the restrictions given above we need to construct all possible lattice vectors $\boldsymbol{a}' = \lambda \boldsymbol{a}_1 + \mu \boldsymbol{a}_2 + \nu \boldsymbol{a}_3$ ($\lambda, \mu, \nu \in \mathbb{Z}$) and collect only those perpendicular to $\boldsymbol{n}$. For numerical reasons we are forced to introduce a cutoff parameter to restrict the number of possible triples $\{\lambda, \mu, \nu\}$ to a finite number. Thus, the cutoff parameter is defined as the maximum length $L_{\max}$ of the vector $\boldsymbol{a}'$. That means, we restrict ourselves to cells with the longest edge smaller than $L_{\max}$, which is motivated physically. The algorithm extends the search space automatically until all proper vectors $\boldsymbol{a}' \perp \boldsymbol{n}$ are constructed. At the end, all pairs of linearly independent vectors $(\boldsymbol{a}'_1, \boldsymbol{a}'_2)$ are gathered and classified into 2D Bravais lattices with their corresponding dimensions. The smallest 2D lattice with the highest symmetry is taken for further investigation.

The last step concerns the length of the vector $\boldsymbol{a}'_3$ which of course must end at a lattice point that belongs to S_1. The problem reduces to the question, if there exists a solution to the equation

$$t_1 \boldsymbol{a}_1 + t_2 \boldsymbol{a}_2 + t_3 \boldsymbol{a}_3 = \gamma \frac{\boldsymbol{n}}{|\boldsymbol{n}|} \tag{1.74}$$

within the space $t_i \in \mathbb{N}$ and $\gamma \in \mathbb{R}$? Since S_1 is periodic in all directions the solution cannot be unique. There may exist a smallest γ_0 and corresponding t_i, which lead to

multiple solutions of the equation. Numerically the equation is solved by starting with a small positive value γ and increasing it in small steps, where small means typically a fraction of the dimension of atomic distances (e.g. 0.1 Å). For each γ Eq. (1.74) is solved for all t_i and rounded to the next nearest integer. Then the left-hand side of (1.74) is evaluated again using the rounded values. If the vector is parallel to $\boldsymbol{n}$ it is considered as the missing third lattice vector $\boldsymbol{a}_3'$. After the crystal lattice S_2 is fully determined the atomic basis is transformed from S_1 to S_2.

1.8.2 Coincidence lattice

Finally, the coincidence lattice between the smallest irreducible slab cell and the overlayer can be constructed along the common axis $\boldsymbol{n}$. However, most often it is not possible to find a perfectly matching common lattice. Instead, we allow strain or stress to occur solely in the overlayer in order to fulfill the matching conditions approximately as it can be found in experiments. There may exist no or infinitely many coincidence lattices, hence, we introduce another cutoff parameter R_{max} which restricts the maximum size of the primitive cell (it may also act as a stopping criterion for the algorithm, if no coincidence lattice is found). All linear combinations of in-plane lattice vectors of each crystal are constructed and grouped in tuples. Tuples describing the same Bravais lattice are removed, the remaining 2D lattices of the substrate are compared with those of the overlayer. If they are identical they are considered as coincidence lattices.

Chapter 2

Group-IV honeycomb crystals
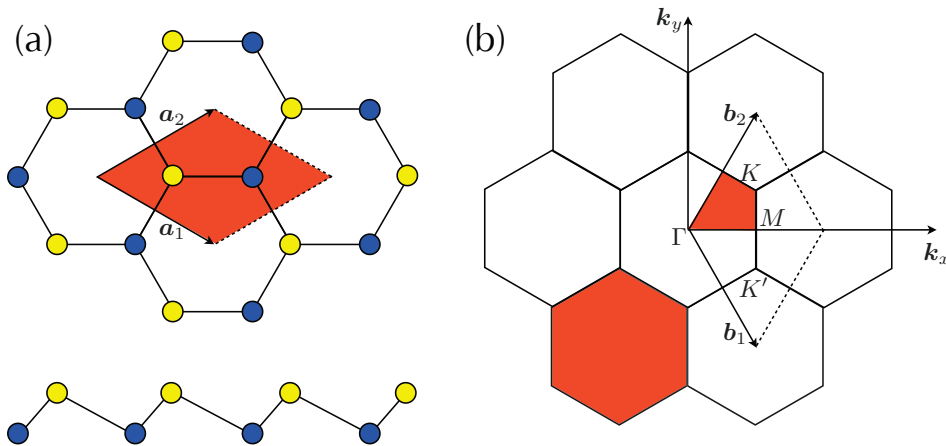
2.1 Crystal structure

Graphene, silicene, germanene and stanene can be described as a two-dimensional hexagonal Bravais lattice with two basis atoms. Within the supercell approach described in Sec. 1.5 the 2D crystal is placed in a 3D simulation box with periodic boundary conditions in all three spatial dimensions. The lattice vectors are defined as

$$\boldsymbol{a}_1 = \frac{a}{2}(3, -\sqrt{3}, 0),\ \boldsymbol{a}_2 = \frac{a}{2}(3, \sqrt{3}, 0),\ \text{and}\ \boldsymbol{a}_3 = a(0, 0, L/a)\,. \tag{2.1}$$

The factor a describes the in-plane nearest-neighbor distance between two adjacent basis atoms, which is $a = 1.42$ Å for graphene [108]. The lattice constant a_0 of the hexagonal crystal is related to a by means of $a_0 = \sqrt{3}a$. L is the distance between adjacent sheets in the artificial supercell direction $\boldsymbol{e}_z$. The distance L must be chosen such that any interaction between neighboring sheets is negligible. Hence, we increased the distance L until the electrostatic potential as a function of the z coordinate exhibits a flat plateau in the vacuum region between the sheets. Typically $L = 20$ Å is a very safe choice for all 2D crystals under investigation. In general the positions of the basis atoms are fixed up to an arbitrary translation within the unit cell. However, a symmetric arrangement is advantageous with respect to theoretical calculations and visualization, thus, the basis atoms are kept fixed at the positions

$$\boldsymbol{c}_1 = \frac{1}{3}(\boldsymbol{a}_1 + \boldsymbol{a}_2) + \frac{1}{2}(\boldsymbol{a}_3 + \Delta \cdot \boldsymbol{e}_z)\ \text{and}\ \boldsymbol{c}_2 = \frac{2}{3}(\boldsymbol{a}_1 + \boldsymbol{a}_2) + \frac{1}{2}(\boldsymbol{a}_3 - \Delta \cdot \boldsymbol{e}_z)\,. \tag{2.2}$$

as depicted in Fig. 2.1(a). The buckling height Δ accounts for the out-of-plane shift of the basis atoms.

Figure 2.1: (a) Top and side view of the crystal structure of group-IV honeycomb crystals. The atomic basis of the crystal is depicted as blue an yellow spheres. The unit cell is shaded red. (b) Reciprocal lattice of the 2D hexagonal Bravais lattice. The first Brillouin zone (hexagon) and the irreducible part of the Brillouin zone for the space group $p3m1$ [102, 109] are shaded in red.

The reciprocal lattice vectors

$$\boldsymbol{b}_1 = \frac{2\pi}{a_0}\left(\frac{1}{\sqrt{3}}, -1, 0\right), \; \boldsymbol{b}_2 = \frac{2\pi}{a_0}\left(\frac{1}{\sqrt{3}}, 1, 0\right), \; \text{and } \boldsymbol{b}_3 = \frac{2\pi}{L}(0, 0, 1) \tag{2.3}$$

describe a hexagonal lattice as well (cf. Fig. 2.1(b)). Thus, the first Brillouin zone (BZ) is a hexagon which is, however, rotated through 30° against the real-space hexagons of the honeycomb lattice. Since the sheet distance L is large, no dispersion is expected in $\boldsymbol{b}_3$ direction. Hence, in the numerical calculations a $N \times N \times 1$ Monkhorst-Pack $\boldsymbol{k}$-point mesh is used and, consequently samples the 3D BZ with $N \times N$ points in the k_x-k_y-plane, whereas $k_z = 0$. Effectively, only a 2D BZ is considered. Of superior importance are the six corners of the 2D BZ, representing Dirac points. Although these six point are equivalent from the energetic point of view it can be shown that there is indeed a difference in the determining Hamiltonian [108]. Thus, the wave functions between neighboring Dirac points differ although the energy eigenvalues are equal. For this reason, the Dirac points are classified into K and K' located at e.g.

$$\boldsymbol{K} = \frac{1}{3}\boldsymbol{b}_1 + \frac{2}{3}\boldsymbol{b}_2 \; \text{and } \boldsymbol{K}' = \frac{2}{3}\boldsymbol{b}_1 + \frac{1}{3}\boldsymbol{b}_2 \tag{2.4}$$

alternating at the corner points of the hexagonal Brillouin zone. The mid-edge point M is located at

$$\boldsymbol{M} = \frac{1}{2}(\boldsymbol{b}_1 + \boldsymbol{b}_2). \tag{2.5}$$

2.2 Electronic structure from tight-binding model

The group-IV honeycomb crystals share similar electronic properties of their atomic building blocks and thus, also similar electronic properties. In particular the valence electrons mainly fill one s and three p orbitals with the possibility of building hybrid orbitals when composed to crystals. It will be shown from first principles, that the atomic arrangements in silicene, germanene and stanene possess a non-vanishing buckling height Δ, whereas graphene remains atomically flat. In the nearest-neighbor tight-binding description for buckled structures the π (built from atomic p_z orbitals) and σ orbitals (build from atomic s and $p_{x,y}$ orbitals) are coupled. Here we neglect the coupling, which in turn decouples π orbitals and σ orbitals and one may treat both problems separately. The decoupling is naturally present in graphene due to its vanishing buckling. For silicene, germanene and stanene the description of the energy bands is still valid at least close to the Dirac points K and K'. Energetically, the σ orbitals correspond to strongly bound electrons with deep-lying energy bands, whereas the π orbitals correspond to electrons with energies close to the Fermi level. Therefore, the tight-binding model can be restricted to one p_z orbital per lattice site [1, 108, 110–115].

As stated, the buckling of the atoms is neglected and a truly 2D system is obtained. Each atom has three nearest and six next-nearest neighbors (cf. Fig. 2.1). Following the procedure presented in the book of Saito *et al.* [110] the eigenvalues of the Hamiltonian as a function of $\boldsymbol{k}$ become [111, 115]

$$\varepsilon(\boldsymbol{k}) = \varepsilon_p \pm t\sqrt{3 + f(\boldsymbol{k})} + t'f(\boldsymbol{k})$$

$$f(\boldsymbol{k}) = 2\cos\left(\sqrt{3}k_y a\right) + 4\cos\left(\frac{3}{2}k_x a\right)\cos\left(\frac{\sqrt{3}}{2}k_y a\right) \tag{2.6}$$

where t (t') is the nearest-neighbor (next-nearest neighbor) hopping energy and ε_p is the on-site energy. The full dispersion of the π bands is depicted in Fig. 2.2. Since ε_p only
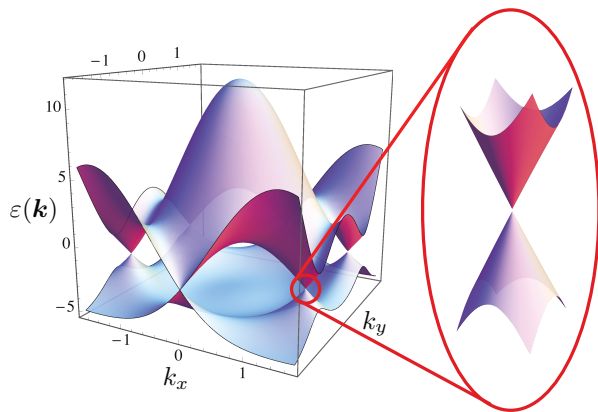
Figure 2.2: Example of the π-band structure of the group-IV honeycomb crystals setting $\varepsilon_p = 0$, $t = -2.7$ eV, $t' = -0.2t$. The region around one K point is enlarged and shows conical conduction and valence bands corresponding to massless Dirac fermions.

describes an energy shift it is usually neglected. The valence and conduction bands are touching each other exactly at the Dirac points in the 2D hexagonal BZ. The parameter t' originating from the next-nearest interaction terms breaks the electron-hole symmetry. Its exact value depends strongly on the system, but it is usually much smaller than the nearest-neighbor parameter t.

In the vicinity of a Dirac point K the band dispersion can be expanded in a series, leading to a linear dispersion

$$\varepsilon(\boldsymbol{q}) = \pm \hbar v_F |\boldsymbol{q}|, \qquad \boldsymbol{q} = \boldsymbol{k} - \boldsymbol{K}, \tag{2.7}$$

which resembles the dispersion of massless (Dirac) particles, either electrons or holes, traveling with the Fermi velocity $v_F = -3/2ta/\hbar$. As will be shown later, v_F is in general two orders of magnitude smaller than the speed of light.

The tight-binding model describes very well the π bands of the group-IV honeycomb crystals. Since the buckling and also spin-orbit coupling has been neglected it is best suited for the description of graphene. Taking into account also the buckling results in a complicated coupling between the σ and π bands [112, 116]. The increasing mass of the atoms along the group-IV increases the importance of spin-orbit coupling, which has been taken into account in the tight-binding model as well [43, 116, 117]. However, SOC is only considered approximately by either neglecting again the buckling or by constructing an approximate Hamiltonian around the Dirac points. These drawbacks can be overcome by first-principles methods presented in the next section.

2.3 Structural properties from first principles

In this section we employ density functional theory as implemented in the VASP package. Exchange and correlation (XC) are described within the GGA-PBE approximation [56]. $32 \times 32 \times 1$ Γ-centered Monkhorst-Pack $\boldsymbol{k}$ points and numerical parameters as presented in Tab 1.1 are used for the computation of the ground state. It has been confirmed, that the structural properties do not further improve if the plane-wave energy cutoff or the number of $\boldsymbol{k}$ points is increased, or the threshold for the Hellmann-Feynman forces is decreased. The approach is described in detail for germanene, however, the results are also mentioned for the remaining crystals. The impact of SOC is most important for the electronic properties, but can be safely neglected for the structural optimization.

The structure of the group-IV honeycomb crystals are determined by two parameters, the in-plane nearest-neighbor distance a (or the lattice constant a_0) and the buckling height Δ. The optimized geometries are obtained by minimizing the total energy as a

function of the lateral lattice parameter a. At each value of a, the atomic positions, for symmetry reasons, essentially the sheet buckling Δ, were fully relaxed to reduce the Hellmann-Feynman forces below 0.001 eV Å^{-1}. The energy of the crystal as a function of a is shown in Fig. 2.3 The energy as a function of the nearest-neighbor distance exhibits
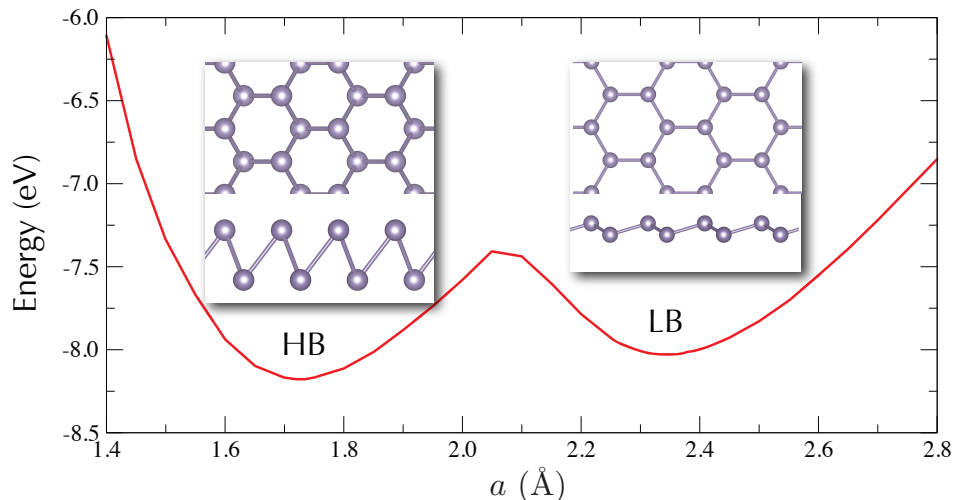
Figure 2.3: Energy as a function of the in-plane nearest-neighbor distance of 2D Ge in GGA-PBE. The inset shows the geometries of the high-buckled and low-buckled phase of germanene in top and side view.

two distinct minima at $a = 1.726$ Å and $a = 2.344$ Å. The corresponding buckling heights are $\Delta = 2.24$ Å (high-buckled (HB) phase) and $\Delta = 0.689$ Å (low-buckled (LB) phase), respectively. The HB phase is energetically favored, however, the important question is whether these geometries correspond to real local minima on the Born-Oppenheimer surface. Using the Parlinski-Li-Kawazoe method [118] as implemented in the PHONOPY code [119] based on the frozen-phonon approach as implemented in VASP the phonon dispersion can be investigated. It turns out, that the energetically favorable HB phase has imaginary frequencies and must be regarded unstable. Indeed, structural optimization of the HB structure on the (2×2) supercell tends to clustering (favored sp^3 bonding) of the system. Therefore, the HB structure does not correspond to a real local minimum, since it occurs only under the constraint of the (1×1) hexagonal unit cell with two atoms in the basis.

The LB structure of germanene also exhibits imaginary frequencies, but only at the Γ point of the BZ. However, these frequencies seemingly belong to particularly soft phonon modes and thus, only appear due to numerical reasons. The structural relaxation of a 7×7 supercell also does not lead to any distortions of the LB structure of germanene. Consequently, the LB structure is considered at least metastable, since it belongs to a real local minimum on the total-energy surface. The computed phonon dispersion and

conclusions agree with the literature [23].

In contrast to germanene, the same approach for graphene yields an atomically flat structure ($\Delta = 0$) with only one distinct energy minimum. Silicene and stanene also possess two distinct minima. Stability analysis by means of phonons yields unstable HB structures as in the case of germanene. For silicene, the LB structure is stable since no imaginary frequencies occur in the phonon dispersion. The stability of stanene is discussed controversially, some references suggest a stable LB phase [120], whereas others suggest a stable HB phase [121]. In this work only the LB phase is considered to be able to discuss chemical trends along the group-IV column of the periodic table of the elements.

The structural properties of all group-IV honeycomb crystals are summarized in Table 2.1. They are in agreement with previous findings [23, 122–126]. There are clear chemical

	C	Si	Ge	Sn
a_0 (Å)	2.468	3.868	4.060	4.673
a (Å)	1.425	2.233	2.344	2.698
Δ (Å)	0.00	0.45	0.69	0.85
v_F ($10^6\,\mathrm{m\,s^{-1}}$)	1.01 (0.83)	0.65 (0.53)	0.62 (0.52)	0.55 (0.48)
m^* (m_0)	0.000 (0.000)	0.001 (0.001)	0.007 (0.008)	0.029 (0.028)
E_g (meV)	0.0 (0.0)	1.9 (1.5)	33 (24)	101 (73)

Table 2.1: Structural and electronic parameters. Electronic quantities are derived from hybrid HSE06 calculations. The GGA results are given in parentheses. E_g and m^* are calculated with inclusion of SOC (without SOC, $E_g = m^* = 0$).

trends. The characteristic lateral geometry parameters a and a_0 and the buckling height Δ increase along the row C, Si, Ge, Sn. The increasing buckling amplitude indicates deviation from the pure sp^2 bonding and the formation of mixed $sp^2 - sp^3$ bonding. The sp^3 character also increases along the row C, Si, Ge, Sn. Indeed, the buckling amplitude Δ approaches more and more the value $\Delta_{sp^3} = a/(2\sqrt{6})$ for complete sp^3 bonding.

## 2.4 Electronic properties from first principles

2.4.1 GGA-PBE approach

The Kohn-Sham equations (1.17) for graphene, silicene, germanene, and stanene are solved. The corresponding band structures along high-symmetry lines of the 2D BZ are shown in Fig. 2.4. Additionally, the density of states (DOS) obtained within the tetrahedron

method [127] on a refined regular $\boldsymbol{k}$-point mesh with size $128 \times 128 \times 2$ (two $\boldsymbol{k}$ points in z direction for numerical reasons) is shown besides the band structures.
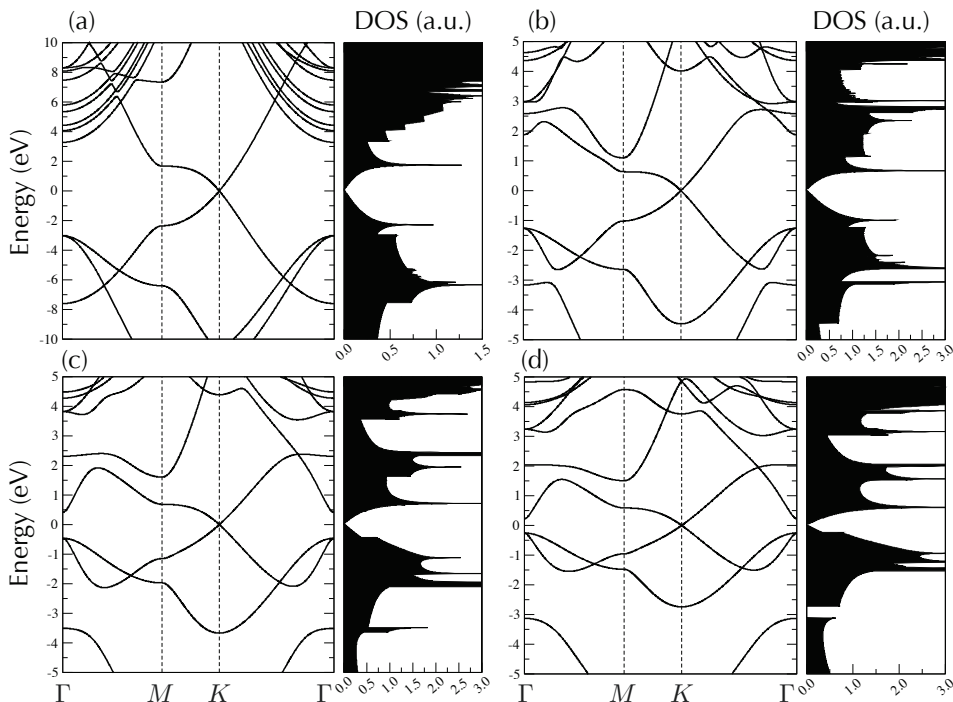
Figure 2.4: Band structure and density of states for (a) graphene, (b) silicene, (c) germanene and (d) stanene calculated within a DFT-GGA approach. The Fermi level is located at zero energy.

Within the DFT-GGA framework graphene, silicene, germanene and stanene represent a multi-valley zero-gap semiconducting character. Conical linear bands appear at the K and K' point independent of the group-IV crystal, which can also be seen from the linear DOS around the Fermi level (see e.g. [48]). The term zero-gap semiconductor is justified since, in contrast to metals, the DOS vanishes at the Fermi level. The approximation of linear bands in graphene is valid up to several eV away from the Fermi level, as displayed in Fig. 2.4(a). Although silicene, germanene and stanene are not perfectly sp^2 bonded systems, still conical linear bands appear at the K point which is due to the decoupling of the σ and π bands according to symmetry considerations [128]. In the DFT calculations also the atomic s and $p_{x,y}$ electrons are taken into account. These electrons mainly contribute to energetically low-lying bands, e.g., in graphene about 3 eV away from the Fermi level visible at the Γ point. For silicene, germanene and stanene these σ-derived bands shift more and more towards the Fermi level, however, the bandgap at Γ remains finite. Thus, the apex of the valence band Dirac cone around K and K' points still fixes the Fermi energy for undoped group-IV crystals. As an example, the orbitals contributing to the four (spin-degenerate) occupied bands in germanene are shown in Fig. 2.5.
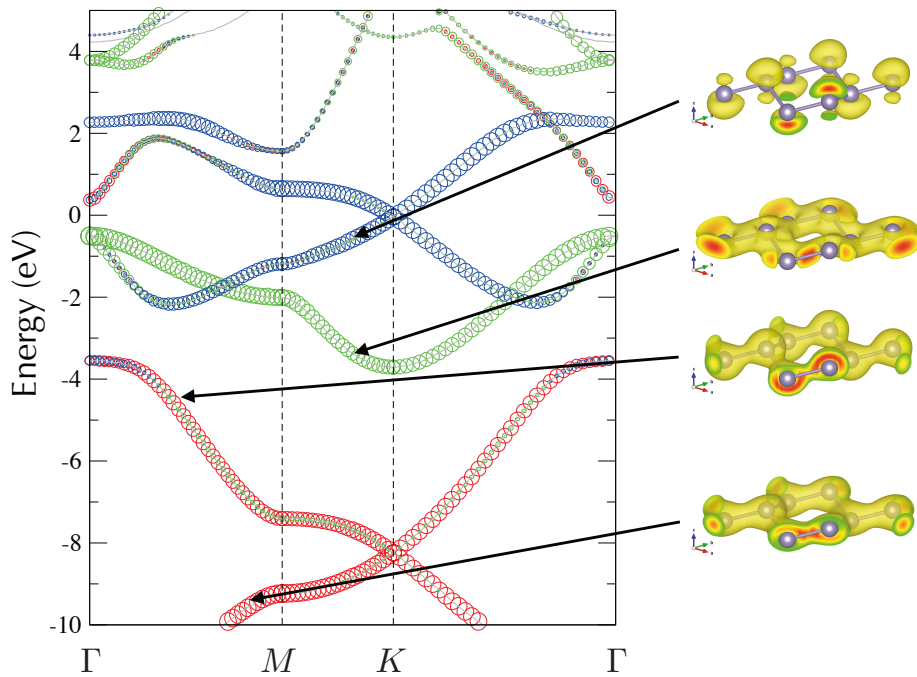
Figure 2.5: The orbital character of the bands in germanene: s (red), $p_{x,y}$ (green) and p_z (blue). Wave function squared (right) of the orbitals contributing to the four occupied bands at the $\boldsymbol{k}$ points indicated by the arrows.

The slope of the (isotropic) Dirac cone determines the Fermi velocity $v_F = \hbar^{-1}\partial\varepsilon(\boldsymbol{k})/\partial\boldsymbol{k}|_{\boldsymbol{k}\approx\boldsymbol{K}}$ of the charge carriers. The calculated values for all 2D group-IV crystals are given in Table 2.1. The Fermi velocity for freestanding graphene has been determined experimentally. Its value is about $1.1 \times 10^6\,\mathrm{m\,s^{-1}}$ [8]. The discrepancy between the experimental value and the DFT-GGA calculation is about 25%. The result is not surprising, since DFT is a ground-state theory and typically underestimates the valence-conduction-band energy distances.

2.4.2 Approximate quasiparticle corrections

Here the impact of quasiparticle corrections on the electronic band structure based on the HSE06 functional [37, 39] are studied. As stated in Sec. 1.3.6, the HSE functional simulates important features of the true quasiparticle band structure. The modification of structural properties of the crystals due to the HSE06 functional is neglected, although we may expect a small change of the lattice constant and buckling. However, usually small structural changes only marginally influence the electronic properties. Therefore, the lattice constants and buckling heights determined by DFT-GGA are kept fixed. The electronic band structure is obtained as explained in detail in Sec. 1.5.1. The band structures of all 2D honeycomb crystals are shown in Fig. 2.6.
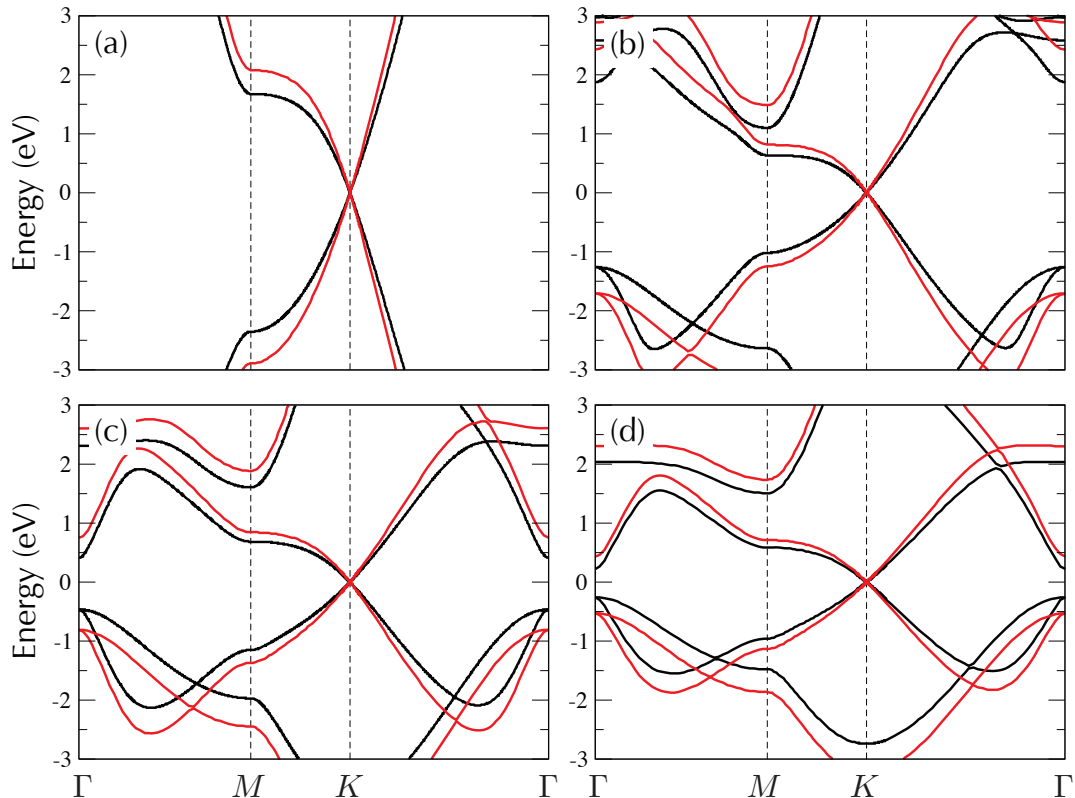
Figure 2.6: Comparison of the band structures along high symmetry lines in the 2D BZ of (a) graphene, (b) silicene, (c) germanene and (d) stanene in the DFT-GGA approach (black curves) and with quasiparticle corrections (red curves). The Fermi level is fixed at zero energy. SOC is not taken into account.

The approximate quasiparticle corrections by means of the HSE06 functional are zero at the Fermi level, thus, no bandgap is opened at the Dirac points. However, the valence band energies away from the Fermi level are shifted downwards, while the conduction band energies are shifted upwards compared to DFT-GGA band positions. The trend is clearly expected when starting a quasiparticle computation from a local or semilocal approach to XC. Consequently, the energy gaps outside K or K' are significantly opened while the wavevector dispersion, and thus the Fermi velocity, near K or K' is increased with respect to standard semilocal DFT calculations. The Fermi velocities are given in Table 2.1. As before the computed value of $1.01 \times 10^6 \, \mathrm{m \, s^{-1}}$ for graphene is compared to the experimental value of $1.1 \times 10^6 \, \mathrm{m \, s^{-1}}$ [8]. It clearly shows an improvement over the GGA result when quasiparticle effects are taken into account. The quasiparticle (QP) value $1.15 \times 10^6 \, \mathrm{m \, s^{-1}}$ using the GW approximation is slightly larger [73]. Larger values measured by means of angle-resolved photoemission spectroscopy (ARPES) for silicene [25] than those in Table 2.1 are very likely a consequence of the substrate influence. We conclude that the HSE functional simulates important features of the full QP theory.

## 2.4.3 Influence of spin-orbit interaction

We investigate the influence of SOC on the quasiparticle band structure, in particular close to the Dirac points. This requires much numerical effort. The convergence of the fundamental bandgap induced by SOC as a function of the number of $\boldsymbol{k}$ points is very slow when using hybrid functionals. The regular 2D $\boldsymbol{k}$-point meshes have to be carefully chosen since the convergence is strongly enhanced if the K and K' points are excluded from the regular $\boldsymbol{k}$-point mesh [129] as displayed in Fig. 2.7. $\boldsymbol{k}$ point meshes that can be represented as $3n \times 3n \times 1$ ($n \in \mathbb{N}$) (red line) include the Dirac points and converge remarkably slower than $\boldsymbol{k}$ meshes that exclude them (blue and green lines). Anyway, they converge against
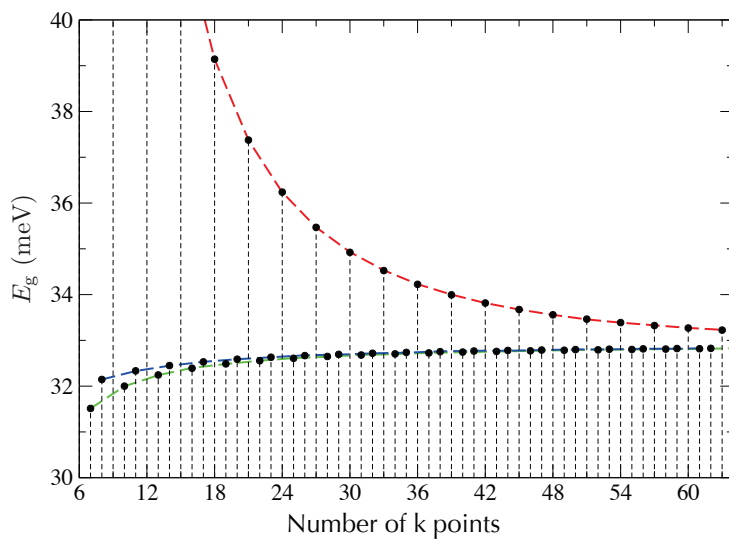
Figure 2.7: Electronic bandgap of germanene using the HSE06 functional at the Dirac point as a function of the number of $\boldsymbol{k}$ points in each reciprocal lattice direction. Colored lines are meant as guides to the eye. Details see text.

the same value if enough $\boldsymbol{k}$ points are used in the computation. Consequently, we apply a $32 \times 32 \times 1$ Γ-centered Monkhorst-Pack $\boldsymbol{k}$-point mesh [86] for all group-IV materials to compute their electronic properties. The HSE06 band structures of the four 2D honeycomb crystals along high-symmetry lines in the hexagonal BZ are plotted in Fig. 2.8. For silicene, germanene and stanene the inset also shows the linear dispersion around the K and K' point obtained without SOC in comparison to the dispersion with SOC. It can be seen that SOC induces a fundamental gap E_{gap} and, hence, massive Dirac particles with effective masses m^* close to the valence and conduction band edges near K (or K') points. We do not find a $\boldsymbol{k}$-induced splitting of the twofold degeneracy due to SOC, i.e., away from Γ. At least along high-symmetry lines we do not observe Rashba [130] or Dresselhaus [131, 132] components in the band structure, in agreement with other studies [133, 134]. At the Γ point a similar splitting of the fourfold degenerate uppermost valence band into two twofold degenerate valence bands occurs as in the germanium bulk. For graphene, the smallness of the SOC-induced E_{g} makes its precise HSE06 computation difficult. Since the size of the estimated bandgap E_{g} is about 0.02 meV, we only discuss the effect of SOC
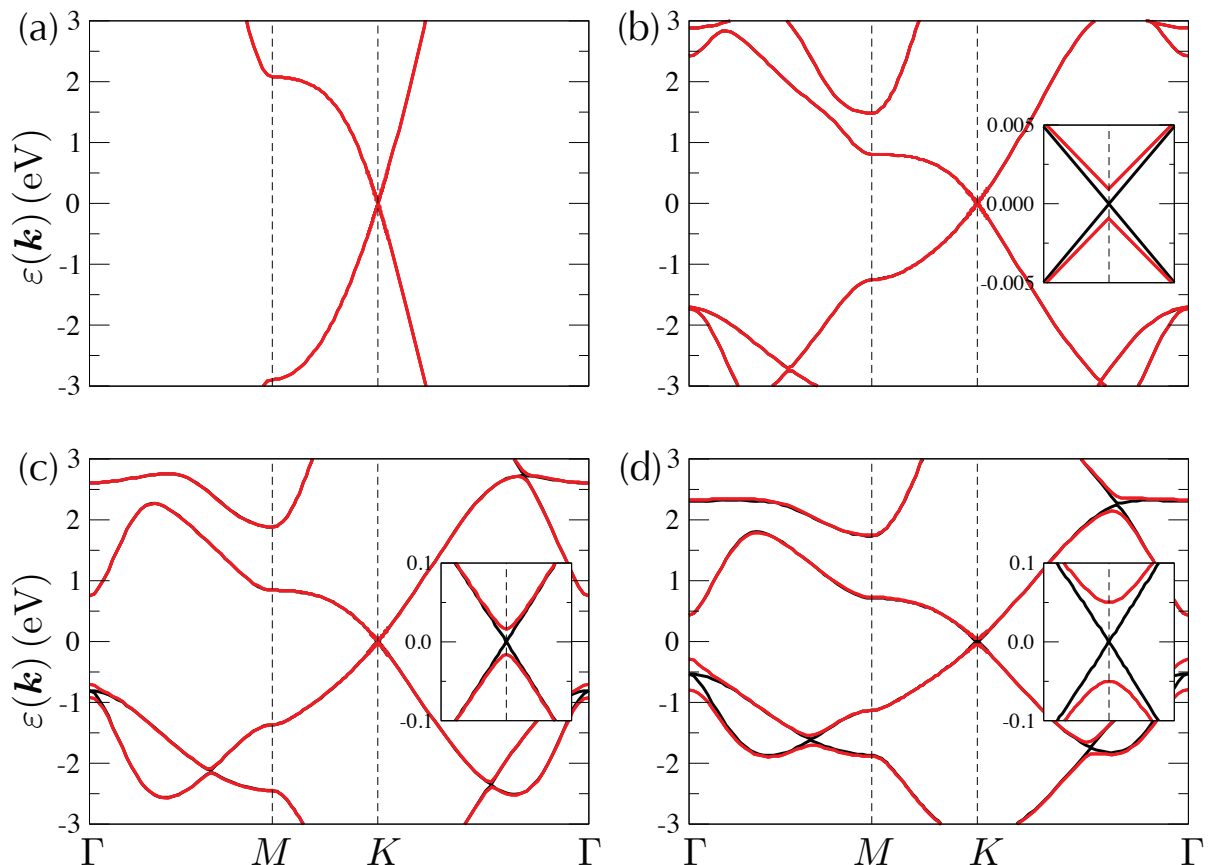
Figure 2.8: Approximate quasiparticle band structures of (a) graphene, (b) silicene, (c) germanene, and (d) stanene along high-symmetry lines of the 2D hexagonal BZ using the HSE06 functional including spin-orbit interaction. For silicene, germanene and stanene, the inset shows a magnification of the electronic bandgap around the Dirac point together with the band structure obtained without SOC (solid black lines).

for the other group-IV materials.

The electrons (+) and holes (−) in silicene, germanene and stanene in the vicinity of K or K' can be approximated by a dispersion relation of massive relativistic Dirac particles [116]

$$\varepsilon(\boldsymbol{k}) = \pm\sqrt{\left(\frac{E_{\mathrm{g}}}{2}\right)^2 + (\hbar v_F \Delta \boldsymbol{k})^2} \tag{2.8}$$

with $\Delta\boldsymbol{k}$ as the deviation of the 2D wavevector from its value at a K or K' point. The SOC-induced gaps E_{g} are also listed in Table 2.1. They follow the same clear chemical trend as the spin-orbit splittings Δ_{SO} in the 3D diamond structures of the group-IV materials mentioned above. The E_{g} values are, however, by one order of magnitude smaller. Thereby, the spin-orbit effects using non-local HSE06 XC potentials are significantly larger than those obtained within DFT-GGA as a consequence of the more localized quasiparticle states. Our findings in Table 2.1 are in agreement with E_{g} values in other recent DFT

computations with deviations less than 1 meV. Values E_{g} = 1.55 (Si), 23.0 (Ge), and 73.5 (Sn) meV have been given in the literature [30, 116, 135]. The finite gap gives rise to massive Dirac (electrons or holes) particles near a K or K' point with the effective mass

$$m^* = \frac{E_{\mathrm{g}}}{2v_F^2} \,. \tag{2.9}$$

Its values in Table 2.1 also show a clear increase with the atomic number of the group-IV element.

2.5 Optical conductivity and absorbance

Here we study if the direct relation of the absorbance to the fine-structure constant remains conserved in the presence of real-structure effects such as the actual Fermi velocity of the Dirac fermions and anisotropic deviations from the linear wave-vector dispersion around the K and K' Dirac points. The influence of the incomplete sp^2 hybridization and hence of the buckling of the honeycomb lattice is investigated in the case of silicene, germanene and stanene. The effect of the gauge of the electromagnetic field is discussed for vanishing photon wave vectors. All issues are investigated using ab-initio calculations of the dielectric function and the optical conductivity, respectively. For better insight into some aspects of the numerically results, tight-binding calculations are supplied as well.

Taking into account classical electrodynamics it is shown, how reflection, transmission and absorption of multilayer thin films are related to the optical conductivity of 2D crystals.

2.5.1 Numerical methods

The starting point for the calculation of the dielectric function or optical conductivity according to Eqs. (1.34) and (1.35) are the lattice parameters in Table 2.1 and basically exactly the same numerical set up in terms of the energetic cutoff, vacuum and $\boldsymbol{k}$-point mesh for the electronic ground state.

The frequency-dependent conductivity requires the calculation of optical transition matrix elements $M_{cv}(\boldsymbol{k}, \boldsymbol{q})$ according to Eq. (1.36) between occupied valence and empty conduction bands in the irreducible part of the Brillouin zone. Therefore, also a large number of conduction bands in addition to the four valence bands are needed. Without SOC, 16 bands in total are needed for converged optical spectra below photon energies of $\hbar\omega = 10$ eV, whereas with SOC twice the number of bands are needed. In general, a $400 \times 400 \times 1$

($128 \times 128 \times 1$) Γ-centered $\boldsymbol{k}$-point grid is used for the optical calculations in GGA-PBE (HSE06). For the calculation of the screened Fock exchange interaction in the HSE06 XC the grid can be reduced to $32 \times 32 \times 1$ $\boldsymbol{k}$ points. Two additional refined grids are applied, each including about 13700 (869) $\boldsymbol{k}$ points within a circle of radius $0.05 \times 2\pi/a$ and $0.005 \times 2\pi/a$ in the IBZ, respectively, around one single K point in GGA (HSE06). The numerical parameters are summarized in Table 2.2.

	bands	coarse $\boldsymbol{k}$ mesh	refined $\boldsymbol{k}$ mesh
GGA-PBE	16 (32)	$400 \times 400 \times 1$	13700
HSE06	16 (32)	$128 \times 128 \times 1$	869

Table 2.2: Numerical parameters used in the calculation of the frequency-dependent optical conductivity $\sigma(\omega)$ within the PBE and HSE06 functional, respectively. Details can be found in the text.

Within the semilocal GGA the ground state is determined by the electron density. Thus, the ground-state density is calculated self-consistently using $32 \times 32 \times 1$ $\boldsymbol{k}$ points, whereas the optical properties are calculated non-self-consistently at arbitrary $\boldsymbol{k}$ points. In contrast, the approach with the HSE06 functional is more complicated. Every HSE calculation is necessarily self-consistent, since due to the non-locality the electronic ground state is a functional of the wave functions. Therefore, the same zero-weight $\boldsymbol{k}$-points trick is applied as already discussed for the calculation of the band structure (Sec. 1.5.1). Here, for exact calculations of the optical conductivity, also the $\boldsymbol{k}$-point weights in the irreducible BZ have to be restored and taken into account after the calculation is done.

Another issue is related to the Fermi level if the HSE06 functional is used. It has been pointed out earlier, that the Dirac point should be excluded from the $\boldsymbol{k}$ point mesh for better convergence of the Fock exchange energy and consequently, also the SOC-induced bandgap. However, the inclusion of the Dirac point is no source of error only if the $\boldsymbol{k}$-point weight is zero, since such points do not contribute to the calculation of the Fock exchange energy. Of course, in a calculation where some $\boldsymbol{k}$ points have zero weights while others have nonzero weights, the Fermi level may lie below the apex of the Dirac cone. Therefore, the Fermi level must also be adjusted accordingly. We have modified the VASP code in such a way, that *all* transition matrix elements are written to a file, which allows the change of occupation numbers afterwards and a calculation of the optical conductivity directly by means of Eqs. (1.34) and (1.35).

The optical conductivity $\sigma(\omega)$ of the 3D supercell arrangement of the 2D group-IV honeycomb crystals is calculated in the supercell approximation and given by Eq. (1.34) and (1.45). The 3D conductivity can be related to the 2D one $\sigma_{2D}(\omega)$ by changing from

a 3D to a 2D sample. For the superlattice arrangement the relation is mediated by the superlattice dimension L (distance of adjacent crystal sheets in the supercell)

$$\sigma_{2D}(\omega) = L \, \sigma(\omega). \tag{2.10}$$

The real part of the 2D optical conductivity is attributed to losses in the atomically thin sheet. It will be shown in Sec 2.6.2 that the (thickness-independent) optical absorption (or absorbance) $A(\omega)$ of such a sheet for normal incidence is directly related to $\sigma_{2D}(\omega)$ and well approximated by means of

$$A(\omega) \simeq Re \, \tilde{\sigma}_{2D} \tag{2.11}$$

where the dimensionless normalized quantity $\tilde{\sigma}_{2D}(\omega)$ is introduced according to (1.58). Hence, it now appears that there is an approximate relation between the imaginary part of the dielectric function of the 3D cell and the absorption, at least in the limit of zero reflectivity,

$$A(\omega) \simeq \frac{\omega}{c} L \, Im \, \epsilon(\omega) . \tag{2.12}$$

2.5.2 Independent-particle results in DFT-GGA

Using GGA-PBE without SOC the resulting electronic band structure is conical around the K and K' points of the 2D hexagonal BZ as displayed in Fig. 2.6. The eigenvalues $\varepsilon_\nu(\boldsymbol{k})$ of the Kohn-Sham equation (1.17) are used to illustrate the optical interband transition energies $\Delta\varepsilon_{cv}(\boldsymbol{k}) = \varepsilon_c(\boldsymbol{k}) - \varepsilon_v(\boldsymbol{k})$ and the joint density of states JDOS$(\hbar\omega) = \sum_{c,v,\boldsymbol{k}} \delta(\hbar\omega - \Delta\varepsilon_{cv}(\boldsymbol{k}))$. Results for the four honeycomb sheet materials graphene, silicene, germanene and stanene are given in Fig. 2.9. They illustrate how and with which JDOS the energy conservation is fulfilled in the optical absorption for a given photon energy $\hbar\omega$. In the range of very low photon energies, whose limit decreases along the row C, Si, Ge, and Sn, the isotropic Dirac cones are also visible in the joint band structure at K for small energies. The Dirac cones give rise to a linear increase of JDOS(ω) in the low-energy region $\hbar\omega$. For higher interband energies, the critical points $\boldsymbol{k}_0$ and van Hove singularities $\nabla[\varepsilon_c(\boldsymbol{k}) - \varepsilon_v(\boldsymbol{k})]|_{\boldsymbol{k}=\boldsymbol{k}_0} = 0$ appear. Their energies are indicated by horizontal lines. They indeed give rise to spectral features in the JDOS beginning near 4.0 eV (graphene), 1.6 eV(silicene), 0.9 eV (germanene), and 0.5 eV (stanene). The weak intensity of the lowest van Hove singularity for germanene at 0.9 eV related to the lowest interband transition at Γ is due to its small effective interband mass of the σ bands and the M_0 character of the singularity. Division of JDOS(ω) by $\hbar\omega$ makes this singularity visible in the absorbance spectrum of germanene (Fig. 2.10), which is approximately described by (2.11). In general quasiparticle and excitonic effects are supposed to have an impact on
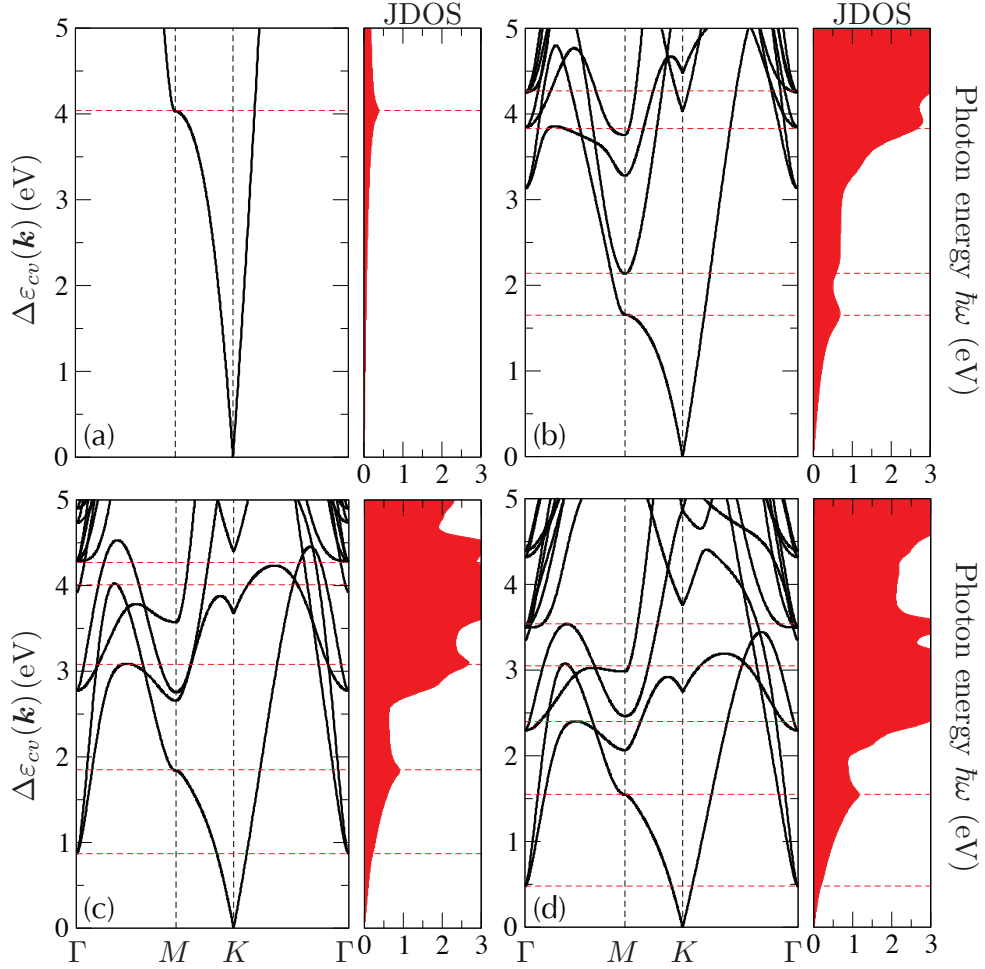
Figure 2.9: Interband transition energies along high-symmetry lines in the BZ for (a) graphene, (b) silicene, (c) germanene, and (d) stanene. The red horizontal lines indicate energies of van Hove singularities which give peak structures in the absorbance in Fig. 2.10. The resulting joint density of states JDOS(ω) are displayed in addition [in units eV^{-1}/cell]

the computed optical properties of the sheet crystals. However, quasiparticle and excitonic effects tend to compensate each other [136], thus, the approximations presented so far are reasonable in particular for low photon energies. In reality, there is still the open question if the group-IV honeycomb crystals eventually are excitonic insulators [137], which will not be addressed here. An influence on the spectra is expected for very small photon energies.

Low-frequency absorbance

The frequency dependence of the absorbance (2.11) is calculated numerically from Eq. (1.44) for the optical conductivity using the ab-initio electronic structure, more precisely the band structure $\varepsilon_\nu(\boldsymbol{k})$ and Bloch functions $|\nu\,\boldsymbol{k}\rangle$. The obtained interband structures are
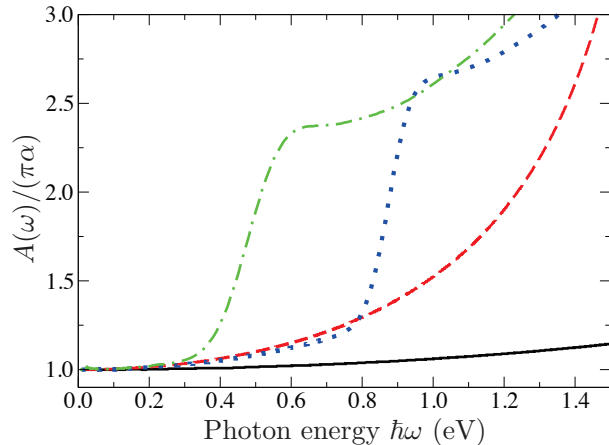
Figure 2.10: Optical absorption spectrum $A(\omega)$ calculated within the approximation of independent Kohn-Sham particles with the GGA-PBE XC functional for graphene (black solid line), silicene (red dashed line), germanene (blue dotted line), and stanene (green dash-dotted line) vs. photon energy.

plotted in Fig. 2.9 in a small range of photon energies for the four studied 2D crystals. The longitudinal representation of the optical transition matrix elements (1.36) has been used. First, we investigate the resulting infrared absorbance as displayed in Fig. 2.10. Indeed, for graphene, we observe the result known from measurements [44, 138] and from the theoretical prediction assuming massless Dirac fermions and the vector-potential (transverse) gauge [44], that in the limit $\hbar\omega \to 0$, the absorbance approaches to $A(0) = \pi\alpha$ (=0.022925) with $\alpha = e^2/\hbar c$ in excellent agreement with the predicted value and also in good agreement with the experimental findings for practically undoped graphene [73, 138]. We find that this holds also for silicene and germanene and that the numerical values are $A(0) = 0.02293$ (graphene), 0.02290 (silicene), 0.02292 (germanene), and 0.02293 (stanene). Hence, the absorbance $A(0)$ is independent of the sheet buckling, i.e., of the strong deviations from the sp^2 hybridization in silicene, germanene and stanene. The reason is that the point-group symmetry of a 2D honeycomb lattice is conserved independent of the buckling.

The result in Fig. 2.10 has been found within a (normal) Fermi-liquid approximation taking into account the full band structure $\varepsilon_\nu(\boldsymbol{k})$ and all interband transition matrix elements between occupied and empty Bloch states in the entire 2D hexagonal BZ. The result thus holds for all group-IV honeycomb crystals for low frequencies. Important ingredients are of course the linear $\boldsymbol{k}$ dispersion of the interband energies $\Delta\varepsilon_{cv}(\boldsymbol{k})$ (see Fig. 2.9) for extremely small photon energies and precise values of the optical matrix elements between π and π^* bands at the corner points of the BZ, $\boldsymbol{k} = K$ or K', independent of the 2D material.
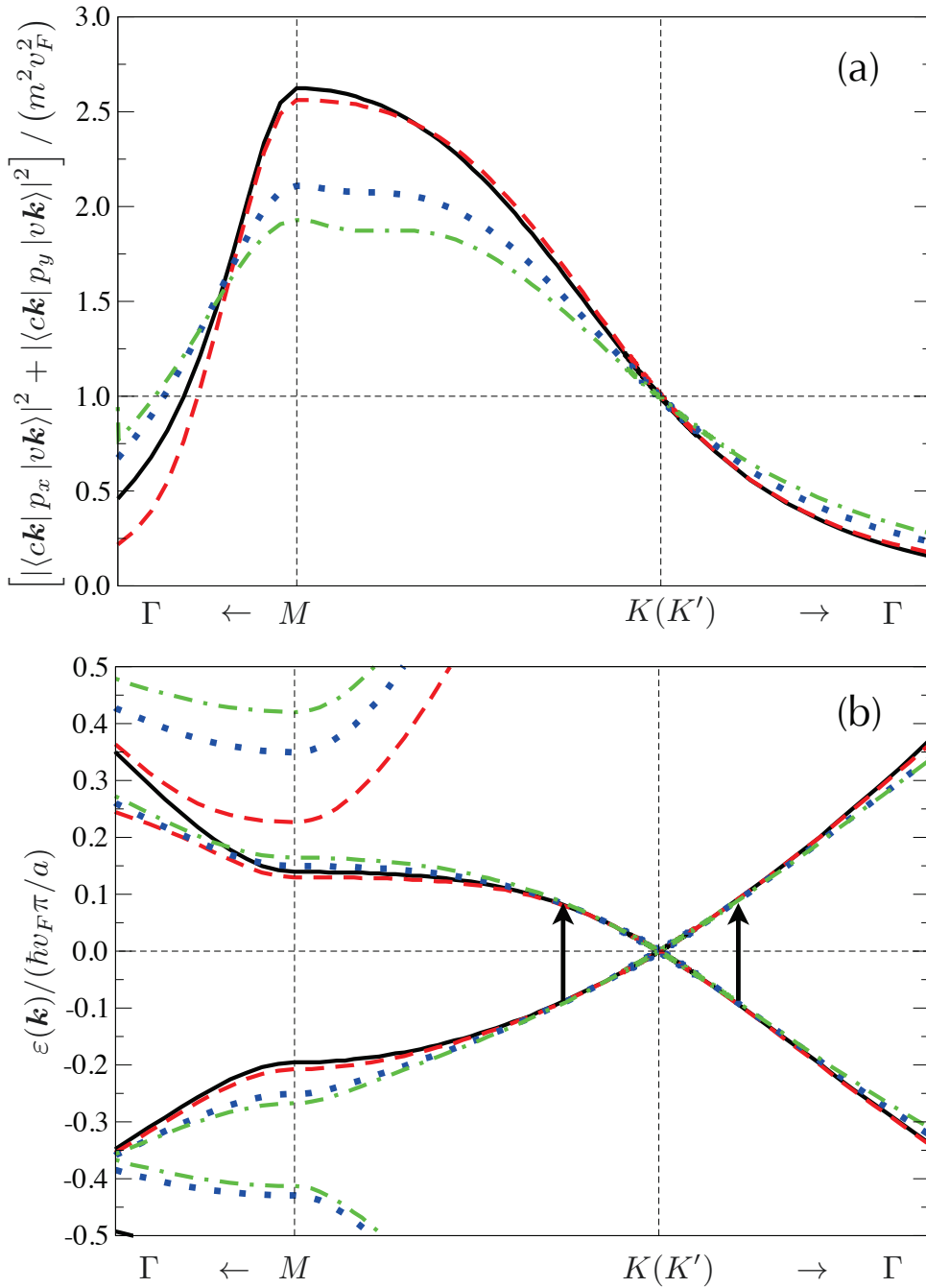
Matrix elements

The matrix elements for the lowest interband transitions between the highest valence band v and the lowest conduction band c are plotted in Fig. 2.11(a) along three high-symmetry

lines including the BZ boundary KM (or $K'M$). For comparison, the corresponding π and π^* bands, that are involved in the optical transitions, are shown in Fig. 2.11(b). Of course, away from the BZ boundary near K or K' the first σ and σ^* bands along the ΓM line and in its vicinity appear for silicene, germanene and stanene close to the π and π^* bands. In Fig. 2.11, the band energies and the momentum matrix elements are normalized to their characteristic values $\hbar v_F \pi/a$ and $m^2 v_F^2$, respectively, in the Dirac-Weyl theory, i.e., near K (or (K')), in order to demonstrate that in the studied energy and wave-vector regions they are rather independent of the material.

Most important for the result $A(0) = \pi\alpha$, obtained within the independent-particle approximation and the ab-initio electronic structure, are the finite interband transition matrix elements around K (or K') in Fig. 2.11(a). For their explicit computation, the longitudinal representation (1.36) has been used. The results presented in Fig. 2.11(a) are, however, rewritten as the momentum matrix elements according to the relation between Eqs. (1.36) and (1.40). They indicate that for low photon energies the optical properties, which according to the interband structure and the joint density of states are due to $\pi \to \pi^*$ transitions, are dominated by contributions from $\boldsymbol{k}$ points near the BZ boundary along the MK (or MK') lines. The matrix elements possess a maximum at an M point where, however, the underlying atomic symmetry of the wave functions is modified with respect to that at a K or K' point. The effects of the group-IV material and the sheet buckling are small. More precisely, at K or K' points the momentum matrix-element squares are the same in units of $m^2 v_F^2$. Indeed, the numerical treatments yield values 0.995 (graphene), 0.995 (silicene), 1.004 (germanene) and 0.990(stanene) very close to the value 1 (see below) as expected. The numbers also illustrate the quality of the PAW functions used for the calculation of optical properties [139]. In general, the normalized momentum matrix element appearing in Fig. 2.11(a) only exhibits a weak wave-vector dispersion. At M, a minor reduction occurs along the row C→Si→Ge→Sn, whereas along $K\Gamma$ and $M\Gamma$ an opposite tendency is observed. The chemical trends are in rough agreement with the energy differences of the π and π^* bands in Fig. 2.11(b). Along KM, the interband energies are increased, while they are slightly reduced from K toward Γ.

Analytical approach

The result $A(0) = \pi\alpha$ can be also analytically derived, using the tight-binding method [140, 141], but restricting only to the p_z-orbitals and their nearest-neighbor interaction. Inserting Eq. (1.35) into Eq. (2.11), for normal incidence, and, thus, in-plane polarization of the light, the optical absorbance of a two-dimensional crystal for $\omega > 0$ is described by

Figure 2.11: (a) Transition matrix elements of the pure $\pi \to \pi^*$ transitions along high-symmetry lines in the BZ for graphene (black solid line), silicene (red dashed line), germanene (blue dotted line), and stanene (green dot dashed line). The longitudinal representation of the matrix elements (1.36) has been used in the numerical calculations. (b) For illustration, the π and π^* bands that are involved in the optical transitions are also shown. The transitions are indicated by vertical arrows.

(spin-degeneracy not yet taken into account)

$$A(\omega) = \frac{4\pi^2 e^2 \omega}{c\,A} \sum_{c,v} \sum_{\boldsymbol{k}} |M_{cv}(\boldsymbol{k}, \boldsymbol{q})|^2 \delta(\varepsilon_c(\boldsymbol{k}) - \varepsilon_v(\boldsymbol{k}) - \hbar\omega), \qquad (2.13)$$

where the area $A = V/L$ of the primitive cell of the 2D crystal has been introduced. All interband transitions between Bloch states $|v\,\boldsymbol{k}\rangle$ with energy $\varepsilon_v(\boldsymbol{k})$ and $|c\,\boldsymbol{k}\rangle$ with energy $\varepsilon_c(\boldsymbol{k})$ are taken into account. Within the transversal gauge, the transition matrix elements $M_{cv}(\boldsymbol{k})$ (1.40) are directly related to the momentum matrix elements $\langle c\,\boldsymbol{k}|p_x|v\,\boldsymbol{k}\rangle$ and $\langle c\,\boldsymbol{k}|p_y|v\,\boldsymbol{k}\rangle$ of the in-plane momentum operator.

In the limit of vanishing frequencies $\omega \to 0$, only the lowest π^*-like conduction band $c = +$ and the highest valence band $v = -$ near K and K' points contribute to the interband absorption (cf. with Fig. 2.9). For symmetry reasons, honeycomb crystals are optically isotropic for in-plane polarization, which is accounted for by choosing e.g. $\boldsymbol{q} = q(\boldsymbol{e}_x + \boldsymbol{e}_y)/\sqrt{2}$ in the matrix element (1.40). Together with the replacement of the wave-vector sum in Eq. (2.13) by an integral over the BZ one finds

$$A(\omega) = 2\frac{4\pi^2 e^2 \omega}{c\,A} \frac{\hbar^2}{m^2(\hbar\omega)^2} \frac{A}{(2\pi)^2} \frac{1}{2} \sum_{j=x,y} \int_{\mathrm{BZ}} d^2\boldsymbol{k}\, |\langle +; \boldsymbol{k}|p_j|-; \boldsymbol{k}\rangle|^2$$
$$\times \delta(\varepsilon_+(\boldsymbol{k}) - \varepsilon_-(\boldsymbol{k}) - \hbar\omega)\,, \qquad (2.14)$$

where the spin degeneracy of the bands is accounted for by an additional factor of 2. The two bands of the lowest interband pair of the studied 2D zero-gap semiconductor form Dirac cones at the three K and K' points $k_{oi}\,(i = 1 - 6)$ (see Fig. 2.9). Because of the energy conservation in Eq. (2.13) we restrict the $\boldsymbol{k}$ integral to the six important regions in the BZ from which the principal contributions to the optical absorption are expected for low photon energies. Thereby, we have to take in mind that groups of three K (K') points are equivalent and only one third of each environment of a K (K') point belongs to the BZ. So we have in total to study only two nonequivalent $\boldsymbol{k}_{oi}$ (one K and one K') points with their full environment. Because of the convergence of all integrals we extend these environments to infinite.

The bands in Fig. 2.11(b) forming the Dirac cones at each $\boldsymbol{k}_{oi}$ are

$$\varepsilon_\pm(\boldsymbol{k}_{oi} + \Delta\boldsymbol{k}) = \pm\hbar v_F |\Delta\boldsymbol{k}| \qquad (2.15)$$

with $\Delta\boldsymbol{k} = \boldsymbol{k} - \boldsymbol{k}_{oi}$. The Fermi velocity v_F in Table 2.1 characterizes the linear band

dispersion. Then, Eqs. (2.13) and (2.14) give rise to

$$A(\omega) = \frac{\alpha\hbar}{m^2\omega} \sum_{i=1}^{2} \sum_{j=x,y} \int_{\text{BZ}} d^2\boldsymbol{k} \, |\langle +; \boldsymbol{k}_{oi} + \Delta\boldsymbol{k}|p_j|-; \boldsymbol{k}_{oi} + \Delta\boldsymbol{k}\rangle|^2$$
$$\times \delta(2\hbar v_F|\Delta\boldsymbol{k}| - \hbar\omega),$$

(2.16)

where the Sommerfeld fine-structure constant $\alpha = e^2/(\hbar c) \simeq 1/137.036$ has been introduced. The strength of the optical transitions between the Dirac cones of electrons and holes is determined by the squares of the momentum matrix elements between the valence band $v = -$ and the conduction band $c = +$ [see Fig. 2.11(a)]. We investigate them near a K (or K') point $\boldsymbol{k}_{oi}$. We assume [and indeed numerically found in Fig. 2.11(a)] that the transitions, despite their vanishing excitation energy, are dipole-allowed at $\boldsymbol{k} = \boldsymbol{k}_{oi}$. Their strength is given by $D = \sum_{j=x,y} \langle +; \boldsymbol{k}_{oi} + \Delta\boldsymbol{k}|p_j|-; \boldsymbol{k}_{oi} + \Delta\boldsymbol{k}\rangle|^2$. At such a Dirac point $\boldsymbol{k}_{oi}$, in the limit $\Delta\boldsymbol{k} \to 0$, the two Bloch functions $|+; \boldsymbol{k}_{oi}\rangle$ and $|-; \boldsymbol{k}_{oi}\rangle$ approach each other (apart from a phase factor). This is shown in Fig. 2.12 where the square moduli of the eigenstates are depicted for silicene. The squares are identical for the
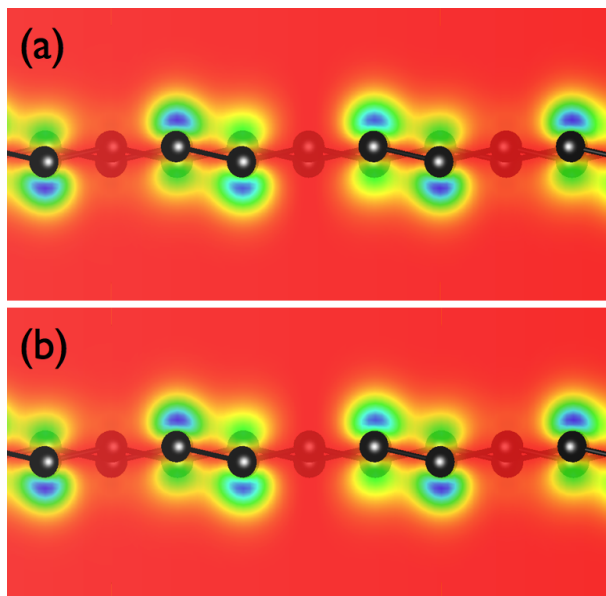
Figure 2.12: Wave-function squares of silicene for the highest occupied π state (a) and the lowest unoccupied π^* state (b) at K. The atomic positions in the isolated Si sheet indicate the buckled honeycomb geometry [14].

lowest unoccupied state and the highest occupied state at K and K' (not shown). Their symmetry and the maxima to find an electron or hole are identical. This can also be immediately seen using a tight-binding approximation with p_z orbitals localized at A and B atoms [140]. Consequently, at K or K', the strength can be approximately replaced by $D = \sum_{j=x,y} \langle \pm; \boldsymbol{k}_{oi}|p_j|\pm; \boldsymbol{k}_{oi}\rangle|^2$, i.e., formally by intraband transition matrix elements. For intraband matrix elements, it however holds $\langle \nu; \boldsymbol{k}|\boldsymbol{p}|\nu; \boldsymbol{k}\rangle = \frac{m}{\hbar}\nabla_{\boldsymbol{k}}\varepsilon_\nu(\boldsymbol{k})$. Together with

Eq. (2.15) then the total strength is found to be

$$D = (mv_F)^2 \tag{2.17}$$

in complete agreement with the ab-initio calculations in Fig. 2.11(a)]. This result determines the empirical parameter M in the nearest-neighbor tight-binding description of Grüneis et al. [140] by relating the Fermi velocity to M by means of $|M| = \sqrt{\frac{8}{3}} mv_F$.

With the value (2.17) of the momentum matrix element at a K or K' point it follows from Eq. (2.16) in the vanishing frequency limit,

$$A(\omega) = 2\frac{\hbar v_F^2}{\omega}\alpha \int d^2(\Delta\boldsymbol{k})\delta(2\hbar v_F|\Delta\boldsymbol{k}| - \hbar\omega). \tag{2.18}$$

Interestingly, similar integrals appear in a time-dependent formulation of the response of Dirac-Weyl particles [142]. Finally, we obtain

$$A(\omega) = 2\frac{\hbar v_F^2}{\omega}\alpha\frac{2\pi\hbar\omega}{(2\hbar v_F)^2} = \pi\alpha. \tag{2.19}$$

In the limit of vanishing optical transition energies, the crystal-material dependence in the matrix elements and that in the interband energies compensate each other. Indeed, the infrared absorbance is determined by a universal constant, the Sommerfeld fine-structure constant for all honeycomb crystals formed by only one group-IV element.

Region of van Hove singularities

In contrast to the behavior in the infrared spectral region in Fig. 2.10, the absorbance shows completely different frequency variations for the four 2D honeycomb materials graphene, silicene, germanene, and stanene in the visible and ultraviolet spectral regions, as shown in Fig. 2.13. The main reason is related to the different band structures [see Fig. 2.11(b)], especially the interband ones in Fig. 2.9. The van Hove singularities in the joint density of states in Fig. 2.9 and the energy dependence of the optical matrix elements determine the lineshape of the absorbance. The peaks and shoulders in $A(\omega)$ can be almost related to minima (M_0), maxima (M_2) or saddle points (M_1) in the 2D interband band structure and JDOS [48] (as indicated by dotted horizontal lines in Fig. 2.9), respectively. Because of the strong transition strength at the M point in the 2D BZ [see matrix elements in Fig. 2.11(a)] the saddle point in the difference $\varepsilon_c(\boldsymbol{k}) - \varepsilon_v(\boldsymbol{k})$ of the lowest conduction band (π^*-like) and highest valence band (π-like) gives rise to a pronounced peak at 4 eV (graphene), 1.6 eV (silicene), 1.7 eV (germanene), or 1.5 eV (stanene). Of course, the true
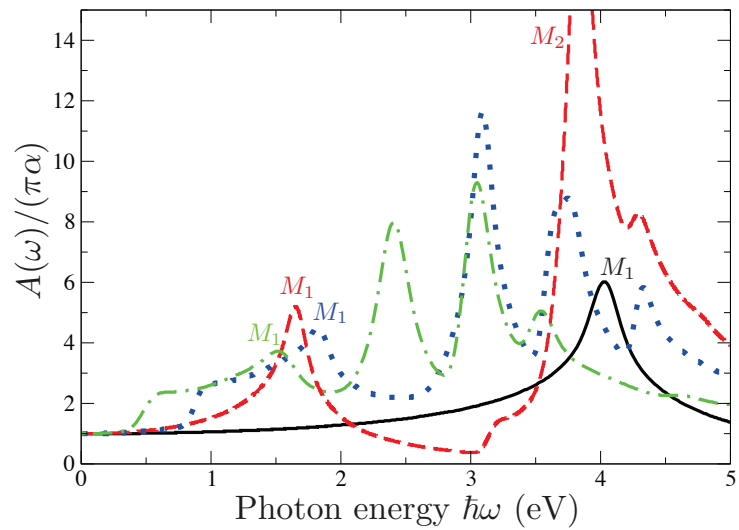
Figure 2.13: Spectral absorbance (in units of $\pi\alpha$) for graphene (black solid line), silicene (red dashed line), germanene (blue dotted line), and stanene (green dash dotted line).

position should be somewhat shifted to higher energies due to quasiparticle and excitonic effects, e.g., by 0.5 eV as shown for graphene [73]. The other spectral features appearing for silicene, germanene and stanene can also be explained in terms of the joint band structure and density of states in Fig. 2.9. The right-handed step [48] at $\hbar\omega = 0.9$ eV for germanene is in agreement with the 2D nature and the minimum character of the lowest interband transition at Γ. The absorbance feature near $\hbar\omega = 3.1$ eV is related to manifold contributions from M_0, M_1, and M_2 at the ΓM and MK lines (see Fig. 2.9), enforced by high JDOS due to several band crossings. The most pronounced structure in the spectrum for silicene at $\hbar\omega = 3.9$ eV is mainly related to the M_2 maximum of the interband transition energy at the ΓM line. However, there are also contributions from M_0 singularities at Γ, M, and K points as well as M_1 on the MK lines. Also the remaining features in the spectra of Fig. 2.13 can be approximately related to critical points and van Hove singularities in Fig. 2.9.

Gauge invariance of the absorbance

The absorbance of the four crystals graphene, silicene, germanene, and stanene is displayed in Fig 2.14 versus a wide frequency range of photon energies. The two different gauges of the electromagnetic field expressed by the two types transition matrix elements (1.36) and (1.40) have been applied, where the implementation within the PAW method of Gajdoš *et al.* [80] is used. The figure clearly demonstrates that within the PAW approach the longitudinal and transversal expressions for the frequency-dependent absorbance yield identical results for the energy positions of the spectral features as peaks and shoulders. This is a consequence of the identical joint density of states used. However, also the peak heights are more or less independent of the used description of the transition matrix
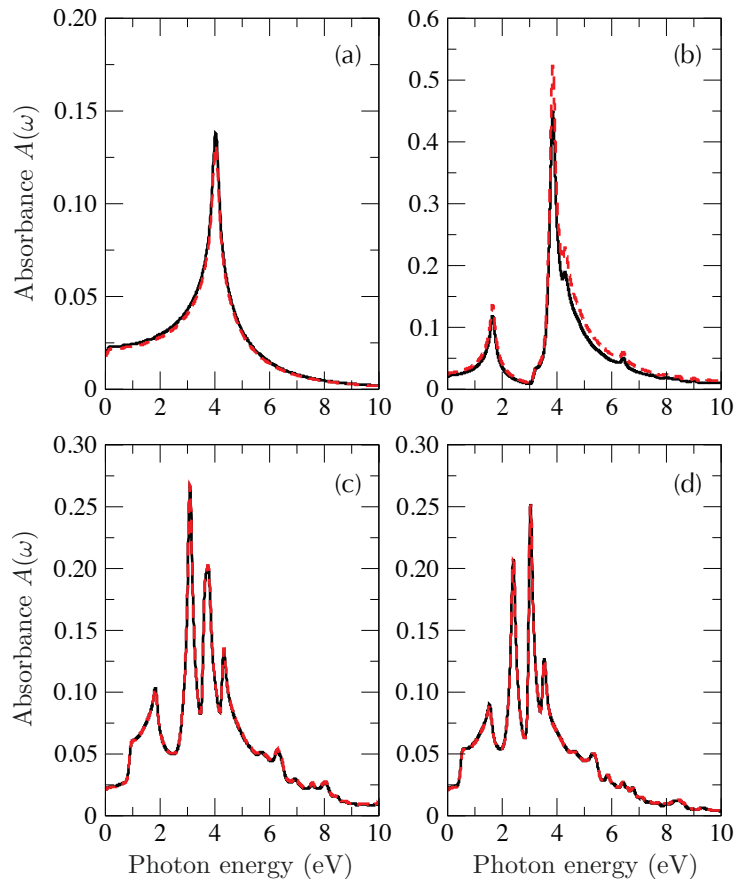
Figure 2.14: The frequency-dependent absorbance for (a) graphene, (b) silicene, (c) germanene, and (d) stanene. Besides the longitudinal gauge (1.36) (black solid line) also the transversal gauge (1.40) (red dashed line) has been used.

elements, at least for C-, Ge- and Sn-based sheets. This fact numerically confirms the assumption that the PAW approach generates all-electron wave functions and eigenvalues for the valence and conduction states [139]. The fictitious all-electron potential is local in space and hence leads to the strict relation between the matrix elements in Eqs. (1.36) and (1.40). Only for Si the peak intensities are slightly reduced when the longitudinal expression is applied for $A(\omega)$. The same effect has been observed for the absorption spectra of bulk silicon [80]. The deviation is mainly a consequence of the numerical description. The authors [80] argued that the discrepancies between the two gauges may be compensated by the inclusion of d state projectors and d one-center terms within the PAW spheres.

2.5.3 Quasiparticle effects and SOC

The absorbance of group-IV honeycomb crystals exhibits the peculiarity that the optical absorption is related to the fine-structure constant independent of the group-IV atom, the

sheet buckling, and the orbital hybridization in the limit of vanishing photon frequencies. On the other hand, one knows that semilocal DFT functionals rather accurately predict ground-state properties, but fail to predict excited state properties such as the optical bandgap in non-metals and the correct frequency dependence of the dielectric function. However, here we deal with zero-gap semiconductors (at least without SOC). Since in zero-gap semiconductors with Dirac cones only the Fermi velocity in the vicinity of the Dirac points changes due to quasiparticle effects, it should be possible to determine the optical conductivity (or absorbance) in the low-frequency regime without applying more sophisticated approaches to the electron-electron interaction, such as the many-body perturbation theory within the GW approximation, or the Bethe-Salpeter equation to account for excitonic effects. Consequently, we consider quasiparticle effects only approximately by means of the HSE06 functional, which yields a reasonable description of the quasiparticle band structure and wave functions, even including SOC.

In contrast, the increasing importance of SOC on the electronic properties for heavy group-IV atoms and the deformation of the Dirac cones near the K and K' points ask for a more detailed investigation of the impact of the SOC on the optical properties, therefore, we studied the optical absorbance by means of Eq. (2.11). The optical absorbance resulting from the independent-quasiparticle computations for all group-IV honeycomb crystals as a function of the photon energy is shown in Fig. 2.15. Without SOC the low-frequency absorbance approaches the well-known limit $A(\omega \rightarrow 0) = \pi\alpha$ as demonstrated earlier for independent Kohn-Sham electrons. However, using the HSE approach, the optical absorption peaks are blueshifted due to quasiparticle corrections. In a wide frequency range the optical absorbance taking into account SOC shows a very good overall agreement with the absorbance obtained without SOC. However, a more detailed analysis reveals a remarkable modification of the optical absorbance close to the fundamental absorption edge. For $\hbar\omega < E_g$ the absorption vanishes, while for $\hbar\omega > E_g$ the absorbance is significantly increased for $\hbar\omega \rightarrow E_g$. This behavior is particularly pronounced for germanene (Fig. 2.15(c)) and stanene (Fig. 2.15(d)). Within our numerical accuracy we estimate the absorbance is enhanced by a factor of two at $\hbar\omega = E_g$ due to SOC.

This peculiar lineshape of the absorbance in the vicinity of the fundamental absorption edge asks for a detailed explanation. In general, it is a consequence of the relativistic band dispersions (2.8) and the optical matrix elements (2.16) modified due to the inclusion of SOC when calculating the imaginary part of the dielectric function. The modified band dispersion is illustrated in Fig. 2.8. The strength of the corresponding interband transitions is displayed in Fig. 2.16. As an example we study the optical matrix elements between the highest occupied and the lowest unoccupied Bloch bands of germanene along the two high-symmetry directions $K\Gamma$ and KM. The optical transition matrix elements
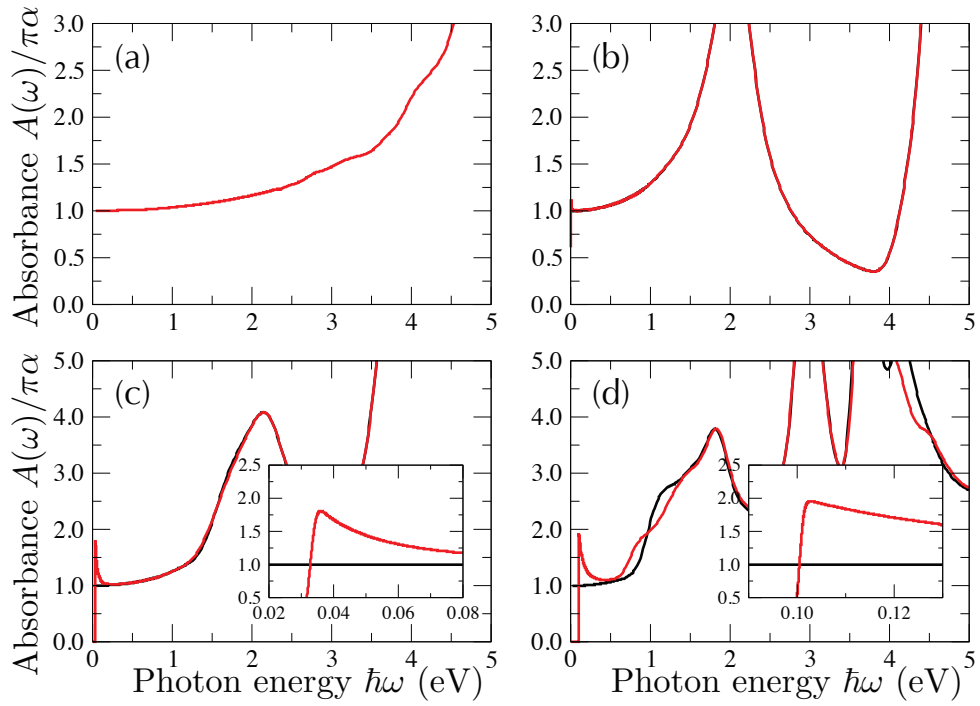
Figure 2.15: Optical absorbance in units of $\pi\alpha$ as a function of the photon energy for (a) graphene, (b) silicene, (c) germanene, and (d) stanene without (black solid lines) and with (red solid lines) spin-orbit coupling. The inset in (c) and (d) depicts the region around their respective fundamental absorption edges.
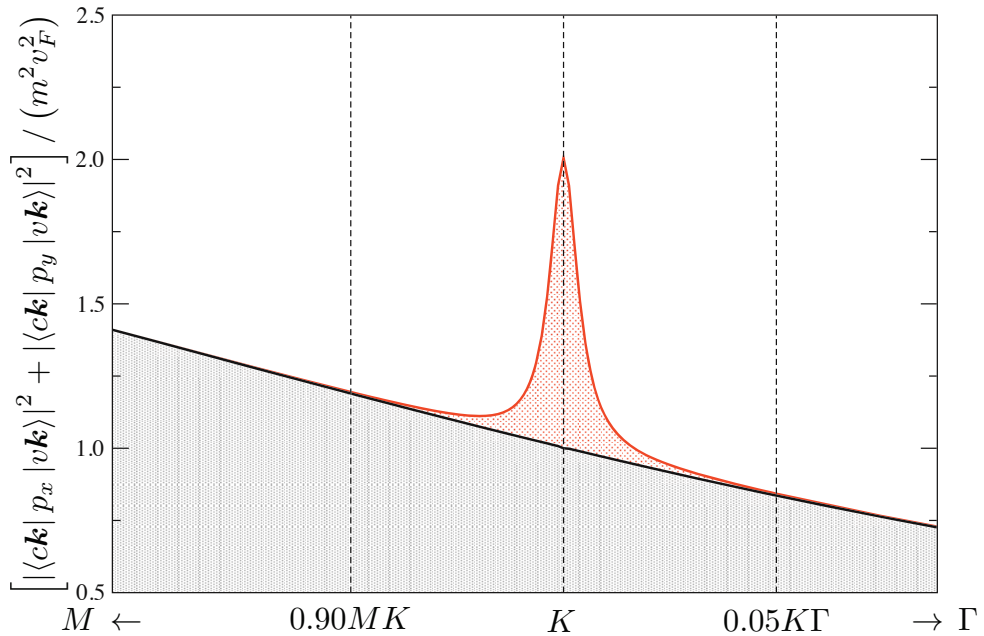
Figure 2.16: A normalized optical matrix element of germanene without (black solid line) and with (red solid line) spin-orbit interaction between the highest occupied and lowest unoccupied Bloch bands in the vicinity of K. At K, without SOC, the normalized optical matrix element approaches the ideal value 1.

resulting within the longitudinal approximation for Pauli spinors and germanene near a K or K' point are displayed in Fig. 2.16 for in-plane light polarization.

Without SOC , the squares of the momentum matrix elements $D(\boldsymbol{k}) = \sum_{j=x,y} |\langle c; \boldsymbol{k}|p_j|v; \boldsymbol{k}\rangle|^2$ reduce to $m^2 v_F^2$ at a Dirac point $\boldsymbol{k}_o \simeq K, K'$ with a weak, almost linear, $\Delta\boldsymbol{k}$ dependence, whereas the matrix elements $D(\boldsymbol{k})$ including SOC are significantly enhanced by a factor of two near $\boldsymbol{k}_o \simeq K, K'$ with a pronounced $\boldsymbol{k}$ dependence. Further away from the Dirac point the matrix elements with and without SOC are practically identical.

With SOC the matrix elements display an additional Lorentzian $\Delta\boldsymbol{k}$ dependence near a Dirac point. This can be represented analytically by

$$D(\boldsymbol{k}_o + \Delta\boldsymbol{k}) = m^2 v_F^2 \left(1 + \frac{1}{1 + b|\Delta\boldsymbol{k}|^2}\right) , \ b = \frac{2\hbar^2}{E_g m^*} = \left(\frac{2\hbar v_F}{E_g}\right)^2 . \tag{2.20}$$

The quantity b is determined by exhausting the oscillator strength sum rule on the dielectric function in the low-frequency regime. We have to stress that the agreement of Eq. (2.20) with the numerical curve in Fig. 2.16 is excellent. The same holds also for silicene and stanene (not shown). Including the corrected matrix elements (2.20) the optical absorbance is readily computed by means of Eq. (2.14). Taking into account the modified band dispersion (2.8) due to the massive Dirac particles in the presence of SOC we derive

$$A(\omega) = \pi\alpha \left[1 + \left(\frac{E_g}{\hbar\omega}\right)^2\right] \Theta(|\hbar\omega| - E_g) . \tag{2.21}$$

Since the joint density of states near the Dirac points $\sim \hbar\omega\Theta(\hbar\omega - E_g)$ is still linear in the photon energy, the strong modification of the absorbance is mainly a consequence of the modified transition matrix elements (2.20). The result recovers important features encountered in the numerical calculations. First of all, for photon energies that are large (but much below the optical interband transitions near critical points in the band structure in Fig. 2.15) compared to the electronic bandgap, the absorbance reduces to the well-known limit $A(\omega \gg E_g/\hbar) = \pi\alpha$ Furthermore, for photon energies in the vicinity of the fundamental absorption edge the absorbance increases to $A(\omega \approx E_g/\hbar) = 2\pi\alpha$. In between these two limits the absorbance follows the power law as predicted by Eq. (2.21). For vanishing SOC, i.e. $E_g \to 0$, the previous analytical description is recovered.

The above findings, in particular Eqs. (2.20) and (2.21) also hold for GGA calculations, if the proper bandgaps E_g and Fermi velocities v_F are taken from Table 2.1.

The optical absorbance is related to the real part of the 2D conductivity according to Eq. (2.11), which has been determined very precisely numerically with the HSE06 functional including SOC by means of a hybrid mesh strategy [cf. Fig. 2.15]. The imaginary part

is readily obtained by a numerical Kramers-Kronig transformation explained in detail in Sec. 1.4.1. The resulting real and imaginary part of the conductivity function $\sigma_{2D}(\omega)$ are shown in Fig. 2.17. Compared to the results obtained within the GGA-PBE approach
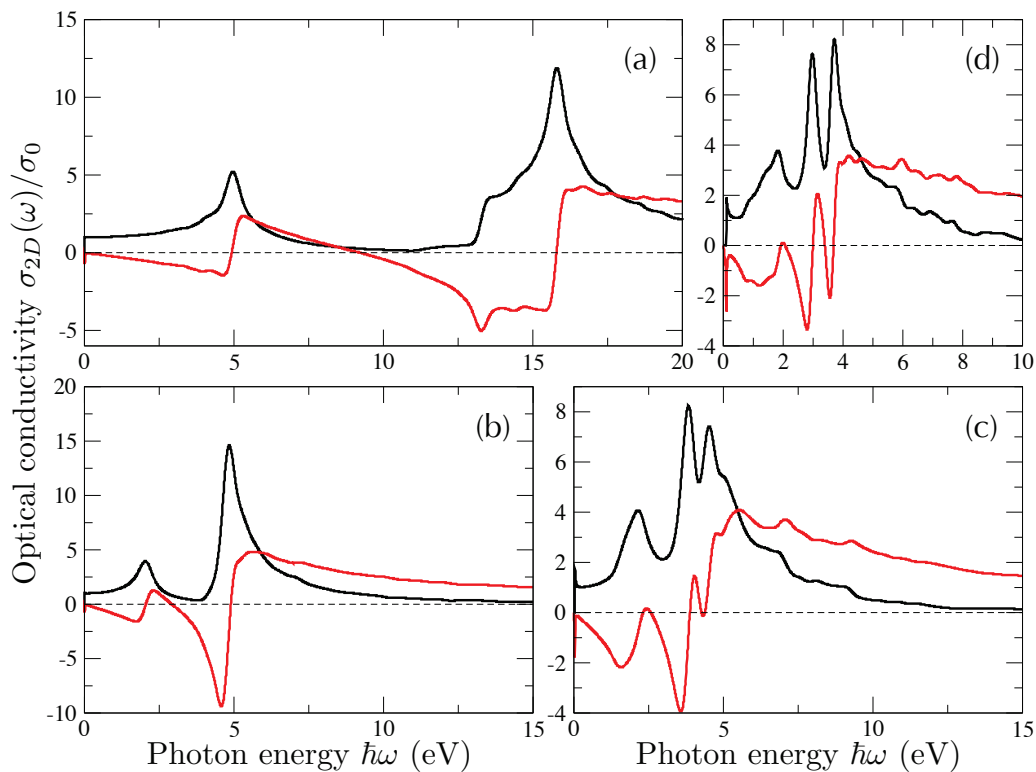
Figure 2.17: Optical conductivity in units of the *ac* conductivity $\sigma_0 = \pi\alpha = 0.023$ of (a) graphene, (b) silicene, (c) germanene, and (d) stanene. Real part: black line, imaginary part: red line.

(displayed in Figs. 2.13 and 2.13), the absorption peaks are blue shifted as expected. The blue shift of the first absorption peak amounts to 1 eV (graphene), 0.4 eV (silicene), 0.4 eV (germanene), and 0.3 eV (stanene). Apart from the blue shift further minor differences between the PBE and HSE06 appear in the heights and widths of the peaks. However, most of the differences are attributed to a larger broadening that has to be used to account for the smaller number of $\boldsymbol{k}$ points that were used for the HSE calculations.

2.6 Reflection, transmission and absorption

2.6.1 Influence of a conducting atomically thin layer

In the last section the absorbance $A(\omega)$ of 2D honeycomb crystals for normal incidence related to the real part of the 2D conductivity $\sigma_{2D}(\omega)$ by means of Eq. (2.11) has been investigated. However, a rigorous proof of the connection between optical absorption and the real part of the 2D conductivity is yet missing. In this section the reflection, transmission and absorption of 2D crystal sheets which are characterized by a 2D (complex) conductivity function $\sigma_{2D}(\omega)$ is investigated for arbitrary angles of incidence and light polarization. It is shown, how the special case of Eq. (2.11) is determined from the general formulas.

We study a single graphene, silicene, germanene, or stanene layer surrounded by two optical isotropic media $j = 0, 1$ which are characterized by complex dielectric functions $\epsilon_j(\omega)$ [cf. Fig. 2.18]. The sheet crystal itself is characterized by the frequency-dependent 2D
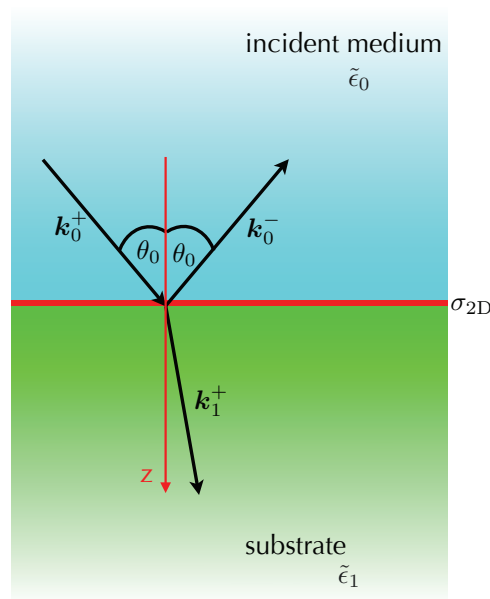
Figure 2.18: Light propagation in a system consisting of a 2D sheet characterized by the conductivity σ_{2D} and isotropic dielectrics $j = 0, 1$ with complex dielectric constants ϵ_j. The direction of the arrows illustrates incoming and outgoing light.

conductivity $\sigma_{2D}(\omega)$. Furthermore, we assume that the permeability of the incident medium and the substrate is equal to the vacuum permeability, embodying the assumption that the materials are nonmagnetic. We also require an incident medium without extinction, i.e., a dielectric function with zero imaginary part. This situation corresponds to a possible experimental situation, where such a group-IV sheet is deposited on top of a substrate. This sample is illuminated by light polarized parallel to the substrate surface from above, i.e., from the vacuum. For graphene such experimental arrangements [44, 138, 143, 144] have been used with exfoliated graphene sheets on top of an insulator or even air. Following the

idea of Berning [87] (cf. Sec. 1.6) the optical response of the layer in this special case is described by Eq. (1.62) and (1.63). For the reflection and transmission at arbitrary angles of incidence and light polarization with abbreviations introduced in Eqs. (1.58) and (1.59) it holds

$$
\begin{aligned}
R &= \left| \frac{\tilde{\eta}_0 - \tilde{\eta}_1 - \tilde{\sigma}_{2\mathrm{D}}}{\tilde{\eta}_0 + \tilde{\eta}_1 + \tilde{\sigma}_{2\mathrm{D}}} \right|^2 , \\
T &= \frac{Re(\tilde{\eta}_1)}{\tilde{\eta}_0} \left| \frac{2\tilde{\eta}_0}{\tilde{\eta}_0 + \tilde{\eta}_1 + \tilde{\sigma}_{2\mathrm{D}}} \right|^2 .
\end{aligned}
\tag{2.22}
$$

In the limit of non-conducting surfaces $\sigma_{2\mathrm{D}}(\omega) = 0$ from Eqs. (2.22) the known Fresnel relations [145] are obtained. If the dielectric functions of the incident medium and the substrate are known, only the conductivity function of the 2D sheet crystal as displayed in Fig. (2.17) is required.

2.6.2 Freestanding 2D sheets at normal incidence

The case of normal incidence is particularly interesting du to the experiments by Nair *et al.* [44] performed on graphene surrounded by air. Assuming $\tilde{\epsilon}_0 = \tilde{\epsilon}_1 = 1$ and $\theta_0 = 0$ the general expressions (2.22) further reduce to

$$
\begin{aligned}
R &= \left| \frac{\tilde{\sigma}_{2\mathrm{D}}/2}{1 + \tilde{\sigma}_{2\mathrm{D}}/2} \right|^2 \\
T &= \frac{1}{|1 + \tilde{\sigma}_{2\mathrm{D}}/2|^2} \\
A &= \frac{Re\,\tilde{\sigma}_{2\mathrm{D}}}{|1 + \tilde{\sigma}_{2\mathrm{D}}/2|^2} \; (= 1 - R - T) .
\end{aligned}
\tag{2.23}
$$

These expressions show how the frequency-dependent conductivity of the atomically thin sheet influences the optical properties. In general, real and imaginary part of $\tilde{\sigma}(\omega)$ can be considered as small quantities compared to 1 according to the numerical results. The leading terms of the expansion of A with respect to the real and imaginary part of $\tilde{\sigma}$ yields

$$
A \approx Re\,\tilde{\sigma}_{2\mathrm{D}} \cdot (1 - Re\,\tilde{\sigma}_{2\mathrm{D}} - \frac{1}{4}((Re\,\tilde{\sigma}_{2\mathrm{D}})^2 + (Im\,\tilde{\sigma}_{2\mathrm{D}})^2)) \approx Re\,\tilde{\sigma}_{2\mathrm{D}}
\tag{2.24}
$$

which has been used in Eq. (2.11).

According to the monoatomic character of the sheet crystal the transmission is only weakly influenced by an isolated layer. This can be easily underlined in the long-wavelength limit $\omega \to 0$. Neglecting SOC the optical conductivity according to Eqs. (2.11) and (2.19) is

given by $\tilde{\sigma}(0) = \pi\alpha$. It follows

$$R = \frac{(\pi\alpha/2)^2}{(1+\pi\alpha/2)^2} \approx \frac{\pi^2\alpha^2}{4}$$

$$T = \frac{1}{(1+\pi\alpha/2)^2} \approx 1 - \pi\alpha + \frac{3}{4}\pi^2\alpha^2 \qquad (2.25)$$

$$A = \frac{\pi\alpha}{(1+\pi\alpha/2)^2} \approx \pi\alpha - \pi^2\alpha^2 \,.$$

Indeed, neglecting second-order effects of the layer, i.e., the reflection, the zero-frequency absorbance is $A = \pi\alpha$.

The frequency dependence of the optical quantities R, T, and A of a freestanding group-IV honeycomb layer is displayed in Fig. 2.19. For the purpose of comparison $Re\,\tilde{\sigma}(\omega) =$
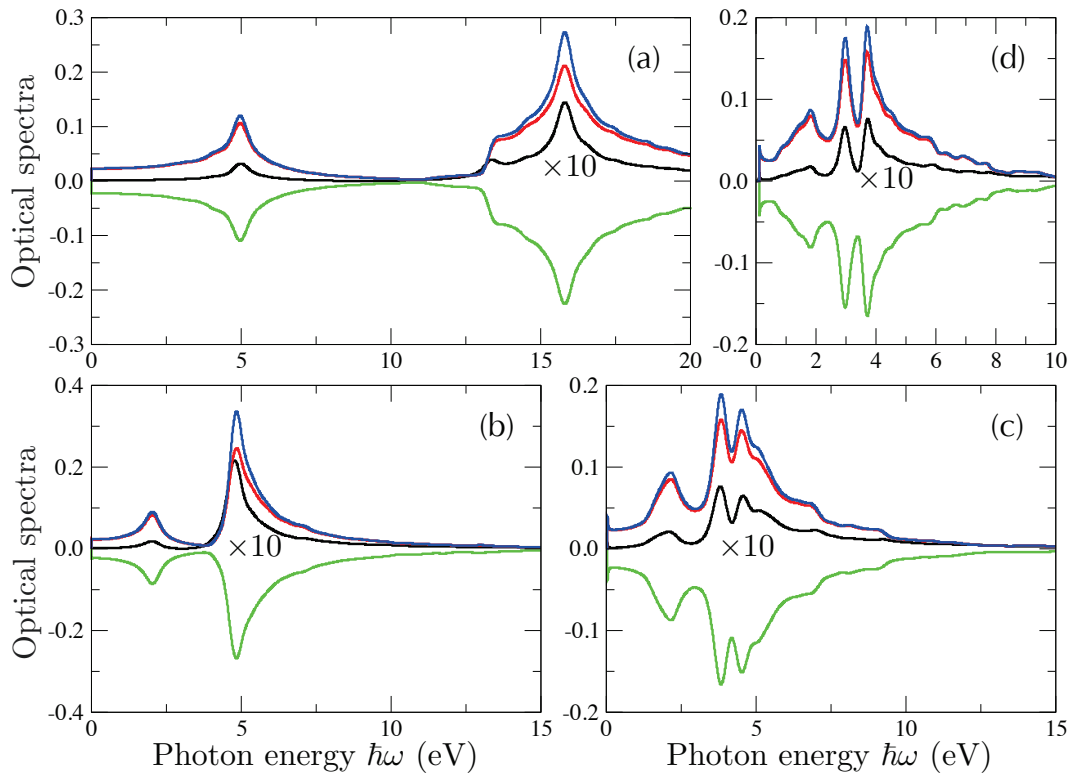
Figure 2.19: Frequency dependence of the optical properties R (black line), $T-1$ (green line), and A (red line) for the four honeycomb crystals (a) graphene, (b) silicene, (c) germanene, and (d) stanene. Normal incidence and hence in-plane light polarization are assumed. For the purpose of comparison with the absorbance $A(\omega)$ the real part of the normalized optical conductivity $\tilde{\sigma}(\omega)$ (blue line) is also displayed.

$\frac{4\pi}{c}Re\,\sigma_{2D}(\omega)$, the normalized real part of the optical conductivity, is also plotted in this figure. The optical properties exhibit several common features independent of the group-IV material. The reflectance of all layers is extremely small. It may only be measurable in the

frequency region of the resonances discussed in Fig. 2.17 for the real part of the normalized conductivity. As a consequence the absorbance and the real part of the normalized conductivity agree rather well. Deviations only appear for photon energies corresponding to the discussed resonances. The absorbance $A(\omega)$ and deviation $1 - T(\omega)$ from 100% transmittivity of a group-IV layer exhibit similar lineshapes and magnitudes. The strength of the absorbance is remarkable for one-atom-thick layers. This especially holds for the photon energies in the range of strong interband transitions. The absorbance approaches extremely large values up to 0.25 (graphene, silicene) or 0.15 (germanene, stanene) in these frequency regions. These values are much higher than the value $\pi\alpha = 0.023$ for vanishing frequencies. The major influence of the group-IV material concerns the lineshape, essentially the number and positions of the optical resonances. They however agree widely with the findings for $Re\,\sigma_{2D}(\omega)$ discussed in Fig. 2.17.

2.6.3 Optical properties beyond strictly 2D sheet crystals

The group-IV honeycomb crystals are usually treated as infinitely thin conducting layers within the framework of classical electrodynamics. Thus, the optical properties are exclusively determined by the isotropic optical conductivity $\sigma_{2D}(\omega)$ in the plane of the 2D sheet crystal, accounted for by means of the boundary conditions of electric (1.53) and magnetic fields (1.52). However, ab-initio calculations within the framework of the superlattice approach reveal also a non vanishing out-of-plane component of the dielectric tensor, which is impossible to include in the theory of a strictly infinitely thin layer.

In the ab-initio calculations the 2D sheet crystal is simulated within an arrangement of 3D unit cells with a large vacuum [cf. Eq. (2.1)]. We obtain the dielectric tensor of the system by means of Eq. (1.42). Due to the hexagonal symmetry of the system the dielectric tensor possesses only diagonal components and vanishing off-diagonal components, where we want to introduce the notation $\tilde{\epsilon}_\parallel \equiv \tilde{\epsilon}_{xx} = \tilde{\epsilon}_{yy}$ (isotropic in-plane component) and $\tilde{\epsilon}_\perp \equiv \tilde{\epsilon}_{zz}$ (out-of-plane component). Thus, 2D sheet crystals can be considered as a strongly anisotropic (uniaxial) crystal. Light propagating in an uniaxial crystal in general experiences birefringence, where the s- and p-polarized electromagnetic waves obey different dispersion relations:

$$\frac{(k_z^o)^2}{\tilde{\epsilon}_\parallel} + \frac{k_x^2 + k_y^2}{\tilde{\epsilon}_\parallel} = \frac{\omega^2}{c^2} \text{ (ordinary wave / } s\text{-pol.)} \tag{2.26}$$

$$\frac{(k_z^e)^2}{\tilde{\epsilon}_\parallel} + \frac{k_x^2 + k_y^2}{\tilde{\epsilon}_\perp} = \frac{\omega^2}{c^2} \text{ (extraordinary wave / } p\text{-pol.)}. \tag{2.27}$$

We introduced the index o (e) for the ordinary (extraordinary) wave, corresponding to s- (p-) polarized light. The theory of light propagating in multilayer thin films (Sec. 1.6) can be readily extended to anisotropic media. The anisotropy requires to replace Eqs. (1.56) and (1.59) by their anisotropic counterparts

$$\tilde{k}_{j,z} = \begin{cases} \tilde{k}_{j,z}^o = \sqrt{\tilde{\epsilon}_{j,\parallel} - \tilde{k}_{0,y}^2} & (s\text{-pol}) \\ \tilde{k}_{j,z}^e = \sqrt{\tilde{\epsilon}_{j,\parallel} - \frac{\tilde{\epsilon}_{j,\parallel}}{\tilde{\epsilon}_{j,\perp}} \tilde{k}_{0,y}^2} & (p\text{-pol}) \end{cases} \tag{2.28}$$

and

$$\tilde{\eta}_j = \begin{cases} \tilde{k}_{j,z}^o & (s\text{-pol}) \\ \tilde{\epsilon}_{j,\parallel}/\tilde{k}_{j,z}^e & (p\text{-pol}) \end{cases}. \tag{2.29}$$

The components of the dielectric tensor obtained by ab-initio methods are of course quantities related to the sheet crystal surrounded by vacuum. The question arises, how they can be related to the dielectric properties of the sheet crystal alone? Therefore we introduce an artificial thickness d of the 2D crystal. Consequently, the 3D superlattice arrangement with lattice constant L (according to Eq. (2.1)) can be considered as composed of a sheet layer of thickness d and a vacuum layer of thickness $L - d$. With the help of the transfer matrix approach or within a microscopic treatment [146] it can be shown, that the components of the dielectric tensor of the composite structure ($\tilde{\epsilon}_{\parallel}, \tilde{\epsilon}_{\perp}$) are related to the components of the sheet crystal ($\tilde{\epsilon}_{s,\parallel}, \tilde{\epsilon}_{s,\perp}$) and the vacuum ($\tilde{\epsilon}_{vac,\parallel}, \tilde{\epsilon}_{vac,\perp}$) by means of

$$L\, \tilde{\epsilon}_{\parallel} = d\, \tilde{\epsilon}_{s,\parallel} + (L - d)\, \tilde{\epsilon}_{vac,\parallel} \tag{2.30}$$

$$\frac{L}{\tilde{\epsilon}_{\perp}} = \frac{d}{\tilde{\epsilon}_{s,\perp}} + \frac{L - d}{\tilde{\epsilon}_{vac,\perp}}. \tag{2.31}$$

Since the dielectric tensor of the vacuum is known, the dielectric tensor $\tilde{\epsilon}_s$ of the 2D sheet crystal as a function of d and L and in relation to $\tilde{\epsilon}_{\parallel}$ and $\tilde{\epsilon}_{\perp}$ can be derived.

The optical properties of a sheet crystal with dielectric tensor components ($\tilde{\epsilon}_{s,\parallel}, \tilde{\epsilon}_{s,\perp}$) surrounded by two arbitrary bulk materials are determined by means of the transfer matrix, which is a product of one transfer matrix for each (nonconducting) interface and the propagation matrix within the sheet. It can be shown, that the transfer matrix T_j^s for s-polarization in the limit of $d \ll \lambda$ is given by

$$T_j^s = \frac{1}{2\tilde{\eta}_j} \begin{bmatrix} \tilde{\eta}_j + \tilde{\eta}_{j+1} + \tilde{\sigma}_{2D,j,\parallel} & \tilde{\eta}_j - \tilde{\eta}_{j+1} + \tilde{\sigma}_{2D,j,\parallel} \\ \tilde{\eta}_j + \tilde{\eta}_{j+1} - \tilde{\sigma}_{2D,j,\parallel} & \tilde{\eta}_j + \tilde{\eta}_{j+1} - \tilde{\sigma}_{2D,j,\parallel} \end{bmatrix}. \tag{2.32}$$

Here, the normalized dimensionless 2D in-plane conductivity $\tilde{\sigma}_{2D,j,\parallel} = -i\frac{\omega}{c}L(\epsilon_{j,\parallel} - 1)$ has been defined equivalently to the definition given in (1.58). For very large supercells

$(L \to \infty$ but still $L \ll \lambda)$ the quantity $\tilde{\sigma}_{2D,j,\parallel}$ converges and becomes independent of L due to the definition of the microscopic dielectric function calculated within the superlattice arrangement (1.42). Indeed, T_j^s corresponds to the transfer matrix derived within the approximation of an infinitely thin conducting interface (1.60).

However, the calculation of the transfer matrix T_j^p for p-polarized light is more complicated and yields

$$T_j^p = \frac{1}{2} \begin{bmatrix} (\tilde{\eta}_j + \tilde{\eta}_{j+1})\mathrm{ch} + (\tilde{\sigma}_{2D,j,\parallel} + \mathrm{ag})\mathrm{sh} & (\tilde{\eta}_j - \tilde{\eta}_{j+1})\mathrm{ch} + (\tilde{\sigma}_{2D,j,\parallel} - \mathrm{ag})\mathrm{sh} \\ (\tilde{\eta}_j - \tilde{\eta}_{j+1})\mathrm{ch} - (\tilde{\sigma}_{2D,j,\parallel} - \mathrm{ag})\mathrm{sh} & (\tilde{\eta}_j + \tilde{\eta}_{j+1})\mathrm{ch} - (\tilde{\sigma}_{2D,j,\parallel} + \mathrm{ag})\mathrm{sh} \end{bmatrix} \quad (2.33)$$

$$\mathrm{ch} = \cosh(\tilde{k}_{0,y}\sqrt{\tilde{\sigma}_{2D,j,\parallel}\,\tilde{\sigma}_{2D,j,\perp}}), \qquad \mathrm{sh} = \frac{\sinh(\tilde{k}_{0,y}\sqrt{\tilde{\sigma}_{2D,j,\parallel}\,\tilde{\sigma}_{2D,j,\perp}})}{\tilde{k}_{0,y}\sqrt{\tilde{\sigma}_{2D,j,\parallel}\,\tilde{\sigma}_{2D,j,\perp}}} \quad (2.34)$$

$$\mathrm{ag} = \tilde{k}_{0,y}^2 \tilde{\eta}_j \tilde{\eta}_{j+1}\tilde{\sigma}_{2D,j,\perp}, \quad (2.35)$$

where we introduced the normalized dimensionless 2D out-of-plane conductivity $\tilde{\sigma}_{2D,j,\perp} = -iL\frac{\omega}{c}(1 - \frac{1}{\epsilon_{j,\perp}})$. Although there exists a formal difference in the relations of the in-plane and out-of-plane conductivities to the components of the dielectric tensor of the superlattice it can easily be shown by means of Eq. (1.42) that in the limit $L \to \infty$ it holds $L(1 - \frac{1}{\epsilon_{j,\perp}}) \approx L(\epsilon_{j,\perp} - 1)$, thus, the definitions become equivalent. Consequently, neither the transfer matrix for s- nor p-polarization explicitly depend on the (artificial) thickness of the sheet crystal and the superlattice distance L in the numerical computations.

The transfer matrix T_j^p asks for further discussion in particular in regard to the s-polarized case T_j^s. For normal incidence ($\tilde{k}_{0,y} = 0$) both transfer matrixes are equivalent as expected. For oblique incidence ($\tilde{k}_{0,y} > 0$) there is an additional impact of the out-of-plane conductivity. Typically, in literature two approaches are discussed. The first approach assumes an infinitely thin sheet crystal and only in-plane components of the conductivity ($\tilde{\sigma}_{2D,j,\parallel} \neq 0$ and $\tilde{\sigma}_{2D,j,\perp} = 0$). In this case the transfer matrices for s- and p-polarization are formally identical. The anisotropy of the crystal does not enter the computation. However, the dependence on the polarization is still hidden in the definition of $\tilde{\eta}_j$ as common. This is also the approach that was chosen in this work. The second approach assumes a sheet crystal with finite width d of about 3.35 Å (corresponds to the sheet distance in graphite) [147], but an isotropic dielectric constant $\tilde{\epsilon}_{s,j}$. However, in this case the impact on the optical properties for oblique incidence is overestimated, as it will be shown below.

For the calculation of the conductivity tensor 128 bands have been used, which guarantees that all optical transitions up to $\hbar\omega = 40$ eV are taken into account. Here we are only interested in qualitative properties of the components of the conductivity tensor. Thus, a single $128 \times 128 \times 1$ $\boldsymbol{k}$-point mesh is sufficient to gather the main features of the

spectra. In Fig. 2.20 we show the normalized in- and out-of-plane conductivities for graphene obtained with the GGA-PBE functional over a wide frequency range. It is
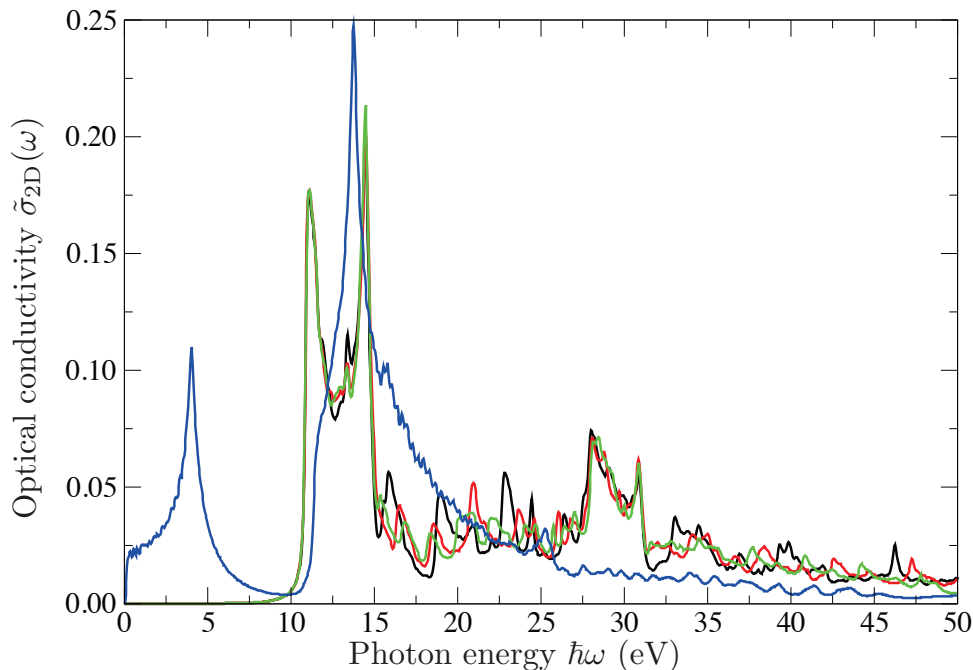
Figure 2.20: Frequency dependence of the real part out-of-plane component $\tilde{\sigma}_{2D,\perp}$ of the conductivity tensor of graphene for a vacuum thickness of $L = 20\,\text{Å}$ (black solid line), $L = 30\,\text{Å}$ (red solid line), and $L = 40\,\text{Å}$ (green solid line). For comparison, the blue solid line shows the real part of the in-plane component $\tilde{\sigma}_{2D,\parallel}$.

clearly visible that the out-of-plane component of the conductivity tensor converges with increasing size L of the vacuum layer. However, it also shows the strong anisotropy. For energies below $\hbar\omega = 10$ eV the real part of the out-of-plane component is extremely small compared to the in-plane component. Consequently, the transfer matrices T_j^p and T_j^s are equivalent in this frequency region. Thus, even for oblique incidence the approximation of an infinitely thin conducting sheet with vanishing $\tilde{\sigma}_{2D,j,\perp}$ almost perfectly holds. For very high photon energies $\hbar\omega \gtrsim 20$ eV the in- and out-of-plane components are of the same order of magnitude. In principle the out-of plane component should be present in the optical properties for oblique incidence of p-polarized light.

We argue, that the out-of-plane conductivity $\sigma_{2D,\perp}(\omega)$ and thus, the finite size of the 2D sheet crystal, can be safely neglected if the wavelength λ of the incident light is large compared to the thickness d, or if the angle of incidence is small. This is particularly true for all optical properties presented so far. For higher photon energies, however, $\sigma_{2D,\perp}(\omega)$ becomes more important and should essentially impact the optical properties of p-polarized light. However, in this case one may also argue that the wave vector $\boldsymbol{q}$ becomes also comparable to the length of the reciprocal lattice vectors and hence, it is

beyond the long-wavelength limit $\boldsymbol{q} \to 0$ used for the derivation of the optical matrix elements (1.36). There is also another argument. Above the ionization potential/electron affinity $I = A = 4.2$ eV of graphene [148, 149], in particular for UV light of photon energies $\hbar\omega \gtrsim 20$ eV, the real part of the optical conductivity is governed by the photoemission process. Hence, it makes less sense to speak about optical properties.

Chapter 3

Topological insulator character

3.1 2D group-IV honeycomb crystals

It has been stated in the previous sections that due to SOC the group-IV honeycomb crystals are insulators rather than zero-gap semiconductors. In this section the theory of topological insulators will be applied to the characterization of group-IV honeycomb crystals. One of the main necessary ingredients is a small-gap insulator, where the bandgap is governed mostly by SOC. The spin-orbit-induced bandgap at the Dirac points increases as the weight of the atom increases. Consequently, for the investigation of effects related to nontrivial topologies we will use germanene, which has a numerically advantageous bandgap compared to graphene and silicene. However, all results based on germanene are also applicable to the other group-IV honeycomb crystals aforementioned.

Freestanding germanene exhibits an inversion center in the origin of the unit cell if the atoms are arranged as in 2.1. Therefore, the parities of the bands at all four TRIM points are sufficient for the determination of the $\mathbb{Z}_2$ invariant ν_0. Numerically, the parities are obtained by means of Eq. (1.65). The wave functions obtained by *ab-initio* methods are composed of two parts, the plane-wave part in the region outside the atoms, and the augmentation part inside the atoms within the PAW methodology. However, the symmetry (in particular the parity) of the states is of course maintained in either of these parts, although the orthonormalization is slightly violated. For that reason we restrict ourselves to the plane-wave expansion of the (Pauli spinor) wave functions, whose expansion coefficients $C_{n,\boldsymbol{k},\boldsymbol{G}}^{\sigma}$ in

$$\langle \boldsymbol{r}|u_{n,\boldsymbol{k}}\rangle = u_{n,\boldsymbol{k}}(\boldsymbol{r}) = \frac{1}{\sqrt{\Omega}} \sum_{\boldsymbol{G}} \begin{pmatrix} C_{n,\boldsymbol{k},\boldsymbol{G}}^{\uparrow} \\ C_{n,\boldsymbol{k},\boldsymbol{G}}^{\downarrow} \end{pmatrix} e^{i\boldsymbol{G}\boldsymbol{r}} \qquad (3.1)$$

are easily accessible in VASP. The wave functions obtained in this way are also normalized to account for the neglected augmentation part. Germanene has eight valence electrons and thus, eight occupied bands. In Tab. 3.1 we show the parity eigenvalues at the Γ point and the three M points for the four Kramers degenerate bands. For symmetry reasons the parities for all bands at each distinct M point are equal. Consequently, the (strong)

$\mathbf{\Gamma}$	$+$	$-$	$+$	$+$	$(-)$
$3\mathbf{M}$	$-$	$+$	$-$	$+$	$(+)$

Table 3.1: Parities ξ_i of all four Kramers-degenerate occupied bands at $\mathbf{\Gamma}$ and the three M points (cf. Fig. 2.8(c)) . The last column denotes the product δ_i of all parities at the corresponding momentum.

topological index $\nu_0 = -1$ according to Eq. (1.66) is obtained. Therefore, the pristine 2D sheet crystal germanene as well as graphene, silicene, and stanene are two-dimensional topological insulators.

Although the parity method is sufficient due to the presence of an inversion center, only the method of the evolution of Wannier charge centers (WCC) as presented in Sec. 1.7.3 allows a generalization to systems without an inversion center. Such a system is presented later, hence, for comparison we already want to apply the method of WCCs on germanene. The evaluation of Eq. (1.70) requires N_x discrete points along the k_x direction. Convergence with respect to N_x has been checked carefully and it turned out that the computation of the topological invariant requires only a comparable low number. However, the details of the curves require a sufficiently large number of k_x points. The calculation of the phase of the WCC according to Eq. (1.73) as a function of k_y with $N_x = 100$ is shown in Fig. 3.1. The partner switching of the WCC occurs around $k_y = 1/3$ (which corresponds to $\boldsymbol{k} = 1/3\,\boldsymbol{b}_2$ according to Sec. 1.7.3). The result is not surprising, since the Dirac point K is located there and thus, valence and conduction bands are closest at this point. The resolution around that point has been increased in order to emphasize the partner switching in more detail. For k_y further away from the Dirac point the WCC are only slightly moving. An arbitrary reference line crosses the evolution lines an odd number of times indicating a topological insulator. A reduction of the number N_x to $N_x = 10$ lead to the same conclusion (topological insulator or not), however, for larger N_x the curves in Fig. 3.1 are smoother.

As expected, both the simple parity method and the more sophisticated and general WCC method successfully render pristine freestanding germanene as a 2D topological insulator. Although not presented here, also graphene, silicene and stanene possess the same classification. Graphene, however, is somewhat difficult. The spin-orbit induced bandgap is extremely small and thus, is metallic from the numerical point of view.
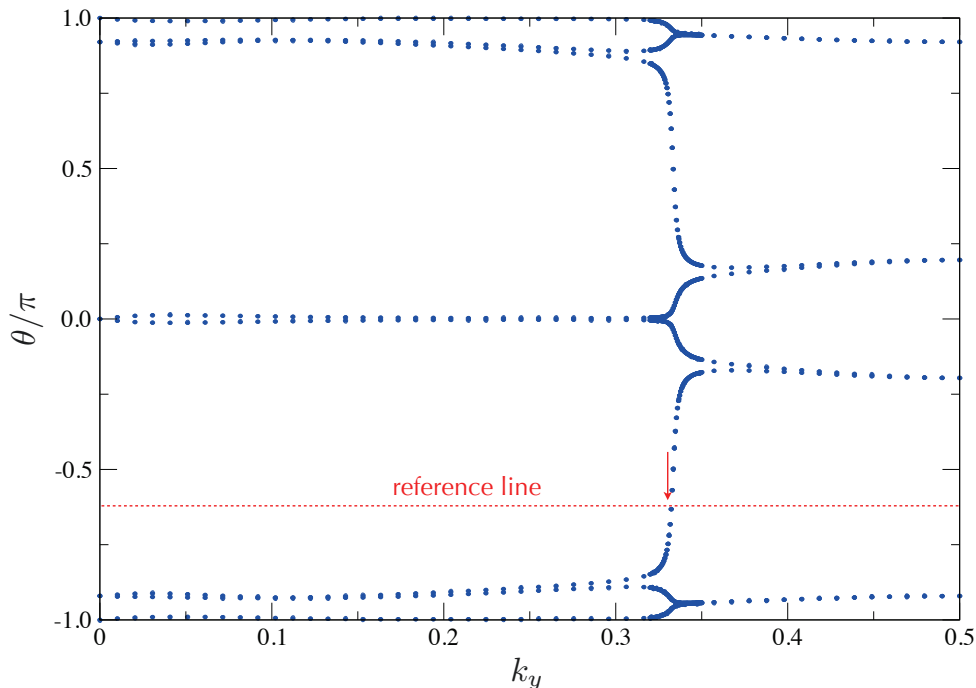
Figure 3.1: Evolution of Wannier charge centers (blue) constructed from the eight valence bands of germanene. The (arbitrary) reference line (red) crosses the evolution curves an odd number of times, indicating a topological insulator. The red arrow indicates the crossing point.

3.2 Impact of external electric fields on the topological invariant

3.2.1 Influence of transverse electric field

Here we investigate the impact of an external electric field E_z on germanene that is considered as a prototypical example. In the field-free case its nontrivial topological invariant has been verified already in the last section. The applied electric field has been varied up to $E_z = 10 \times 10^6$ V/cm. The electronic bandgap as a function of the applied electric field is displayed in Fig. 3.2. We observe the same trend as predicted analytically using a toy model based on only one orbital per atom and a simplified effective nearest-neighbor description of SOC [116, 117]. The bandgap closes at the critical field strength $E_c = 3.4 \times 10^6$ V/cm. Above E_c the bandgap opens again, which indicates a possible topological phase transition according to the general theory presented in 1.7.1. Extending Fig. 3.2 to negative E_z, the bandgap E_g shows a W shape as a function of the external electric field. The electronic bandgap as a function of the external electric field
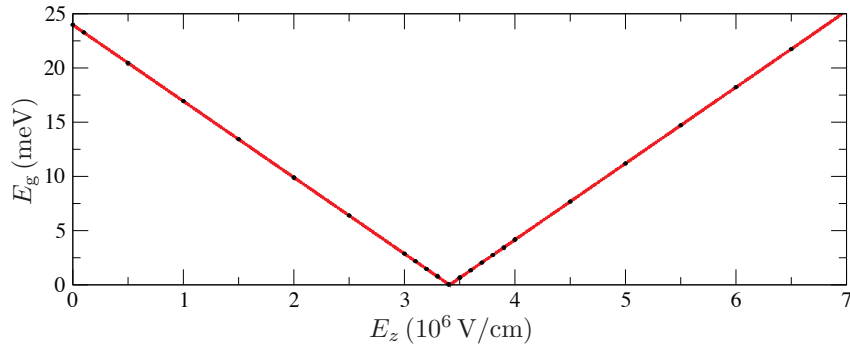
Figure 3.2: Electronic bandgap of germanene at the Dirac point as a function of the strength of an external homogenous electric field perpendicular to the 2D sheet crystal. The black dots represent numerical results, the red line is a (double linear) interpolation.

follows the general expression

$$E_{\mathrm{gap}}(E_z) = E_{\mathrm{gap}} \left| 1 - \frac{|E_z|}{E_c} \right| \tag{3.2}$$

For completeness the critical field strengths for silicene and stanene are also given in Table 3.2. It is clearly visible that E_c increases if the mass of the atoms is increased, since for heavier atoms the SOC-induced bandgap is larger (cf. Tab. 2.1). Anyway, the general equation (3.2) holds.

crystal	$E_c\,(10^6\,\mathrm{V/cm})$
silicene	0.26
germanene	3.41
stanene	9.3

Table 3.2: Critical field strengths E_c for the 2D group-IV honeycomb crystals silicene, germanene and stanene.

3.2.2 Topological invariant

We want to determine the topological index above the critical field strength E_c. Since the external electric field breaks the inversion symmetry of the system the parity method is not applicable anymore and hence, it is essential to use the phase evolution of the WCC. We restrict ourselves to field strengths E_z close to E_c. Independent of the strength of the electric field the phase evolution of the WCC further away from $k_y = 1/3$ (corresponds to the Dirac point located at $\boldsymbol{k} = 1/3\,\boldsymbol{b_2}$) is very similar and comparable to the evolution lines already presented in Fig. 3.1. The reason is that the valence and conduction bands

do not interact due to their large energetic distance. In the vicinity of the Dirac point the situation is, however, different. The valence and conduction bands become very close to each other allowing some interaction between them and also the WCC to switch partners. In Fig. 3.3 we therefore only show a small interval around the Dirac point in the direction ΓM in the 2D BZ which is sufficient to distinguish the trivial from the topological state regardless. The number of sampling points in k_y direction has been increased tremendously
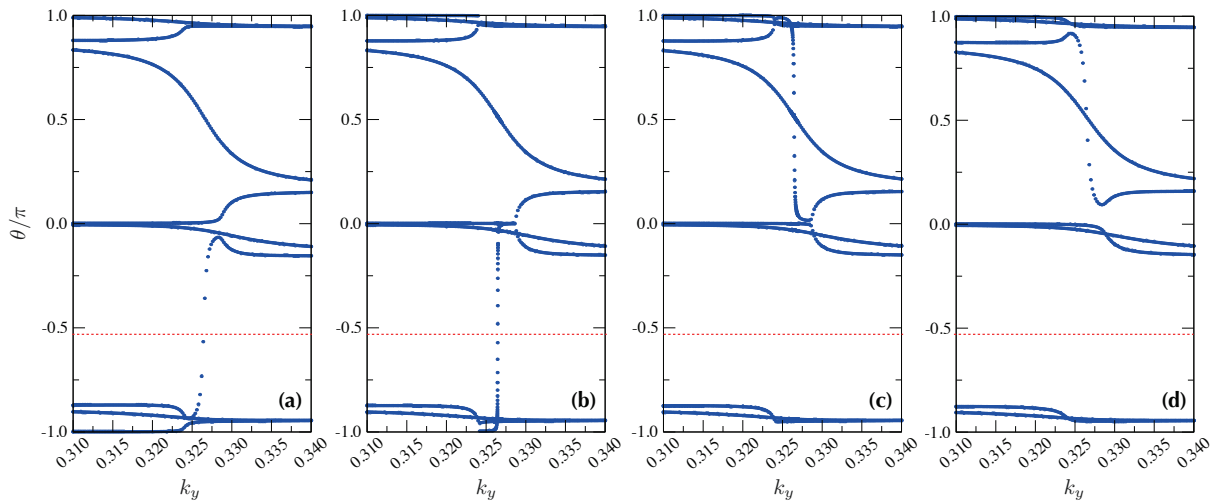
Figure 3.3: Phase evolution of the WCC (blue curves) constructed from the eight valence bands with increasing electric field strength $E_z =$ (a) 3.0, (b) 3.4, (c) 3.5 and (d) 4.0×10^6 V/cm. The reference line is plotted in red.

in order to clarify the exact phase evolution. In Figs. 3.3(a) and (b) the field strength is slightly below E_c. The reference line crosses the evolution lines an odd number of times, indicating a topological phase as in the case without electric field. The slope of one of the evolution lines becomes larger, the closer the electric field strength is to the critical value E_c. If the critical field strength is slightly passed, as displayed in Figs. 3.3(c) and (d), basically one evolution line in the interval $\theta < 0$ disappears and instead an evolution line appears in the interval $\theta > 0$. Counting the number of intersections with the reference line indeed identifies a trivial insulator phase for $E_z > E_c$, and thus, a topological phase transition at $E_z = E_c$.

The methods described above have been successfully applied by other groups to identify further systems as topological insulators, e.g., TiTe$_2$ under strain [150], silicene [151], HgSe [152], functionalized tin films [27], germanene [153], functionalized germanene [154] and dumbbell stanene [155].

3.3 Edge states in germanene nanoribbons

Formally, the 2D bulk insulators silicene, germanene and stanene are topological insulators and exhibit a topological phase transition into a trivial insulator in a strong transverse electric field above a critical field strength. In order to study explicitly the consequences for the possible helical edge states of the crystal as predicted for topological insulators, the crystals must be truncated to a finite size. Here we use germanene as a prototype for the group-IV honeycomb crystals.

3.3.1 Modeling of nanoribbons and their edges

The one-dimensional (1D) nanoribbons are simulated within a supercell approach with $L = 20$ Å ($L = 15$ Å) of vacuum in the direction perpendicular (parallel) to the crystal plane in order to avoid artificial interactions between the periodic images of the 1D structures. The edges of the ribbons are passivated by hydrogen atoms in order to exclude chemical edge states. Thus, Ge dangling bonds are removed as Ge-H bonding and anti-bonding states from the energy region around the Fermi level and the possible topological surface states are revealed. For silicene nanoribbons the deviation of the Si-Si bond lengths at the ribbon boundaries compared to the bulk values is very small [156]. For germanene the effect of structural modifications is also comparably small and has only a minor influence on the electronic properties. For that reason, since we are focused on the topological character of electronic properties, which should not depend on the details of the atomic structure of the edges, we disregard the small atomic relaxation of the edges and study the geometry of ideal, nonrelaxed germanene nanoribbons. We also confirmed the negligible influence of the relaxed edge geometry on the electronic properties by test calculations. More in detail, we fix the Ge atoms in the ribbon arrangement and relax only the position of the hydrogen atoms at the boundaries. This procedure allows to keep the high symmetry of the bulk locally. The neglect of such atomic modifications allows for a better comparison with the desired features of the edge states of the topological insulator as predicted by model studies [43, 117].

Nanoribbons made by 2D honeycomb crystals are characterized by two parameters, the edge orientation and the width of the ribbon. Typically, only two types of edges are studied, the zigzag edge (parallel to bonds, [11$\bar{2}$0] facet) and the armchair one (cutting parallel bonds in a hexagon, [1$\bar{1}$00] facet) [157, 158]. The smallest nanoribbon contains four germanium atoms and two (four) hydrogen atoms if terminated with zigzag (armchair) edges. Nanoribbons with higher index edges are in principle also possible, e.g. the facets

[$3\bar{2}\bar{1}0$] and [$5\bar{4}\bar{1}0$], whose smallest ribbon already contains 28 germanium atoms, but they are less likely present in experiments due to the low symmetry and, therefore, not considered here. The aforementioned low-index crystal orientations are displayed in Fig. 3.4. Another common termination of nanoribbons is of the bearded edge type [159–161], which is very similar to armchair edges. However, they are less common and, thus, also not considered here.
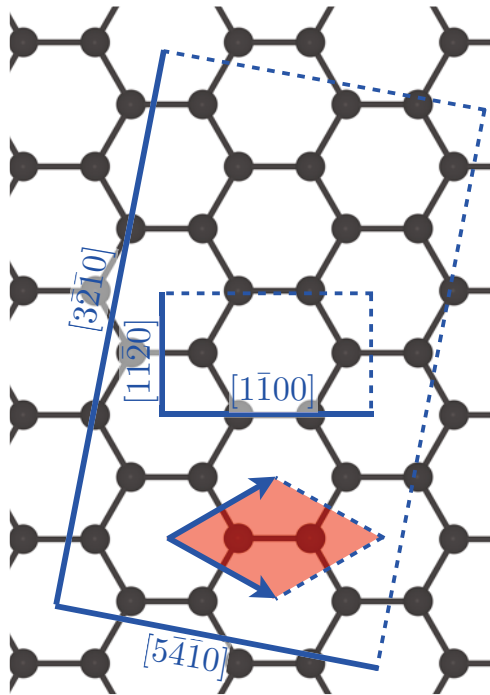
Figure 3.4: Possible low-index crystal orientations for finite nanoribbons. The primitive unit cell of the hexagonal 2D crystal (shaded in red) and the unit cells of the corresponding nanoribbons are indicated.
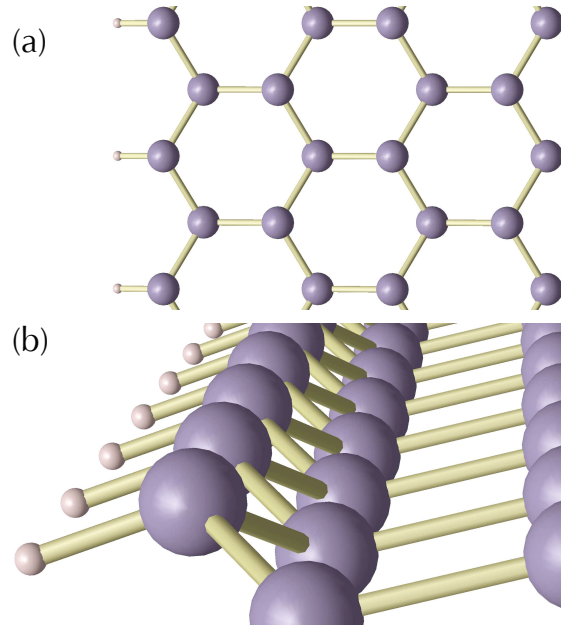
3.3.2 Zigzag germanene nanoribbons

The lattice vectors of the smallest irreducible slab cell of germanene for the description of either zigzag or armchair ribbons is related to the lattice vectors of the unit cell (2.1) by

$$\begin{aligned}
\boldsymbol{a}_1^{\text{rec}} &= \boldsymbol{a}_1 + \boldsymbol{a}_2 \\
\boldsymbol{a}_2^{\text{rec}} &= -\boldsymbol{a}_1 + \boldsymbol{a}_2 \,.
\end{aligned} \tag{3.3}$$

The corresponding primitive cell is rectangular and contains four Ge atoms. The nanoribbon with zigzag edges is obtained by repeating the primitive cell several times in $\boldsymbol{a}_1^{\text{rec}}$ direction, add a vacuum of 15 Å in the same direction while cutting the respective bonds, and add hydrogen atoms for passivation. The width W of the nanoribbon is best represented by the number N of hexagonal group-IV atom rings in the direction of the lattice vector $\boldsymbol{a}_1^{\text{rec}}$ of the 2D Bravais lattice of the honeycomb structure [43] . A total of $2(N+1)$ group-IV atoms belongs to the atomic basis in the rectangular unit cell of the nanoribbon

arrangement. We restrict ourselves to a ribbon width of $N = 16$, which is large enough to exclude any interactions between the two sides of the ribbon. The overlap of the edge states decaying from both sides of the ribbon is therefore negligible. The resulting atomic geometry of the edges is displayed in Fig. 3.5. The bond length between Ge and H is 1.58 Å. The bond angle against the 2D crystal plane is 22.5°.

(a)

(b)

Figure 3.5: (a) Top and (b) perspective view on the atomic structure of the hydrogen-passivated edge of a zigzag germanene nanoribbon.
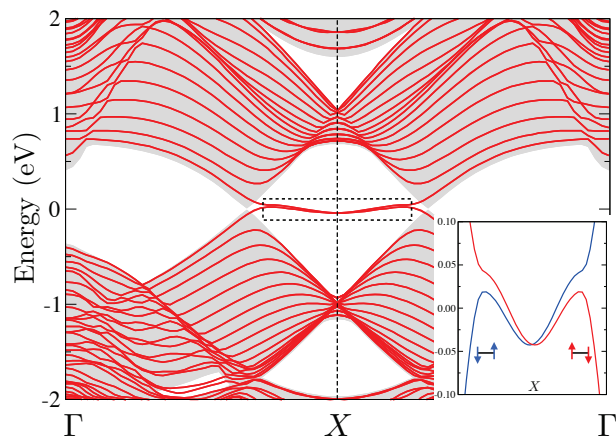
Figure 3.6: Band structure of nonmagnetic $N = 16$ zigzag germanene nanoribbon (red curves) and the projected bulk band structure (gray shading) in the background. Inset: Spin polarization of particles in spin-degenerate topological states close to the Fermi level and their corresponding spin orientation (in red and blue) near the edges of the nanoribbon.

In Fig. 3.6 we display the calculated band structure of the nonmagnetic nanoribbon and the projected bulk band structure, which makes it easy to distinguish between bulk and edge states in the 1D BZ. Although SOC is included, the spin polarization and hence edge magnetism is not yet taken into account. Two Dirac points of the hexagonal bulk BZ are folded onto $\pm 2/3\,\Gamma X$ of the 1D BZ of the nanoribbon. The bandgap of the nanoribbon at the Dirac points is slightly larger than in the bulk due to finite-size effects despite the large ribbon width $N = 16$. However, one clearly sees the appearance of edge states in the

pockets of the projected bulk band structure at the X point of the 1D BZ. In the case without any edge magnetization each edge state is twofold degenerate due to the existence of two equivalent ribbon edges. The upper and the lower bands cross each other exactly at the X point.

Detailed analysis of the bands reveals the spin texture of the bands, which is determined as the expectation value of the three Pauli matrices in the vicinity of the X point in the 1D BZ. They are distinguished by red and blue in the inset. Blue bands refer to spin-up states, which are localized preferably on one edge and where the spin points in a direction perpendicular to the plane of the nanoribbon, and spin-down states, localized on the opposite edge. The real-space localization of the spin-up states in red bands is opposite to that of blue bands such that the ribbon remains nonmagnetic. These bands also appear in Kramers pairs, which means they are symmetric with respect to each other around the X point. The edge character of the states with energies near the Fermi energy at X is illustrated in Fig. 3.7.


Figure 3.7: Wave-function square of the edge states with vanishing energy at X. Ge and H atoms are shown as small purple and white spheres. The center of the ribbon is omitted.

Relatively flat gapless bands appear in the fundamental gap region around a boundary of the 1D BZ. However, in contrast to the tight-binding predictions [117], their dispersion is strongly nonlinear and hence totally different from the predicted linear dispersion. The reason is that the tight-binding model is lacking several aspects of the real ribbon system not included in such a toy model. First, the tight-binding model incorporates only one atomic orbital per atom for the description of the system, which leads to missing bands of the p_x- and p_y-folded bulk states at the Γ point. Furthermore, the buckling and, consequently, also the mixing of different orbitals are not considered. It is clearly shown that, in contrast to the tight-binding predictions, the dispersion of the edge-state bands is rather parabolic (at least that of the upper one) or shows a Mexican-hat behavior (the lower one), rather than a linear dispersion. Very close to X (0.15 $X\Gamma$) these bands can be interpreted as two occupied parabolas which are slightly displaced against each other. The spin polarization of the bands near X or $-X$ seems to be however independent of the electronic structure description.

In our non-collinear simulation of the spin polarization the complete, self-consistently arranged coupling between orbital and spin motion of the electrons is considered. In contrast, in the tight-binding model the Rashba contribution to SOC is either neglected [43] or taken into account with a coupling constant that is too small [117] due to the nearest-neighbor SOC, which may be interpreted as the action of an effective magnetic field due to the orbital motion in normal direction. The Rashba splitting of the spin-decomposed states leads to the typical Mexican-hat-like crossing of the bands as shown in Fig. 3.6. We point out that very recently a similar band behavior has been observed by means of a similar electronic structure approach for germanene nanoroads [153].

We believe that the disagreement is mostly due to the rather small SOC in the real system compared to the oversimplified tight-binding Hamiltonian. In order to support our idea we have plotted the $N = 16$ nanoribbon bands again in Fig. 3.8, but with increasing strength of the SOC, by varying the prefactor β_{SOC} of the corresponding term in the Kohn-Sham equations within the DFT-GGA approach with SOC up to one order of magnitude. Indeed, with increasing SOC strength β_{SOC} the uppermost edge-state
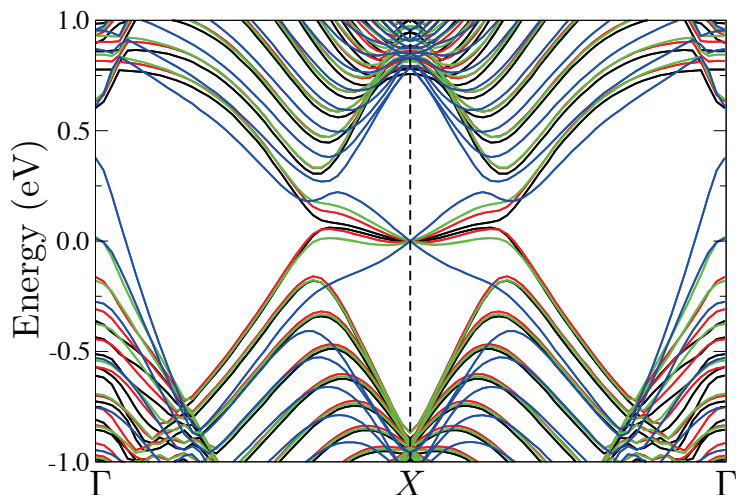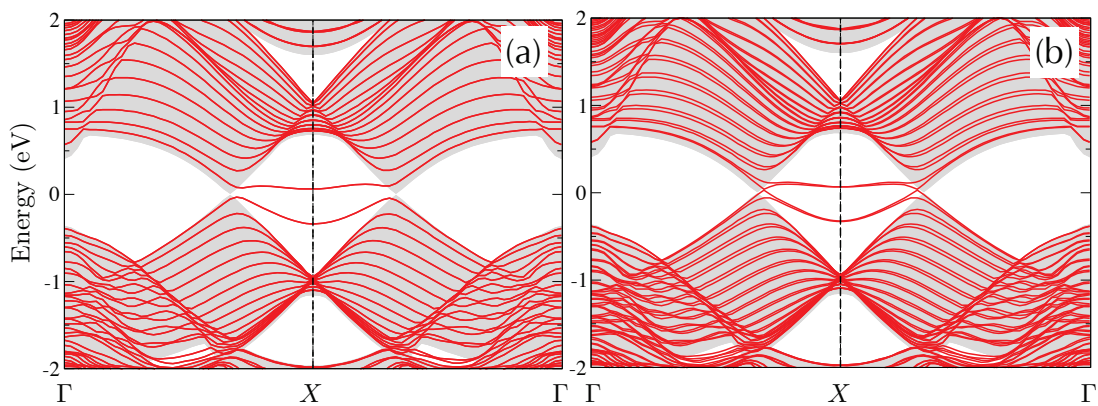

Figure 3.8: Band structure of a nonmagnetic $N = 16$ zigzag germanene nanoribbon with varying SOC enhanced by a factor $\beta_{\mathrm{SOC}} = 1$ (black curves), 3 (red curves), 5 (green curves) or 10 (blue curves).

band becomes more linear, while the lower one loses the relative influence of the Rashba effect. The turning point is SOC that is about five times stronger, i.e., $\beta_{\mathrm{SOC}} = 5$, which approaches values relevant for stanene. Indeed, recent theoretical investigations about stanene and fluorinated stanene [27] also showed promising results of helical edge states in the corresponding nanoribbons. For a factor of 10, i.e., completely unrealistic SOC values, the linear bands predicted by toy models appear. On the other hand, the σ-derived gap at the Γ point is closed, so that the system becomes metallic due to non-topological (i.e. trivial) states.

3.3.3 Edge magnetism

We also take into account the possibility of magnetic edges of which we consider ferro- and antiferromagnetic configurations. It is well known that taking into account magnetic edges may further reduce the energy of the system toward the correct ground state of graphene and silicene nanoribbons [162,163]. The ground states are predicted to be antiferromagnetic at half-filling. For graphene, in addition to total-energy optimization by means of DFT, such zigzag edge magnetization has been confirmed experimentally by means of transport measurements [164]. In fact, in our calculations antiferromagnetic ordering of the spins is energetically favored over the nonmagnetic and ferromagnetic state. In Fig. 3.9 it is clearly

Figure 3.9: Band structure of the (a) antiferromagnetic and (b) ferromagnetic $N = 16$ zigzag germanene nanoribbon (red urves) and the projected bulk band structure (gray shading) in the background.

shown that edge magnetization strongly modifies the dispersion of the edge states at the boundary of the BZ. The spin magnetic moment is about $0.15\mu_B$ per surface atom. For
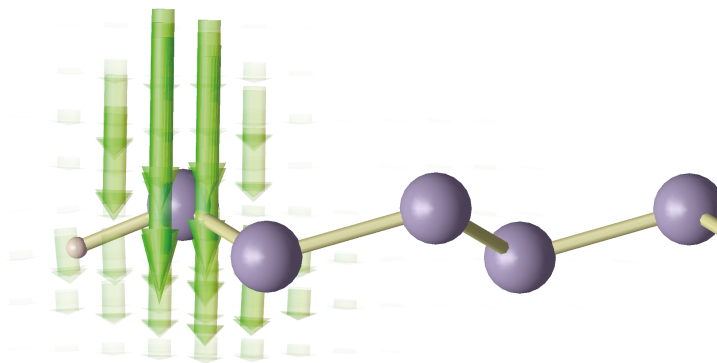
Figure 3.10: Real-space localization of the spin density of the antiferromagnetic germanene nanoribbon at one of the edges.

the antiferromagnetic ground states the spin moments at each edge atom are oriented in opposite directions depending on the edge. In Fig. 3.10 the real-space spin orientation for

an edge state is shown in the vicinity of one edge. It supports the simplified illustration used in Figs. 3.6 and 3.11. Thereby, the total energies of the (anti-)ferromagnetic ribbons depend only slightly on the exact orientation of the spin relative to the plane of the ribbon. The most intriguing result of the energetically favored antiferromagnetic ordering in Fig. 3.9(a) is the opening of a bandgap between them, turning the nanoribbon system into a trivial insulator. The electrons of these states are still localized at the surface of the ribbon but do not lead to metallic surface states. In this case, the system can, in general, not be regarded as a TI. The opening of a bandgap between the surface states already emerges if only spin polarization, and not SOC, is taken into account as it has been demonstrated in previous works on group-IV nanoribbons [165].

We also found a metastable ferromagnetic configuration with spin magnetic moments localized mainly at the edges of the ribbon, which is energetically slightly less favored than the antiferromagnetic one. The energy gain of the antiferromagnetic ground state is about 1 meV (13 meV) per surface atom compared to the ferromagnetic (nonmagnetic) ground state. The small energy difference might give rise to an antiferromagnetic-ferromagnetic transition for larger ribbon widths as predicted for silicene nanoribbons [166]. Because of the magnetic field in the normal direction the degeneracy of all band states shown in Fig. 3.9(a) is lifted in Fig. 3.9(b). The energy regions of the Dirac cones appearing in infinite germanene honeycomb crystals become very interesting. Gapless edge states appear in the "fundamental gap" of the nanoribbon. Linear bands of different spins cross each other near the position of the "bulk" K of K' states. However, they are slightly displaced in $\boldsymbol{k}$ space along the ΓX high-symmetry line toward the X point. We have to mention that defects of the edges may significantly modify the magnetic properties. This also has been shown very recently for silicene nanoribbons [166].

3.3.4 Transverse electric field

Not only magnetic fields but also electric fields influence the edge states and their topological character. Electrically tunable bandgaps have been predicted by calculations for external electric fields oriented parallel to the buckled monolayer of Si or Ge atoms, a silicene or germanene sheet [162, 167]. The impact of such in-plane electric fields on the edge states is much stronger since they break the symmetry of the system. The degeneracy due to the two equivalent edges is lifted. Additional splittings appear. Recently, it has even been shown that field-gated silicene possesses two gapped Dirac cones exhibiting 100% spin polarization and, hence, is a promising source for spin-polarized electrons [168].

In order to study the influence on the topological character, we focus on electric fields,

which leave the ribbon edges equivalent. Consequently, we do not consider the effect of in-plane electric fields. Here, we investigate the influence of vertical homogeneous electric fields E_z. We have to stress that for $E_z = 0$ the antiferromagnetic ribbon is the electronic ground state, however, in this section we focus only on the impact of an external electric field on the nonmagnetic ribbon for reasons that are explained below. Therefore, we study the electronic band structure of germanene and the nonmagnetic $W = 16$ nanoribbon under the action of transverse homogeneous electric fields of various strengths perpendicular to the sheet plane as in Sec. 3.2.2.

The situation in germanene $N = 16$ nanoribbons is different from the behavior of the infinite germanene crystal. Only the nonmagnetic ribbon possesses metallic edge states, whereas a bandgap is present in the antiferromagnetic ground state. In order to study a possible phase transition into a trivial insulator we therefore omit the edge magnetism. Most interesting is the field influence on the electronic structure due to the edge states around the Fermi level and the X point at the BZ boundary as indicated by the electronic structure displayed in Fig. 3.6. We only investigate an energy interval of the order of a few tenths of milli-electron volts and wave vectors around X about ± 0.2 of the entire ΓX distance. Field strengths similar to those in Fig. 3.2 are applied. The development of the bands near X in Fig. 3.11 with increasing field strength E_z is totally different to the "bulk" W-shape in Fig. 3.2. Our results considerably differ from the predictions obtained using a simple four-band second-nearest neighbor tight-binding Hamiltonian [117]. A proof of the reasons has been already discussed in Fig. 3.6. The dispersion of the gapless edge state bands is significantly deformed compared to the tight-binding predictions. Instead of two linear bands, which cross the Fermi level at X, the *ab-initio* calculated bands exhibit a dispersion well known for the Rashba effect in two dimensions [130]. This is again displayed in Fig. 3.11(a), which also clearly shows the metallic character of the ribbons instead of a zero-gap semiconductor behavior [117]. Figures 3.11(b), 3.11(c), and 3.11(d) show the main consequences of a vertical electric field, the symmetry lowering, and the accompanying splitting E_{split} of the edge-state-derived energy bands at X and its surroundings. The dependence of the splitting on the field strengths at or around the critical one E_c are studied. For finite field strength the spin polarization of each edge state is conserved but each band is now only built by states localized at one edge with a defined spin orientation. The inversion symmetry is destroyed [168]. The corresponding degeneracy is lifted. Instead parabolas of different spin polarizations appear, which are, however, energetically separated slightly and shifted against each other around X by Δk_{Rashba}. The field free value $\Delta k_{\text{Rashba}} = 0.02$ Å^{-1} practically does not vary for increasing field strength. At X this energy splitting $E_{\text{split}} = \Xi E_z$ increases almost perfectly linearly with the external electric field E_z. Its coefficient amounts to $\Xi = 0.765$ eÅ. The band
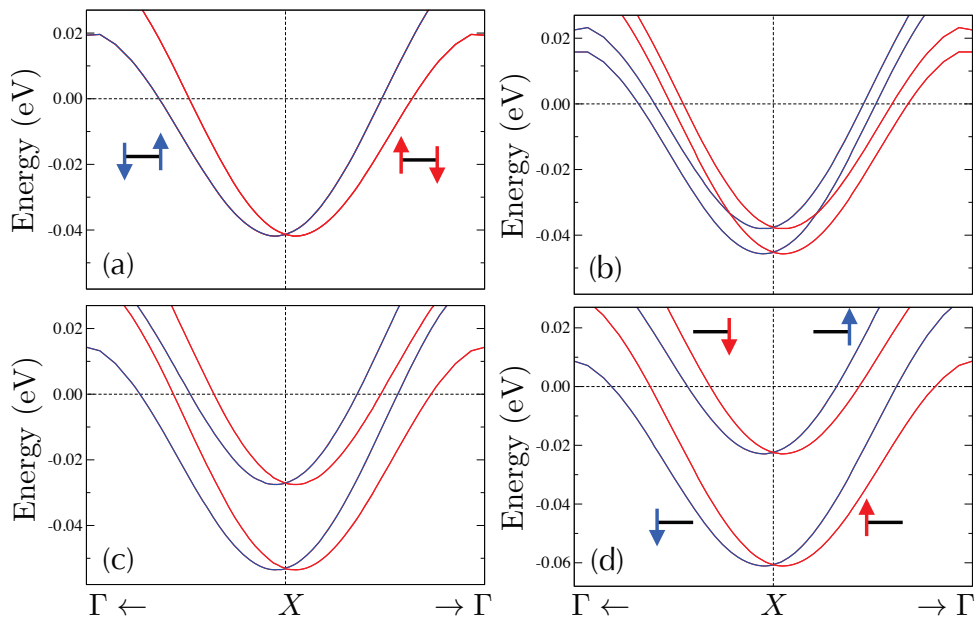
Figure 3.11: One-dimensional energy bands mainly derived from edge states for germanene nanoribbons with $N = 16$ near the boundary of the 1D BZ. Only states around the Fermi level, used as energy zero, and the X point of the BZ boundary are plotted. The two colors (red and blue) of the bands indicate different spin orientations. The field strength varies: (a) $E_z = 0$, (b) $E_z = 1 \times 10^6$ V/cm, (c) $E_z = E_c = 3.4 \times 10^6$ V/cm, and (d) $E_z = 5 \times 10^6$ V/cm (d). The spatial localization of the wave functions at the edges and their spin orientation are illustrated by arrows.

splitting E_{split} at X can be interpreted in first-order perturbation theory by a shift

$$\langle \psi_{L/R} \sigma | e E_z z | \psi_{L/R} \sigma \rangle$$

of each edge state $|\psi_{L/R}\sigma\rangle$ with spin orientation $\sigma = \uparrow, \downarrow$ localized at the left/right edge. Thereby $e E_z z$ describes the coupling of the electrons to the electric field. Due to the presence of the transverse field the symmetry equivalence of the two ribbon edges is destroyed. Consequently from left to right changes the sign of the shift because of the spinor character of the states, while its magnitude is conserved. Twice the absolute value of such a shift defines the splitting energy. We also investigated the impact of a transverse electric field on the electronic structure of the antiferromagnetic ground state. Even strong electric fields only slightly lift the degeneracy of the occupied and unoccupied surface bands (not shown). The general influence of the electric field remains small.

The field influence on the electronic structure presented in Fig. 3.11 is totally different from the predictions of toy models of the kind used in Ref. [117]. Apart from the fact that all bands are taken into account, the properties of a real electron system are described. They contain the atomic edge geometry and, in particular, the self-consistency of the

inhomogeneous electron gas with non-collinear spins. They drastically change the response to the field compared to a system with fixed band and SOC parameters as used in the empirical tight-binding method. Consequently the electron redistribution due to the external electric field is screened and hence weakened [17]. Furthermore, the orbital motion of the electrons is modified via the coupling of angular momentum and spin in the SOC operator. In any case the topological transition between a TI and a band insulator predicted by toy models does not occur. Rather, independent of the field strength the edge states form a metallic system with a Fermi surface around an X point. The band splitting due to the field however makes this Fermi surface more complex. For unrealistically high fields above $E_z = 0.2$ V/Å$= 2 \times 10^7$ V/cm (not shown in Fig. 3.11) a gap opening becomes visible. However, even for stanene with a much stronger SOC the field strength has to be unrealistic strong to approach a band insulator. In a more realistic system the topological character of the electronic structure related to the edge states is difficult to destroy.
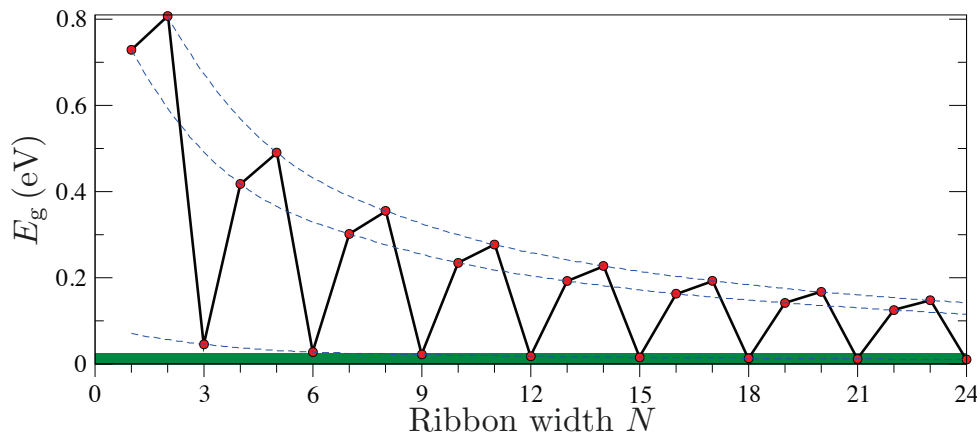
3.3.5 Armchair germanene nanoribbons

The armchair termination of the germanene nanoribbon is obtained by repeating the primitive cell defined in Eq. (3.3) in $\boldsymbol{a}_2^{\text{rec}}$ direction (cf. Fig. 3.4), add a vacuum of 15 Å in the same direction while cutting the respective bonds. A total of $2(N + 2)$ Ge atoms belong to the atomic basis of the nanoribbon cell. Two additional hydrogen atoms per edge are needed for full passivation of the dangling bonds. As in the case of zigzag germanene nanoribbons only the hydrogen atoms are optimized with respect to their bond angles and lengths. Although the bond length between Ge and H atoms remains the same as at the zigzag edges, the bond angle against the sheet plane slightly decreases to 17.4°.

The band structure for the $N = 16$ armchair nanoribbon as well as the projected bulk band structure is plotted in Fig. 3.12. In contrast to the zigzag-terminated edges the two Dirac cones of germanene bulk are folded onto the Γ point of the 1D BZ of the nanoribbon. The bandgap of the nanoribbon indicates a 1D insulator rather than a metal. The bandgap of the $N = 16$ nanoribbon is larger than the bulk bandgap due to finite-size effects. Furthermore, the bandgap is expected to vary as a function of the ribbon width N as depicted in Fig. 3.13. From the numerical calculations we may conclude, that the nanoribbon can be divided into three distinct classes with ribbon widths $N = \{3M + 1, 3M + 2, 3M + 3\}$ $(M = 0, 1, 2, \ldots)$ [165]. Within each class the bandgap decreases monotonically with increasing ribbon width. More importantly, for fixed M the bandgaps of class $N = 3M + 3$ are substantial smaller compared to the other two classes. The bandgap is even smaller than the bulk bandgap if $N \geq 9$ $(M \geq 2)$, indicating the appearance of edge states within the fundamental bulk bandgap. The same trend has also
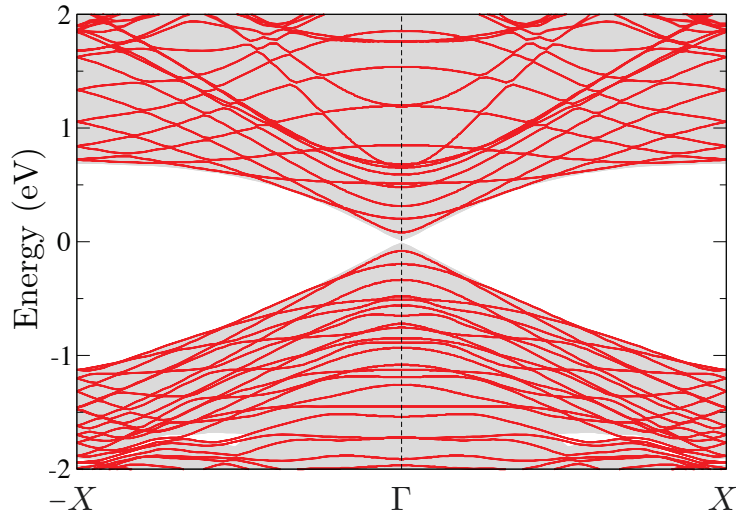
Figure 3.12: Band structure of the $N = 16$ armchair germanene nanoribbon (red curves) and the projected bulk band structure (gray shading) in the background.

Figure 3.13: Electronic bandgap of armchair germanene nanoribbons as a function of the ribbon width N. Numerical results are shown as red filled dots. Blue lines correspond to interpolated values for the three distinct classes described in the text and are used as a guide to the eye. The energy range that is smaller than the bulk bandgap is also shown (green shaded area).

been observed in earlier works for graphene [158, 162] and silicene nanoribbons [156]. For ribbon widths up to $N = 24$ the bandgap of the nanoribbon remains finite, in contrast to the expected zero-gap helical edge states proposed by the theory of topological insulators. We could not further increase the size of the nanoribbon for numerical reasons.

The edge states of armchair germanene nanoribbons appear at the center of the 1D BZ where also the bandgap of the folded bulk band structure is present. Therefore, edge states and bulk states are interfering leading to a an increase of the delocalization of the edge states into the bulk and thus, a coupling between both edges of the ribbon even if the ribbon is comparably large. However, in the limit of very large nanoribbons the

exact termination on either side of the ribbon and thus, the belonging to one of the three ribbon classes, should not matter. Consequently, in this limit the electronic bandgap of all classes should converge to zero, indicating indeed the presence of gapless edge states. We conclude, that the germanene armchair ribbons up to $N = 24$ are not yet large enough to fully decouple the edge states on both edges of the ribbon. Increasing the SOC by a prefactor $\beta_{\text{SOC}} > 1$ (not shown) increases the bulk bandgap of germanene, which also leads to the decoupling between bulk and surface bands at Γ of the 1D BZ, however, for unrealistic high values β_{SOC}.

Utilizing a tight-binding model for group-IV honeycomb crystals [43] it can be shown that the decoupling of bulk and edge states, and thus the appearance of helical edge states, can be indeed achieved by further increasing the ribbon width or the SOC in accordance to our findings presented in Fig. 3.13. However, the proposed nanoribbon sizes for germanene are far beyond the size that can be treated by first-principle methods.

Similarly to zigzag nanoribbons, the possibility of magnetic edges has to be taken into account. However, we have performed test calculations which suggest that the ground state of armchair ribbons always remains nonmagnetic, even if the starting configuration of the ribbon before the self-consistent cycle is magnetic. Our findings in germanene nanoribbons are in agreement with previous works on graphene and silicene nanoribbons [156, 158, 162].

3.4 Functionalized germanene

In the last sections it has been shown that pristine germanene possesses a nontrivial topology, although the linear helical surface states are strongly modified. However, the bulk bandgap is comparable small and thus, linear surface bands are absent in the finite nanoribbon system. Therefore, opening the bandgap by chemical functionalization might lead to decoupling of the bulk and edge states. The states around the Fermi level in pristine germanene are dominated by π orbitals. Consequently, due to functionalization these π bonds turn into σ bonds which opens a huge gap at the Dirac points.

Si *et al.* [154] suggested halogenation with iodine of a single layer of germanene, in the following abbreviated as GeI, as a promising TI material. Hydrogenation as well as halogenation leads to a noble gas configuration when bonding to a p_z orbital of Ge. However, only halogenation with iodine leads to the opening of a sizable bandgap of 0.3 eV at the Γ point of the 2D hexagonal BZ. In contrast, hydrogenation or halogenation with e.g. fluorine atoms opens a too large bandgap and the formation of a trivial insulator. The strong SOC within the σ orbitals and the coupling of p_{xy} orbitals of Ge and heavy

halogens plays a key role in the enlargement of the gaps in halogenated germanene. The nontrivial $\mathbb{Z}_2$ topological order is due to *s-p* band inversion at the Γ point.

In GeI the upwards (downwards) buckled Ge atom covalently bonds to one iodine atom above (below) the 2D crystal plane leading to the same symmetry as pristine germanene. We again use the HSE06 functional in order to generate trustable approximate quasiparticle bandgaps. Without SOC GeI is gapless with valence and conduction bands touching each other at the Γ point. Including SOC an indirect bandgap of about 0.3 eV (direct bandgap of 0.4 eV) is opened in the vicinity to the Γ point, leading to a mexican-hat-like band structure of the highest valence band around Γ. The corresponding band structure can be found in Fig. 3.14.
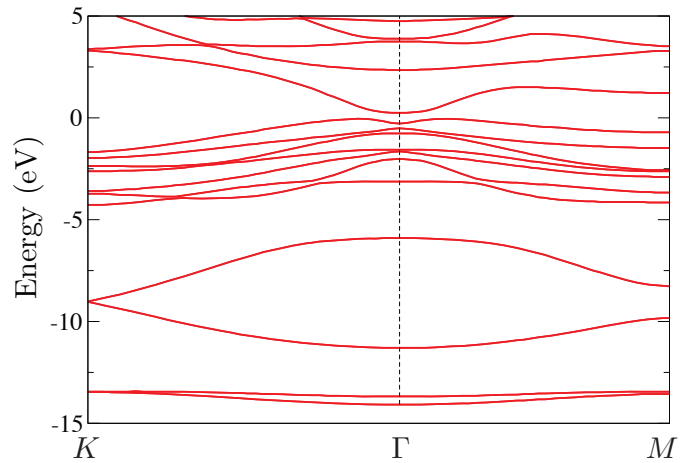
Figure 3.14: Band structure of halogenated germanene along the high-symmetry directions of the 2D hexagonal BZ. The Fermi energy is chosen as the energy zero.

GeI possesses inversion symmetry, consequently, the $\mathbb{Z}_2$ invariant is determined by means of the parities of the occupied bands at Γ and the three M points of each Kramers degenerate pair of eigenstates. The parities can be found in Tab. 3.3. It clearly shows the nontrivial

Γ	+	−	+	−	+	+	+	−	−	−	+	$(-)$
$3M$	−	+	−	+	+	−	−	+	−	+	−	$(+)$

Table 3.3: Parities of all eleven occupied bands at $\boldsymbol{\Gamma}$ and the three $\boldsymbol{M}$ points. The last column denotes the product δ_i of all parities at the corresponding momentum.

topology corresponding to $\mathbb{Z}_2 = 1$, which is due to the band inversion at the Γ point.

The appearance of chiral gapless edge states for GeI nanoribbons has been confirmed by other theoretical groups using DFT [154].

Chapter 4

Influence of substrates

It was proven by first-principles studies that free standing graphene, silicene, germanene and stanene are (meta)stable materials and exhibit Dirac cones with linear band dispersion near K or K' despite the partial sp^3 bonding. The major problem of the application of the group-IV honeycomb crystals is their preparation, which usually results in 2D structures on substrates. Here we investigate exclusively the deposition of silicene on metallic [103, 104] and nonmetallic [106, 107] substrates by means of DFT calculations.

An appropriate substrate for the epitaxial deposition of silicene should fulfill several conditions:
(i) A metallic substrate should be immiscible or not form a silicide with silicon.
(ii) The silicene lattice and the surface lattice should be nearly commensurable. A small biaxial strain of silicene is allowed.
(iii) The chemical interaction with the substrate should be weak, so that neither symmetry breaking nor the opening of large gaps occur due to the formation of covalent, ionic or vdW bonds.

4.1 Silicene on Ag(111)

The Ag(111) substrate is simulated using symmetric slabs with nine atomic layers. The irreducible (111) crystal slab contains three atomic layers [102] with a lateral (surface) lattice constant of $a = 2.89\,\text{Å}$ including vdW interaction ($a = 2.85\,\text{Å}$ in DFT-LDA), which agrees very well with the value of $a = 2.892\,\text{Å}$, which is the experimental cubic lattice constant of Ag. The extent of the vacuum region between the overlayers of two neighbored slabs is fixed at $15\,\text{Å}$. The starting atomic configurations are constructed by adding slightly biaxially strained silicene on both sides of the Ag slabs in agreement with the chosen translational symmetries of the substrate and overlayer to obtain a coincidence lattice

(see 1.8). The Si atoms and two Ag layers on both sides of a slab are allowed to relax. Thereby, the BZ of a given repeated slab system is sampled by a Γ-centered 8×8×1 $\boldsymbol{k}$-point mesh.

We find the coincidence of four silicene-overlayer structures on the Ag(111) substrate, so that the hexagonal unit cells of the slightly biaxially strained silicene sheet and the silver substrate fit to each other roughly. The sheet structures of silicene and the possibility of rotations around the surface normal predict several coincidentally matched adsorbates, which yields five geometries: two structures (i/ii) for $(\sqrt{7} \times \sqrt{7})$R19.1° silicene on a Ag(111)$(\sqrt{13} \times \sqrt{13})$R13.9° substrate and one structure for each of the following coincidence lattice arrangements: (iii) 3×3 on 4×4, (iv) 2×2 on $(\sqrt{7} \times \sqrt{7})$R19.1°, and (v) $(\sqrt{7} \times \sqrt{7})$R19.1° on $(2\sqrt{3} \times 2\sqrt{3})$R30° where the Wood notation is applied [102]. All the five overlayer structures give rise to local minima on the total-energy surface. When taking the translational symmetry constraints into account, they represent an, at least, metastable silicene-derived adsorbate structure on the Ag(111) substrate. The atomic geometries resulting after atomic relaxation are displayed in Fig. 4.1 The Cartesian coordinate system
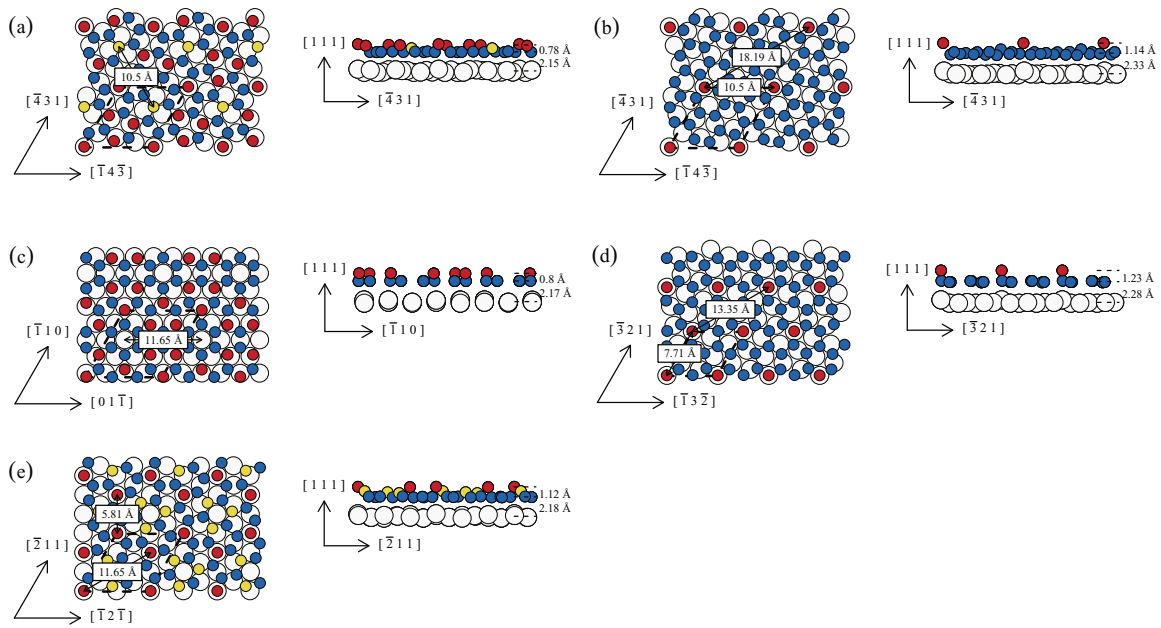
Figure 4.1: Top (left) and side (right) view of the relaxed silicene and first Ag(111) layer for the five geometries (a) $\sqrt{7} \times \sqrt{7}$ on $\sqrt{13} \times \sqrt{13}$ I, (b) $\sqrt{7} \times \sqrt{7}$ on $\sqrt{13} \times \sqrt{13}$ II, (c) 3×3 on 4×4, (d) 2×2 on $\sqrt{7} \times \sqrt{7}$, and (e) $\sqrt{7} \times \sqrt{7}$ on $2\sqrt{3} \times 2\sqrt{3}$. The uppermost (lower) Si atoms are indicated by red (blue) circles while the first-layer Ag atoms are indicated by gray dots. Si atoms at intermediate positions are indicatd by yellow circles. The crystallographic directions are related to the [111]-oriented cubic silver substrate. The unit cell of the adsorbate is displayed by dashed lines. Characteristic lateral and vertical distances are also given.

applied is $x \parallel [01\bar{1}]$, $y \parallel [\bar{2}11]$, and $z \parallel [111]$. At first glance, all the structures seem to keep

essentially honeycomb symmetry as indicated by the hexagonal arrangement of the Si atoms in top view. However, in contrast to ideal freestanding silicene, in which neighboring Si atoms are displaced alternately perpendicular to the sheet plane, the number and the arrangement of the outward buckled Si atoms vary. The threefold honeycomb symmetry is broken for the buckled silicene-derived geometries on Ag(111), as shown by the side views in Fig. 4.1. The optimized geometries agree qualitatively with the structures computed in other DFT calculations [169] using an XC functional within the DFT-GGA and a smaller plane-wave cutoff. A dependence of the actual atomic geometry on the used exchange-correlation functional is only found for the $\sqrt{7} \times \sqrt{7}$ on $2\sqrt{3} \times 2\sqrt{3}$ [Fig. 4.1(e)] coincidence system. In this system, the usage of the LDA approximation results in the disappearance of the in-between silicene layer. Two atoms per unit cell move into the top layer. Within the GGA approximation or with applied tensile strain within the LDA, the three atoms leave the in-between layer into the lower silicene layer. Only the vdW approach yields an arrangement of outward buckled Si atoms in agreement with STM findings.

The strong deviations of the silicene overlayer from the ideal hexagonal silicene are due to the strong chemical interactions with the substrate. We have shown that, as a consequence, a strong hybridization of Si and Ag states occurs which completely destroys the Dirac cones of freestanding silicene [103]. In order to observe structural and electronic properties related to freestanding silicene despite adsorption on a substrate it is necessary to reduce the adsorbate-substrate interaction. There are three possibilities: (i) an intercalation of the two systems, (ii) search for a substrate with reduced interaction with silicene, and (iii) the attempt to grow a van der Waals-bonded silicene sheet on top of one of the five adsorbate systems. In such a case, the adsorbate system may serve as a new substrate. In the following we will focus on new substrates with reduced substrate-adsorbate interaction.

4.2 Silicene on hydrogen-passivated Si(111) and Ge(111) substrates

The adsorption of hydrogen converts the Si(111)2×1 or Ge(111)2×8 reconstructed surfaces into Si(111):H-1×1 surfaces [170]. Strong group-IV-H-bonds are formed. The hydrogen atoms saturate completely all dangling bonds of the top substrate atoms, while the 2D hexagonal symmetry of the uppermost group-IV layer is conserved. The Si(111)1×1 surface is perfectly lattice-matched to the Bravais lattice of 1×1 silicene. Despite the two Si atoms in a (1×1) unit cell of silicene their remarkable buckling leads to a lattice constant that

deviates less than 1% from the 2D lattice constant of the surface (cf. Table 4.1). The

parameter	freestanding	Si(111):H	Ge(111):H	Cl/Si(111)1×1	CaF$_2$(111)1×1
a (Å)	3.86	3.86	4.08	3.86	3.88
Δ (Å)	0.48	0.48	0.39	0.49	0.43
D (Å)	–	2.68	2.01	3.12	2.70
v_F (10^6 m/s)	0.48	0.46	0.42	0.48	0.49
E_g (meV)	0	56	66	3	52

Table 4.1: Lattice constant a and buckling parameter Δ of freestanding and adsorbed silicene from total-energy DFT calculations including vdW interactions. The distance D of the bottom silicene atom and the hydrogen characterizes the adsorbate-substrate interaction. In addition the most important parameters of the electronic structure near the K or K' point of the BZ, the Fermi velocity v_F and the energy gap E_g are listed.

deviation increases for the Ge(111)1×1 substrate to about 4%. Test calculations show, however, that the Dirac cones of freestanding silicene remain up to a tensile strain of this order of magnitude.

The structural optimization and total-energy calculations are performed within the DFT, where the van der Waals (vdW) interaction is included according to Sec. 1.3.4. The H-passivated-IV(111)1×1 and silicene-covered IV(111):H-1×1 surfaces are simulated by repeated symmetric slabs (cf. 1.5) of 18 Si layers covered on both sides by hydrogen. On each surface one silicene sheet is adsorbed. The vacuum between two slabs is increased to 20 Å. The BZ of the superlattice is sampled with a $16 \times 16 \times 1$ $\boldsymbol{k}$-point grid.

4.2.1 Structure and energetics

The structural parameters of the silicene overlayers are summarized in Table 4.1. The vdW interaction slightly increases the buckling Δ compared to the case without vdW (see Table 2.1), while the lattice constant a decreases. Because of the slightly larger lattice constant of the hexagonal Si(111)1×1 and Ge(111)1×1 lattice, the lattice constant of the deposited silicene slightly increases while the buckling is reduced. These structural changes are in qualitative agreement with a minor reduction of the sp^3 hybridization in the silicene overlayer.

One important question for the growth of silicene on top of the passivated IV(111):H-1×1 surfaces is the arrangement of Si atoms in silicene with respect to the H atoms and the group-IV atoms in the uppermost atomic layers. The resulting atomic geometries in top, side, and perspective view are displayed in Fig. 4.2(a), (b), and (c). The corresponding energy landscape exhibits a pronounced minimum. Rotation of the Bravais lattice of silicene
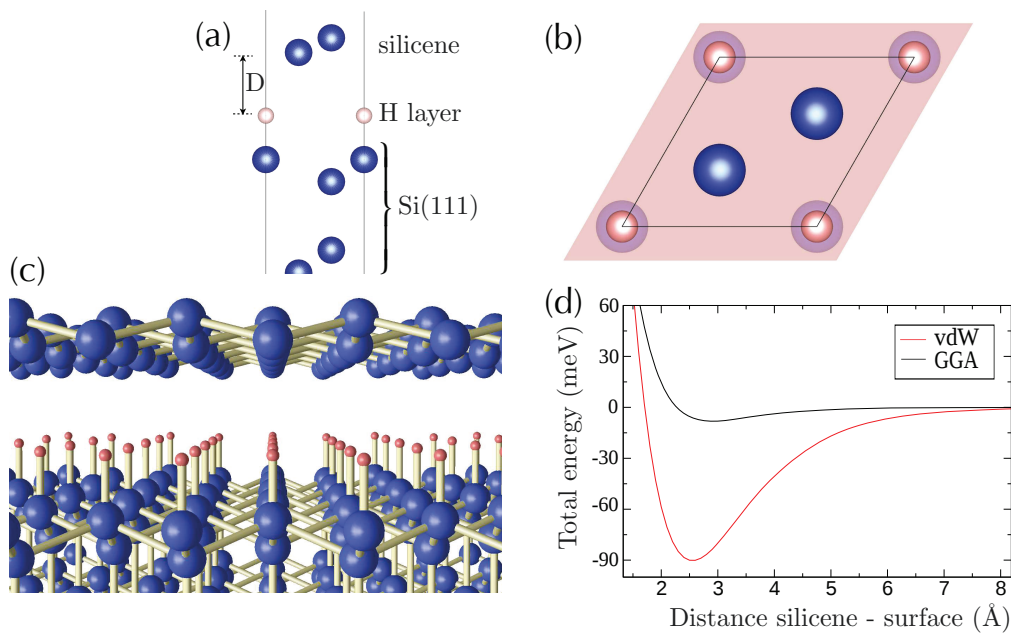
Figure 4.2: (a) Side view, (b) top view, and (c) perspective view on the relaxed silicene adsorbate on the Si(111):H-1×1 surface. The Si (H) atoms are displayed as blue (red) spheres. The distance D between adsorbate and surface and the lateral unit cell are indicated. (d) Total energy per silicene atom of the silicene−Si(111):H-1×1 adsorbate system versus distance D using the GGA-PBE and vdW functional.

and of the surface against each other are energetically less favorable. As a consequence laterally two Si atoms in a silicene unit cell occupy symmetric positions at the long diagonal of the rhombus representing a primitive 1×1 unit cell.

The stability of the silicene overlayer on the passivated substrates is ruled by the energy gain due to adsorption. This energy is characterized in Fig. 4.2(d) as a function of the silicene−substrate distance D, which is defined as vertical distance between the lowest Si atoms in silicene and the H atoms of the substrate. Figure 4.2(d) clearly shows that the silicene adsorbed on a passivated IV(111)1×1 surface is a vdW bonded system. Covalent and ionic bonding to the substrate are negligible. The adsorption of the slightly strained 2D silicene crystal on a passivated Si(111) [Ge(111)] surface gains energy of 91 (93) meV per silicon atom in the silicene overlayer. This value is large compared to the thermal energy $k_BT = 25$ meV at room temperature. Hence, the systems should be stable against thermal fluctuations. To give each silicene atom more degrees of freedom when relaxing, also larger unit cells, e.g. a 3×3 reconstruction, are investigated. Even for small displacements of some atoms from the pre-relaxed positions, all atoms move back into their equilibrium positions obtained for the corresponding 1×1 unit cells. So the silicene overlayer keeps intact despite more structural degrees of freedom.

Another important point concerns the stability of the silicene-covered IV(111):H surface

against the formation of a growing but still H-passivated (111) surface. The presence of adatoms reduces the stability of the H-passivated surface. For that reason we have performed additional total-energy calculations. Indeed, the H-passivated Si(111) surface is the energetically most favorable state of the system. However, there exists an energy barrier between the silicene-adsorbate and the passivated bulk-like system. In order to approximate this barrier we simulate the breaking of single Si(ad)-H-Si(bulk) bonds into [Si(ad)-H] and [Si(bulk)] subsystems on a 2×2 reconstructed Si(111):H surface. We obtain an energy barrier of about 1 eV. Of course, it can only serve as a crude approximation. Nevertheless, this result is supported by recent adsorption experiments. Hauch et *al.* [171] showed experimentally that deposition of Co atoms on Si(111):H is possible without replacing the H atoms.

4.2.2 Electronic properties

The band structure of the silicene-covered H-passivated Si(111)1×1 surface is displayed in Fig. 4.3(a). The regions of the dense slab bands mainly indicate the projected bulk Si
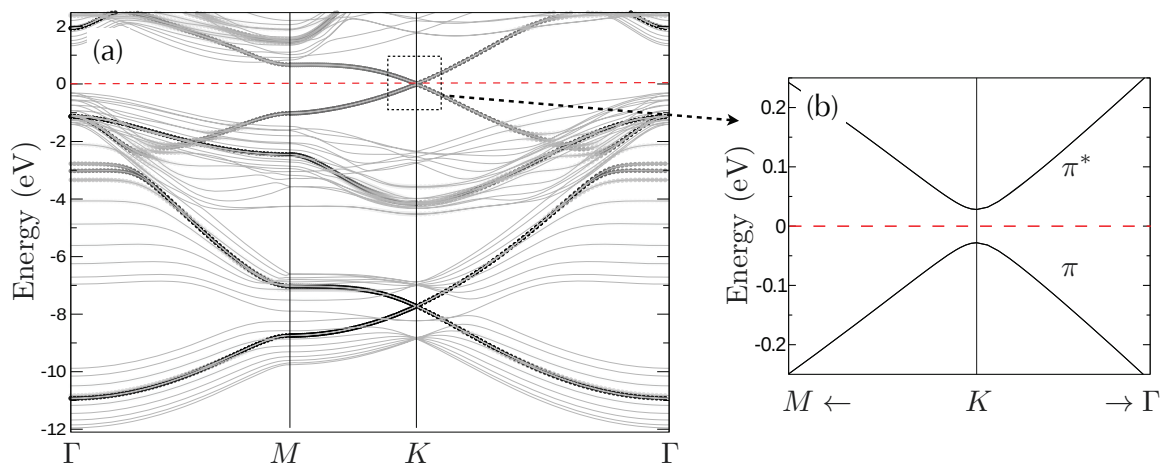
Figure 4.3: (a) Band structure of silicene adsorbed on Si(111):H-1×1 substrate. The silicene character obtained by projections onto the silicene atoms is indicated by black dots with varying intensity of the color. (b) Dirac cone-derived bands near the Fermi level and around a K point. The red-dashed horizontal lines represent the Fermi level.

band structure. A Si-H-derived surface band only appears in the pocket of the projected bulk Si band structure around a K point in the BZ in the valence bands near -8 eV. The silicene-derived bands agree well with the band structure of freestanding silicene in Fig. 2.4(b). This fact indicates the weak interaction between adsorbate and substrate, which is mainly due to vdW interaction, and its associated structural changes. This weak interaction is also visible in the band structure around K and the Fermi level in Fig. 4.3(b). The Dirac cones are almost conserved but slightly deformed near K due to a gap opening

of 56 meV or a somewhat larger value for the Ge(111):H-1×1 substrate (see Table 4.1). A similar gap opening has been described for graphene on a substrate [172]. It is mainly due to the interaction of the p_z orbitals with the substrate which depends on the distance between lower silicon atoms and surface. Together with the Fermi velocity v_F it approximately determines the conduction- and valence-band dispersion by $\sqrt{(E_g/2)^2 + (\hbar v_F \Delta k)^2}$. The Fermi velocity also decreases with increasing gap size (cf. Table 4.1). We point out that the Dirac cones still appear in the fundamental gap of the projected bulk band structure as a consequence of the weak adsorbate-substrate interaction. The corresponding silicene states are non-resonant or bound states compared to the electronic structure of the substrate.

In order to understand better the weak adsorbate-substrate interaction, in Fig. 4.4 we display the difference of the adsorbate system and the sum of the densities computed for the isolated silicene and substrate but keeping their atomic geometries. First of all,
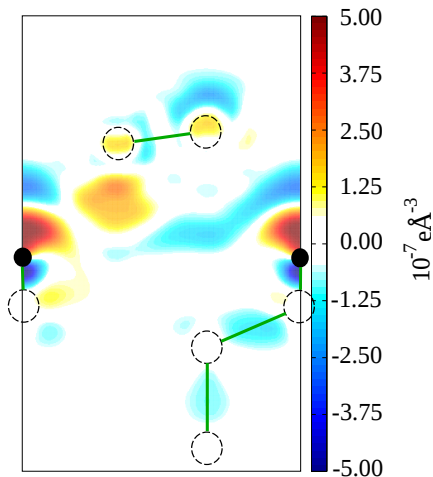

Figure 4.4: Difference of electron densities between the adsorbate system and the isolated silicene and substrate are displayed in a (110) plane of the cubic substrate lattice. Electron accumulation (depletion) is indicated by red (blue) regions. Si atoms are indicated by large circles, while H atoms are represented by black dots. The modifications are given in units of 10^{-7} elementary charges/Å^3. Chemical bonds are highlighted with green solid lines.

the redistribution of electrons is extremely small in agreement with the finding that the silicene overlayer is only vdW-bonded at the IV(111):H-1×1 substrates. The passivated substrate looses electrons in the uppermost bonds. They mainly appear in front of the H atoms. Extremely weak hydrogen-bridge bonds to the silicene may be also formed, especially to the lower Si atoms in the buckled silicene. In addition, the silicene overlayer is somewhat electrically polarized. A weak dipole layer is formed between the outward and inward buckled silicene atoms. The corresponding electric field is mainly responsible for the opening of the small gaps at the K points (cf. Table 4.1).

4.3 Nonmetallic substrates for growth of silicene

Here we investigate the growth of silicene on two novel substrates, Cl-passivated Si(111)1×1 and clean CaF_2(111)1×1 surfaces as indicated in Fig. 4.5. Both substrates possess a
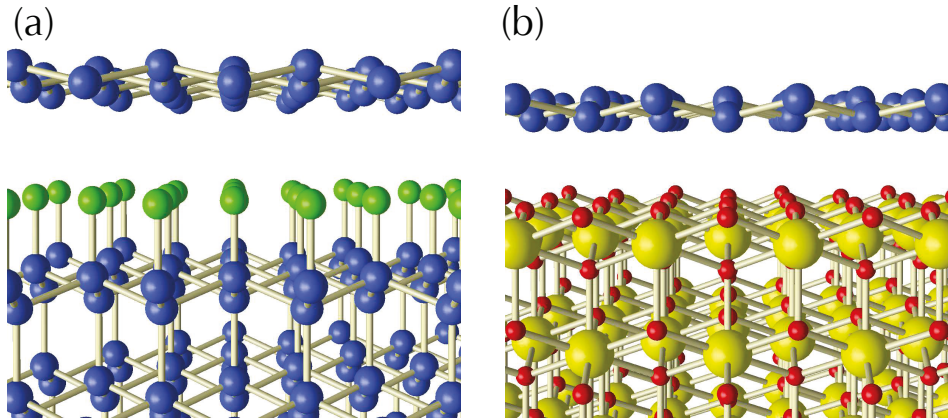
Figure 4.5: Silicene adsorbed on (a) Cl-passivated Si(111)1×1 and (b) clean CaF$_2$(111)1×1 surface. Si atoms: blue, Cl: green, Ca: yellow, F: red.

fundamental bandgap which is advantageous for the possible observation of Dirac cones of silicene overlayer. The Cl-passivated Si(111)1×1 and the CaF$_2$(111)1×1 surfaces are simulated by repeated symmetric slabs of 18 and 24 atomic layers respectively. In the Si case both sides are covered by chlorine. In the CaF$_2$(111) slabs, fluorine layers form the surfaces. Additionally, on each slab surface one silicene sheet is adsorbed. The vacuum between two slabs is chosen to be 20 Å. The slightly biaxially strained silicene, the chlorine layer, and the uppermost atomic layers in the slab are allowed to relax. The BZ is sampled with a $16 \times 16 \times 1$ **k**-point grid. Many different starting geometries with different displacements of the strained silicene overlayer relative to the positions of the Cl or F surface atoms are investigated.

4.3.1 The substrates

Upon reaction of Cl atoms with the cleavage Si(111)7×7 surface and subsequent repeated annealing, the favorable bulk like 1×1 surface appears [173]. A stable monolayer of Cl$^-$ ions covers the Si(111)1×1 surface with almost Si$^+$ ions in the topmost atomic layer. The projected fundamental gap with a minimum of 1.1 eV is free of surface states. The Cl/Si(111)1×1 surface is indeed passivated, while the 2D hexagonal symmetry of the uppermost Si layer is conserved. The Si(111)1×1 surface is perfectly lattice-matched to the Bravais lattice of the 1×1 silicene sheet with a deviation of only 0.1% (see Table 4.1).

The natural cleavage CaF$_2$(111)1×1 surface is terminated by a complete triple layer of F$^-$-Ca^{2+}-F$^-$ monoatomic layers with a topmost F$^-$ layer for electrostatic reasons [174]. The latter one consists of a trigonal arrangement of F$^-$ ions spaced by 3.88 Å (see Table 4.1), that leads to a lattice mismatch to silicene of 0.5%. Because of the inertness of the

CaF$_2$(111)1×1 surface it is suggested as a convenient substrate for a vdW epitaxy of almost strain-free overlayers [175]. The completely filled outermost electron shell of the F$^-$ ions makes the uppermost surface triple layer inert. The silicene atoms should not chemically react with an intact triple layer surface, similar to the behavior of oxygen atoms [176].

4.3.2 Structure and energetics

In the resulting minimum-energy structure of silicene on Cl/Si(111)1×1 the two silicene atoms in the unit cell occupy high-symmetric positions at the long diagonal of the rhombus but representing the primitive 1×1 surface cell. The bucking amplitude Δ of the silicene sheet is little influenced. The stable position of the sheet in a distance of $D = 3.12$ Å (see Table 4.1) is mainly caused by the vdW dispersion forces. Despite the large distance, the binding energy $E_B = 215$ meV/cell is larger than for silicene on Si(111):H-1×1 because of the increased dipole moment of the Cl$^-$-Si$^+$ bonds. This value is large compared to the thermal energy $k_B T = 25$ meV at room temperature. There is an energy barrier between the silicene adsorbate system (configuration 0) compared to the Cl-passivated Si(111)1×1 substrate with two more Si layers (configuration 1) of about 4.1 eV/1×1 cell. To approximate this barrier we displace the two Si atoms of silicene and the Cl atom in 18 steps toward configuration 1 on condition that the distance of two atoms never comes below the sum of the covalent radii. Of course, the calculated energy barrier is very high due to the constraint of a 1×1, but it clearly shows that the silicene configuration on an intact Cl-passivated Si(111) surface represents a true local minimum on the total-energy surface, and that this configuration should be stable against thermal fluctuations.

The results for a F$^-$-terminated CaF$_2$(111)1×1 substrate are rather similar. However, as a consequence of the slightly increased biaxial strain, the buckling amplitude of silicene is reduced (see Table 4.1). The distance $D = 2.70$ Å between overlayer and substrate is somewhat smaller than in the Cl/Si(111)1×1 case but still indicates an influence of the vdW bonding.

To investigate the influence of the 1×1 unit-cell constraint, we have also studied 3×3 lateral unit cells for both substrates, Cl/Si(111) and CaF$_2$(111). Despite significant initial displacements, the silicon overlayers relax back into the silicene geometry optimized within 1×1 cells. This result supports the statement of a stable configuration.

The band structures of the silicene-covered (a) Cl-passivated Si(111) surface and (b) CaF$_2$(111) substrate are displayed in Fig. 4.6. The regions of the dense slab bands mainly indicate the projected bulk (a) Si or (b) CaF$_2$ band structures. The striking difference
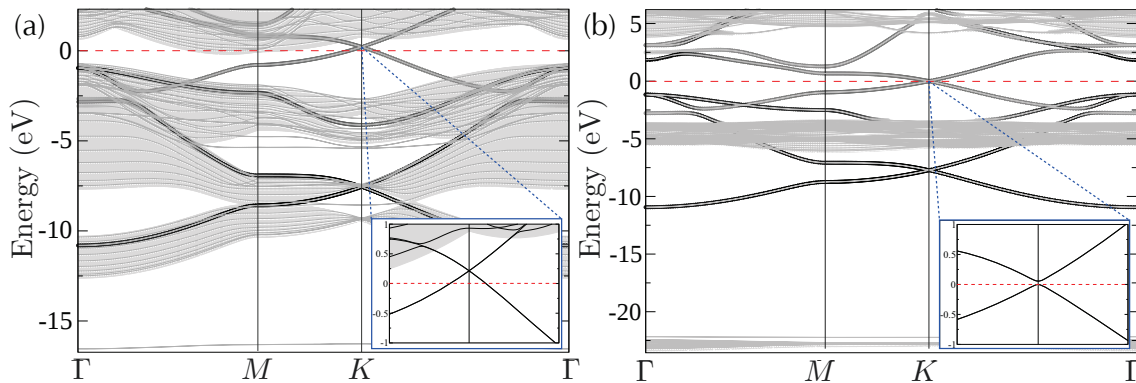
Figure 4.6: Band structures of silicene adsorbed on (a) Cl/Si(111)1×1 and (b) CaF$_2$(111)1×1, respectively. The silicene character obtained by projection onto corresponding Si atoms is indicated by black dots with varying intensity of color. The red-dashed horizontal line represents the Fermi level.

in the chemical bonding of the substrates are indicated by the completely different band widths and energy gaps. The gaps are free of surface states. Such states associated with Cl-Si bonds near K and M only appear in the pockets of the projected valence bands. The electronic-structure modifications due to the silicene overlayer are indicated by additional bands whose chemical nature has been determined by projections onto the silicene atoms. As a consequence of the weak vdW bonding one observes the almost unchanged band structure of freestanding silicene. This is especially true for the Dirac cones around K within the fundamental gaps. The corresponding band states are still derived mainly from Si p_z orbitals.

The weak vdW bonding only slightly modifies the bands near the K point. The Fermi velocities of the Dirac cones are conserved (see Table 4.1). In the case of the Cl/Si(111) substrate, practically no gap is opened. Only the Fermi level is shifted by 0.2 eV toward lower energies, i.e., holes are created in the π-state-derived cone. The projected bulk conduction band minima near M indicate a small electron transfer into the substrate. On CaF$_2$(111) the silicene overlayer opens a small gap between the π^* and π cones. The Fermi energy remains in the gap center.

The outstanding properties known from freestanding silicene are preserved for the slab system, because of the weak bonding. We suggest intensive experimental studies of the deposition of silicene on the investigated nonmetallic substrates. In contrast to the silicene/Ag(111) adsorbate system with strong chemical bonds, the electronic structure of silicene should be detectable within the fundamental gaps of the studied substrates.

Summary and Conclusions

We have studied the structural, electronic and optical properties of the 2D group-IV honeycomb crystals graphene, silicene, germanene and stanene by ab-initio calculations based on DFT within the independent (quasi-)particle approach. The calculations of the atomic structure of silicene, germanene and stanene reveals a tendency to partly sp^3 hybridization leading to slightly buckled structures, whereas graphene remains atomically flat due to sp^2 hybridization. We determined the full electronic structure of the crystal sheets by means of semilocal and nonlocal exchange-correlation functionals. Surprisingly, despite buckling all crystals share very similar electronic properties around the Fermi level. In particular, without spin-orbit coupling (SOC), they can be considered as zero-gap semiconductors with massless Dirac fermions appearing in the vicinity of the K and K' points in the electronic band structure. Taking also into account (approximate) quasiparticle effects by means of the HSE06 functional we obtained the Fermi velocity of the isotropic Dirac cones in good agreement with experimental data. For silicene, germanene and stanene the increasing importance of spin-orbit coupling was pointed out, which introduces an electronic bandgap at the Dirac points and consequently, effectively turns these crystals into insulators. The bandgap increases along the row C→Si→Ge→Sn and is larger in HSE than that obtained with standard DFT functionals.

We have studied the real and imaginary part of the frequency-dependent optical conductivity of the 2D honeycomb crystals. Special care was taken to compute converged spectra, in particular in the long-wavelength limit, with respect to the sampling of the Brillouin zone. In this limit we found an optical absorbance of $\pi\alpha$ as predicted for massless Dirac fermions in graphene. This result, assuming no SOC, is explained analytically by the isotropic linear band structure around the K (or K') points and optical interband matrix elements at these points which can be universally related to the Fermi velocity v_F of the 2D material. This result is universal for all group-IV crystals independent of v_F, the hybridization, the sheet buckling, the applied gauge of the electromagnetic field, and the exchange-correlation functional. For higher frequencies the absorbance spectra start to deviate significantly with the group-IV material. While both many-body and relativistic effects modify the electronic structure near the Dirac points, the modification of the optical

absorbance is restricted to a narrow frequency region near the SOC-induced fundamental bandgap. The finiteness of the bandgap gives rise to a drastic modification of the optical transition matrix elements for small photon energies and, hence, close to a Dirac point. No absorption happens for $\hbar\omega < E_\mathrm{g}$, while the absorbance $A(\omega = E_\mathrm{g}/\hbar + 0^+) = 2\pi\alpha$ near the gap is increased. In the frequency region between the gap and optical interband energies the absorbance value $A(\omega) = \pi\alpha$ is recovered. The results are independent of the group-IV honeycomb structure, but more pronounced for heavier elements.

The influence of an infinitely thin 2D crystal on the frequency-dependent optical reflectance, transmittance, and absorbance was investigated by means of the 2D sheet conductivity. For freestanding honeycomb crystals the reflectance is vanishingly small outside the resonance frequencies. Despite the small layer thickness the absorption of such a 2D crystal is not vanishing. Rather, near the optical resonances the absorbance $A(\omega)$ approaches large values, one order of magnitude larger than the approximate zero-frequency value $A(\omega) = \pi\alpha$. The impact of a finite width by means of the full 3D conductivity tensor is discussed. It is shown to which extend the approximation of an infinitely thin conducting sheet holds for the description of the optical properties of the 2D sheet crystals in terms of the wavelength of the incident light and the thickness of the sheet.

We implemented two methods based on the wave functions obtained within the DFT scheme that allowes the classification of arbitrary 2D and 3D insulators into trivial and topological insulators, where the latter one give rise to the quantum spin-Hall effect. We have shown, that the group-IV honeycomb crystals silicene, germanene and stanene are indeed topological insulators. By applying an external electric field perpendicular to the 2D sheet plane we have shown, that a topological phase transition into a trivial insulator occurs above a critical field strength, that depends on the 2D crystal.

We have studied the edge states of germanene nanoribbons with zigzag and armchair edges. We have discussed the spin texture and the band dispersions of the resulting band states, especially those of the edge states. It has been shown that there exist gapless parabolic bands with opposite spin texture near the Fermi level and the X points of the Brillouin zone boundary. The corresponding wave functions are localized at the edges of the nonmagnetic nanoribbon. The spin-polarized parabolas undergo a Rashba-like band splitting. In contrast to the insulating germanene sheet, the nonmagnetic nanoribbon is metallic. However, the energetically favored ground-state is antiferromagnetic due to an opening of a bandgap between the surface states. Consequently, the ground state of the nanoribbon becomes insulating. Our results clearly demonstrate that the picture of the topological character of such nanoribbons predicted by simpler tight-binding models has to be modified. Similar discrepancies between the model and the self-consistent

ab-initio approach are also found for the influence of an external vertical electric field on the topological character. Whereas for infinite 2D germanene sheets we state agreement concerning the phase transition between a TI and a trivial band insulator, this is not the case for the ribbons. Therefore, we also studied halogenated germanene, which exhibits a increased SOC-induced bandgap compared to pristine germanene. Halogenated germanene was identified as a topological insulator with promising edge states, which may give rise to possible applications in spintronics.

In order to simulate a more realistic experimental situation, also silicene on Ag(111) substrates has been systematically investigated by DFT with van der Waals interaction for various Si coverages, biaxial strains, and translational symmetries resulting in five different adsorbates. The atomic structure and the band structures for the silicene-silver adsorbate systems generally indicate a strong chemical interaction between silicene atom and the atoms in the silver surface. Therefore, we focused our attention on the insulating substrates Si(111) passivated with hydrogen and chlorine, as well as CaF_2 with strongly reduced adsorbate-substrate interaction. These systems are stabilized by van der Waals interactions. The associated weak bonding has only a minor influence on the electronic structure of the adsorbed silicene. Only very small gaps are opened which even slightly deform the Dirac cones at the corner points of the Brillouin zone. In contrast to the Si/Ag(111) adsorbate system with strong chemical bonds, here the overlayers represent silicene also from the point of their electronic properties.

Concluding, the two-dimensional sheet crystals that once began with the exfoliation of a single graphene sheet, opened an entirely new field of physics about the two-dimensional electron gases in solid state systems. The peculiar electronic properties in these ultra thin crystals give rise to a further miniaturization of electronic circuits to the nanoscale, while increasing the efficiency and speed of electronic components. The topological character of the helical edge states of some 2D crystals may lead also to potential applications in the strongly developing field of spintronics.

The optical properties of 2D sheet crystals are not yet fully understood and offer a huge potential for further improvement. An increase of the optical absorption of germanene and stanene due to the impact of the SOC is not confirmed experimentally since both crystals have not been synthesized so far. We hope, that the increasing interest in stanene will lead to its realization within the next few years. In particular the question arises, if the tensorial character of the conductivity does affect the optical properties in an optical ellipsometry experiment. Therefore, we suggest the experimental investigation of reflection, transmission and absorption at oblique incidence with polarized light at high photon energies for investigating this effect.

Another interesting question concerns the impact of the topological character of the 2D sheet crystal on its optical conductivity. If the strength of an external electric field applied perpendicular to the sheet plane is tuned in such a way, that the SOC-induced electronic bandgap is equivalent to the field-free case, is there any signature in the optical conductivity in the vicinity of the fundamental bandgap? Calculations on e.g. germanene could probably answer the question and lead to an in-depth understanding based on the optical matrix elements and the symmetry of the contributing wave functions.

We also hope, that our suggestions of substrates for the growth of silicene and germanene by means of van der Waals epitaxy will help also to find proper substrates for the growth of other 2D crystals. Combined with first-principles calculations it will be possible to determine precisely the atomic structure and the corresponding electronic properties.

Bibliography

[1] P. R. Wallace. The Band Theory of Graphite. In: *Phys. Rev.* **71** (9), pp. 622 (1947).

[2] H. P. Boehm, A. Clauss, G. O. Fischer, and U. Hofmann. Das Adsorptionsverhalten sehr dünner Kohlenstoff-Folien. In: *Zeitschrift für anorganische und allgemeine Chemie* **316** (3-4), pp. 119. ISSN 1521-3749 (1962).

[3] K. S. Novoselov, A. K. Geim, S. V. Morozov, D. Jiang, Y. Zhang, S. V. Dubonos, I. V. Grigorieva, and A. A. Firsov. Electric Field Effect in Atomically Thin Carbon Films. In: *Science* **306** (5696), pp. 666 (2004).

[4] K. S. Novoselov, A. K. Geim, S. V. Morozov, D. Jiang, M. I. Katsnelson, I. V. Grigorieva, S. V. Dubonos, and A. A. Firsov. Two-dimensional gas of massless Dirac fermions in graphene. In: *Nature* **438** (7065), pp. 197. ISSN 0028-0836 (2005).

[5] K. S. Novoselov, D. Jiang, F. Schedin, T. Booth, V. V. Khotkevich, S. Morozov, and A. K. Geim. Two-dimensional atomic crystals. In: *Proc. Natl. Acad. Sci. USA* **102**, pp. 10451 (2005).

[6] A. K. Geim and K. S. Novoselov. The rise of graphene. In: *Nat. Mater.* **6**, pp. 183 (2007).

[7] K. R. Paton, E. Varrla, C. Backes, R. J. Smith, U. Khan, A. O'Neill, C. Boland, M. Lotya, O. M. Istrate, P. King, T. Higgins, S. Barwich, P. May, P. Puczkarski, I. Ahmed, M. Moebius, H. Pettersson, E. Long, J. Coelho, S. E. O'Brien, E. K. McGuire, B. M. Sanchez, G. S. Duesberg, N. McEvoy, T. J. Pennycook, C. Downing, A. Crossley, V. Nicolosi, and J. N. Coleman. Scalable production of large quantities of defect-free few-layer graphene by shear exfoliation in liquids. In: *Nat Mater* **13** (6), pp. 624 (2014).

[8] Y. Zhang, Y.-W. Tan, H. L. Stormer, and P. Kim. Experimental observation of the quantum Hall effect and Berry's phase in graphene. In: *Nature* **438** (7065), pp. 201. ISSN 0028-0836 (2005).

[9] S. Y. Zhou, G.-H. Gweon, J. Graf, A. V. Fedorov, C. D. Spataru, R. D. Diehl, Y. Kopelevich, D.-H. Lee, S. G. Louie, and A. Lanzara. First direct observation of Dirac fermions in graphite. In: *Nat Phys* **2** (9), pp. 595. ISSN 1745-2473 (2006).

[10] R. Gillen and J. Robertson. The screened-exchange approximation as alternative method for DFT calculations on graphene structures. In: *physica status solidi (b)* **247** (11-12), pp. 2945. ISSN 1521-3951 (2010).

[11] M. I. Katsnelson. Zitterbewegung, chirality, and minimal conductivity in graphene. In: *The European Physical Journal B - Condensed Matter and Complex Systems* **51** (2), pp. 157. ISSN 1434-6028 (2006).

[12] A. B. Kuzmenko, E. van Heumen, F. Carbone, and D. van der Marel. Universal Optical Conductance of Graphite. In: *Phys. Rev. Lett.* **100** (11), p. 117401 (2008).

[13] F. Bechstedt, L. Matthes, P. Gori, and O. Pulci. Infrared absorbance of silicene and germanene. In: *Applied Physics Letters* **100** (26), 261906 (2012).

[14] L. Matthes, P. Gori, O. Pulci, and F. Bechstedt. Universal infrared absorbance of two-dimensional honeycomb group-IV crystals. In: *Phys. Rev. B* **87**, p. 035438 (2013).

[15] L. Matthes, O. Pulci, and F. Bechstedt. Massive Dirac quasiparticles in the optical absorbance of graphene, silicene, germanene, and tinene. In: *Journal of Physics: Condensed Matter* **25** (39), p. 395305 (2013).

[16] L. Matthes, O. Pulci, and F. Bechstedt. Optical properties of two-dimensional honeycomb crystals graphene, silicene, germanene, and tinene from first principles. In: *New Journal of Physics* **16** (10), p. 105007 (2014).

[17] L. Matthes, K. Hannewald, J. Furthmüller, and F. Bechstedt. Screening and band structure effects on quasi-one-dimensional transport in periodically modulated graphene. In: *Phys. Rev. B* **84**, p. 115427 (2011).

[18] M. I. Katsnelson, K. S. Novoselov, and A. K. Geim. Chiral tunnelling and the Klein paradox in graphene. In: *Nat Phys* **2** (9), pp. 620. ISSN 1745-2473 (2006).

[19] L. Matthes, K. Hannewald, and F. Bechstedt. *Ab initio* investigation of graphene-based one-dimensional superlattices and their interfaces. In: *Phys. Rev. B* **86**, p. 205409 (2012).

[20] H. Yang, J. Heo, S. Park, H. J. Song, D. H. Seo, K.-E. Byun, P. Kim, I. Yoo, H.-J. Chung, and K. Kim. Graphene Barristor, a Triode Device with a Gate-Controlled Schottky Barrier. In: *Science* **336** (6085), pp. 1140 (2012).

[21] A. Abbott and Q. Schiermeier. Research prize boost for Europe. In: *Nature* **493**, pp. 585 (2013).

[22] M. Peplow. The quest for supercarbon. In: *Nature* **503**, pp. 327 (2013).

[23] S. Cahangirov, M. Topsakal, E. Aktürk, H. Şahin, and S. Ciraci. Two- and One-Dimensional Honeycomb Structures of Silicon and Germanium. In: *Phys. Rev. Lett.* **102**, p. 236804 (2009).

[24] L. L. Yan Voon and G. Guzmán-Verri. Is silicene the next graphene? In: *MRS Bulletin* **39**, pp. 366. ISSN 1938-1425 (2014).

[25] P. Vogt, P. De Padova, C. Quaresima, J. Avila, E. Frantzeskakis, M. C. Asensio, A. Resta, B. Ealet, and G. Le Lay. Silicene: Compelling Experimental Evidence for Graphenelike Two-Dimensional Silicon. In: *Phys. Rev. Lett.* **108**, p. 155501 (2012).

[26] L. Chen, C.-C. Liu, B. Feng, X. He, P. Cheng, Z. Ding, S. Meng, Y. Yao, and K. Wu. Evidence for Dirac Fermions in a Honeycomb Lattice Based on Silicon. In: *Phys. Rev. Lett.* **109**, p. 056804 (2012).

[27] Y. Xu, B. Yan, H.-J. Zhang, J. Wang, G. Xu, P. Tang, W. Duan, and S.-C. Zhang. Large-Gap Quantum Spin Hall Insulators in Tin Films. In: *Phys. Rev. Lett.* **111**, p. 136804 (2013).

[28] C. L. Kane and E. J. Mele. Z_2 Topological Order and the Quantum Spin Hall Effect. In: *Phys. Rev. Lett.* **95**, p. 146802 (2005).

[29] D. Hsieh, D. Qian, L. Wray, Y. Xia, Y. S. Hor, R. J. Cava, and M. Z. Hasan. A topological Dirac insulator in a quantum spin Hall phase. In: *Nature* **452** (7190), pp. 970 (2008).

[30] C.-C. Liu, W. Feng, and Y. Yao. Quantum Spin Hall Effect in Silicene and Two-Dimensional Germanium. In: *Phys. Rev. Lett.* **107**, p. 076802 (2011).

[31] R. O. Jones and O. Gunnarsson. The density functional formalism, its applications and prospects. In: *Rev. Mod. Phys.* **61** (3), p. 689 (1989).

[32] R. M. Dreizler and E. K. U. Gross. *Density Functional Theory: An Approach to the Quantum Many-Body Problem.* Springer, Berlin. ISBN 3-540-51993-9 (1990).

[33] K. Burke. Perspective on density functional theory. In: *J. Chem. Phys.* **136**, p. 150901 (2012).

[34] A. D. Becke. Perspective: Fifty years of density-functional theory in chemical physics. In: *The Journal of Chemical Physics* **140** (18), 18A301 (2014).

[35] J. P. Perdew, M. Ernzerhof, and K. Burke. Rationale for mixing exact exchange with density functional approximations. In: *The Journal of Chemical Physics* **105** (22), pp. 9982 (1996).

[36] C. Adamo and V. Barone. Toward reliable density functional methods without adjustable parameters: The PBE0 model. In: *J. Chem. Phys.* **110** (13), pp. 6158 (1999).

[37] J. Heyd, G. E. Scuseria, and M. Ernzerhof. Hybrid functionals based on a screened Coulomb potential. In: *Journal of Chemical Physics* **118** (18), pp. 8207 (2003).

[38] J. Heyd, J. E. Peralta, G. E. Scuseria, and R. L. Martin. Energy band gaps and lattice parameters evaluated with the Heyd-Scuseria-Ernzerhof screened hybrid functional. In: *The Journal of Chemical Physics* **123** (17), 174101 (2005).

[39] J. Heyd, G. E. Scuseria, and M. Ernzerhof. Erratum: "Hybrid functionals based on a screened Coulomb potential" [J. Chem. Phys. 118, 8207 (2003)]. In: *Journal of Chemical Physics* **124** (21), 219906 (2006).

[40] L. Fu and C. L. Kane. Time reversal polarization and a Z_2 adiabatic spin pump. In: *Phys. Rev. B* **74**, p. 195312 (2006).

[41] L. Fu, C. L. Kane, and E. J. Mele. Topological Insulators in Three Dimensions. In: *Phys. Rev. Lett.* **98**, p. 106803 (2007).

[42] M. Ezawa. Topological phase transition and electrically tunable diamagnetism in silicene. In: *The European Physical Journal B* **85** (11), 363. ISSN 1434-6028 (2012).

[43] M. Ezawa and N. Nagaosa. Interference of topologically protected edge states in silicene nanoribbons. In: *Phys. Rev. B* **88**, p. 121401 (2013).

[44] R. R. Nair, P. Blake, A. N. Grigorenko, K. S. Novoselov, T. J. Booth, T. Stauber, N. M. R. Peres, and A. K. Geim. Fine Structure Constant Defines Visual Transparency of Graphene. In: *Science* **320** (5881), p. 1308 (2008).

[45] C.-L. Lin, R. Arafune, K. Kawahara, N. Tsukahara, E. Minamitani, Y. Kim, N. Takagi, and M. Kawai. Structure of Silicene Grown on Ag(111). In: *Applied Physics Express* **5** (4), p. 045802 (2012).

[46] A. Fleurence, R. Friedlein, T. Ozaki, H. Kawai, Y. Wang, and Y. Yamada-Takamura. Experimental Evidence for Epitaxial Silicene on Diboride Thin Films. In: *Phys. Rev. Lett.* **108**, p. 245501 (2012).

[47] Y. Yamada-Takamura and R. Friedlein. Progress in the materials science of silicene. In: *Science and Technology of Advanced Materials* **15** (6), p. 064404 (2014).

[48] G. Grosso and G. P. Parravicini. *Solid State Physics*. Academic Press, Cambridge (2003).

[49] T. Koopmans. Über die Zuordnung von Wellenfunktionen und Eigenwerten zu den Einzelnen Elektronen Eines Atoms. In: *Physica* **1** (1-6), pp. 104 . ISSN 0031-8914 (1934).

[50] J. B. Foresman, M. Head-Gordon, J. A. Pople, and M. J. Frisch. Toward a systematic molecular orbital theory for excited states. In: *The Journal of Physical Chemistry* **96** (1), pp. 135 (1992).

[51] P. Hohenberg and W. Kohn. Inhomogeneous Electron Gas. In: *Phys. Rev.* **136** (3B), pp. B864 (1964).

[52] R. M. Martin. *Electronic Structure*. Cambridge University Press (2004).

[53] W. Kohn and L. J. Sham. Self-Consistent Equations Including Exchange and Correlation Effects. In: *Phys. Rev.* **140** (4A), pp. A1133 (1965).

[54] D. M. Ceperley and B. J. Alder. Ground State of the Electron Gas by a Stochastic Method. In: *Phys. Rev. Lett.* **45** (7), pp. 566 (1980).

[55] J. P. Perdew and A. Zunger. Self-interaction correction to density-functional approximations for many-electron systems. In: *Phys. Rev. B* **23** (10), pp. 5048 (1981).

[56] J. P. Perdew, K. Burke, and M. Ernzerhof. Generalized Gradient Approximation Made Simple. In: *Phys. Rev. Lett.* **77** (18), pp. 3865 (1996).

[57] Y. Zhang and W. Yang. Comment on "Generalized Gradient Approximation Made Simple". In: *Phys. Rev. Lett.* **80**, pp. 890 (1998).

[58] U. von Barth and L. Hedin. A local exchange-correlation potential for the spin polarized case. i. In: *Journal of Physics C: Solid State Physics* **5** (13), pp. 1629 (1972).

[59] A. Schrön, C. Rödl, and F. Bechstedt. Energetic stability and magnetic properties of MnO in the rocksalt, wurtzite, and zinc-blende structures: Influence of exchange and correlation. In: *Phys. Rev. B* **82** (16), p. 165109 (2010).

[60] A. Schrön, C. Rödl, and F. Bechstedt. Crystalline and magnetic anisotropy of the $3d$-transition metal monoxides MnO, FeO, CoO, and NiO. In: *Phys. Rev. B* **86**, p. 115134 (2012).

[61] J. Kübler, K.-H. Höck, J. Sticht, and A. R. Williams. Density functional theory of non-collinear magnetism. In: *J. Phys. F* **18** (3), p. 469 (1988).

[62] T. Oda, A. Pasquarello, and R. Car. Fully Unconstrained Approach to Noncollinear Magnetism: Application to Small Fe Clusters. In: *Phys. Rev. Lett.* **80**, pp. 3622 (1998).

[63] D. Hobbs, G. Kresse, and J. Hafner. Fully unconstrained noncollinear magnetism within the projector augmented-wave method. In: *Phys. Rev. B* **62** (17), pp. 11556 (2000).

[64] M. Dion, H. Rydberg, E. Schröder, D. C. Langreth, and B. I. Lundqvist. Van der Waals Density Functional for General Geometries. In: *Phys. Rev. Lett.* **92**, p. 246401 (2004).

[65] G. Román-Pérez and J. M. Soler. Efficient Implementation of a van der Waals Density Functional: Application to Double-Wall Carbon Nanotubes. In: *Phys. Rev. Lett.* **103**, p. 096102 (2009).

[66] J. Klimeš, D. R. Bowler, and A. Michaelides. Van der Waals density functionals applied to solids. In: *Phys. Rev. B* **83**, p. 195131 (2011).

[67] J. Klimeš and A. Michaelides. Perspective: Advances and challenges in treating van der Waals dispersion forces in density functional theory. In: *The Journal of Chemical Physics* **137** (12), 120901 (2012).

[68] A. D. Becke. A new mixing of Hartree–Fock and local density-functional theories. In: *Journal of Chemical Physics* **98** (2), pp. 1372 (1993).

[69] J. Paier, M. Marsman, K. Hummer, G. Kresse, I. C. Gerber, and J. G. Ángyán. Screened hybrid density functionals applied to solids. In: *Journal of Chemical Physics* **124** (15), 154709 (2006).

[70] J. Paier, M. Marsman, K. Hummer, G. Kresse, I. C. Gerber, and J. G. Ángyán. Erratum: "Screened hybrid density functionals applied to solids" [J. Chem. Phys. 124, 154709 (2006)]. In: *Journal of Chemical Physics* **125** (24), 249901 (2006).

[71] M. J. Lucero, T. M. Henderson, and G. E. Scuseria. Improved semiconductor lattice parameters and band gaps from a middle-range screened hybrid exchange functional. In: *Journal of Physics: Condensed Matter* **24** (14), p. 145504 (2012).

[72] V. Dose. Momentum-resolved inverse photoemission. In: *Surface Science Reports* **5** (8), pp. 337 . ISSN 0167-5729 (1985).

[73] L. Yang, J. Deslippe, C.-H. Park, M. L. Cohen, and S. G. Louie. Excitonic Effects on the Optical Response of Graphene and Bilayer Graphene. In: *Phys. Rev. Lett.* **103**, p. 186802 (2009).

[74] O. Pulci. private communication.

[75] H. Ehrenreich and M. H. Cohen. Self-Consistent Field Approach to the Many-Electron Problem. In: *Phys. Rev.* **115** (4), p. 786 (1959).

[76] S. L. Adler. Quantum Theory of the Dielectric Constant in Real Solids. In: *Phys. Rev.* **126** (2), pp. 413 (1962).

[77] N. Wiser. Dielectric Constant with Local Field Effects Included. In: *Phys. Rev.* **129** (1), pp. 62 (1963).

[78] S. Baroni and R. Resta. Ab initio calculation of the macroscopic dielectric constant in silicon. In: *Phys. Rev. B* **33** (10), p. 7017 (1986).

[79] B. Adolph, V. I. Gavrilenko, K. Tenelsen, F. Bechstedt, and R. Del Sole. Nonlocality and many-body effects in the optical properties of semiconductors. In: *Phys. Rev. B* **53** (15), pp. 9797 (1996).

[80] M. Gajdoš, K. Hummer, G. Kresse, J. Furthmüller, and F. Bechstedt. Linear optical properties in the projector-augmented wave methodology. In: *Phys. Rev. B* **73** (4), p. 045112 (2006).

[81] G. B. Arfken and H. J. Weber. *Mathematical Methods for Physicists.* Elsevier (2005).

[82] I. J. Weinberg. Hilbert Transform by Numerical Integration. RADC-TR-79-3 In-House Report (1979).

[83] G. Kresse and J. Furthmüller. Efficient iterative schemes for ab initio total-energy calculations using a plane-wave basis set. In: *Phys. Rev. B* **54** (16), pp. 11169 (1996).

[84] G. Kresse and J. Furthmüller. Efficiency of ab-initio total energy calculations for metals and semiconductors using a plane-wave basis set. In: *Comp. Mater. Sci.* **6** (1), pp. 15 (1996).

[85] G. Kresse and D. Joubert. From ultrasoft pseudopotentials to the projector augmented-wave method. In: *Phys. Rev. B* **59** (3), pp. 1758 (1999).

[86] H. J. Monkhorst and J. D. Pack. Special points for Brillouin-zone integrations. In: *Phys. Rev. B* **13** (12), pp. 5188 (1976).

[87] P. Berning. Theory and Calculation of Optical Thin Films. In: G. Hass, editor, *Physics of Thin Films*, pp. 69–121. Academic Press, New York and London (1963).

[88] D. J. Griffiths and C. A. Steinke. Waves in locally periodic media. In: *American Journal of Physics* **69** (2), pp. 137 (2001).

[89] T. Zhan, X. Shi, Y. Dai, X. Liu, and J. Zi. Transfer matrix method for optics in graphene layers. In: *Journal of Physics: Condensed Matter* **25** (21), p. 215301 (2013).

[90] M. Kohmoto. Topological invariant and the quantization of the Hall conductance. In: *Annals of Physics* **160** (2), pp. 343 . ISSN 0003-4916 (1985).

[91] J. E. Avron, D. Osadchy, and R. Seiler. A Topological Look at the Quantum Hall Effect. In: *Physics Today* **56** (8), pp. 38 (2003).

[92] Y. Yao, L. Kleinman, A. H. MacDonald, J. Sinova, T. Jungwirth, D.-s. Wang, E. Wang, and Q. Niu. First Principles Calculation of Anomalous Hall Conductivity in Ferromagnetic bcc Fe. In: *Phys. Rev. Lett.* **92**, p. 037204 (2004).

[93] D. Xiao, M.-C. Chang, and Q. Niu. Berry phase effects on electronic properties. In: *Rev. Mod. Phys.* **82**, pp. 1959 (2010).

[94] M. Gradhand, D. V. Fedorov, F. Pientka, P. Zahn, I. Mertig, and B. L. Györffy. First-principle calculations of the Berry curvature of Bloch states for charge and spin transport of electrons. In: *Journal of Physics: Condensed Matter* **24** (21), p. 213202 (2012).

[95] J. E. Moore. The birth of topological insulators. In: *Nature* **464** (7286), pp. 194. ISSN 0028-0836 (2010).

[96] Y. Ando. Topological Insulator Materials. In: *Journal of the Physical Society of Japan* **82** (10), p. 102001 (2013).

[97] R. Yu, X. L. Qi, A. Bernevig, Z. Fang, and X. Dai. Equivalent expression of $\mathbb{Z}_2$ topological invariant for band insulators using the non-Abelian Berry connection. In: *Phys. Rev. B* **84**, p. 075119 (2011).

[98] A. A. Soluyanov and D. Vanderbilt. Computing topological invariants without inversion symmetry. In: *Phys. Rev. B* **83**, p. 235401 (2011).

[99] E. Prodan. Manifestly gauge-independent formulations of the $\mathbb{Z}_2$ invariants. In: *Phys. Rev. B* **83**, p. 235115 (2011).

[100] H. Zhang and S.-C. Zhang. Topological insulators from the perspective of first-principles calculations. In: *physica status solidi (RRL) - Rapid Research Letters* **7** (1-2), pp. 72. ISSN 1862-6270 (2013).

[101] L. Fu and C. L. Kane. Topological insulators with inversion symmetry. In: *Phys. Rev. B* **76**, p. 045302 (2007).

[102] F. Bechstedt. *Principles of Surface Physics*. Springer-Verlag, Berlin (2003).

[103] P. Pflugradt, L. Matthes, and F. Bechstedt. Silicene-derived phases on Ag(111) substrate versus coverage: *Ab initio* studies. In: *Phys. Rev. B* **89**, p. 035403 (2014).

[104] P. Pflugradt, L. Matthes, and F. Bechstedt. Silicene on metal and metallized surfaces: ab initio studies. In: *New Journal of Physics* **16** (7), p. 075004 (2014).

[105] P. Pflugradt, L. Matthes, and F. Bechstedt. Unexpected symmetry and AA stacking of bilayer silicene on Ag(111). In: *Phys. Rev. B* **89**, p. 205428 (2014).

[106] S. Kokott, L. Matthes, and F. Bechstedt. Silicene on hydrogen-passivated Si(111) and Ge(111) substrates. In: *physica status solidi (RRL) - Rapid Research Letters* **7** (8), pp. 538. ISSN 1862-6270 (2013).

[107] S. Kokott, P. Pflugradt, L. Matthes, and F. Bechstedt. Nonmetallic substrates for growth of silicene: an ab initio prediction. In: *Journal of Physics: Condensed Matter* **26** (18), p. 185002 (2014).

[108] A. H. Castro Neto, F. Guinea, N. M. R. Peres, K. S. Novoselov, and A. K. Geim. The electronic properties of graphene. In: *Rev. Mod. Phys.* **81** (1), pp. 109 (2009).

[109] T. Terzibaschian and B. Enderlein. The irreducible representations of the two-dimensional space groups of crystal surfaces. Theory and applications. In: *physica status solidi (b)* **133** (2), pp. 443. ISSN 1521-3951 (1986).

[110] R. Saito, G. Dresselhaus, and M. S. Dresselhaus. *Physical Properties of Carbon Nanotubes.* Imperial College Press (1998).

[111] S. Reich, J. Maultzsch, C. Thomsen, and P. Ordejón. Tight-binding description of graphene. In: *Phys. Rev. B* **66** (3), p. 035412 (2002).

[112] G. G. Guzmán-Verri and L. C. Lew Yan Voon. Electronic structure of silicon-based nanostructures. In: *Phys. Rev. B* **76** (7), p. 075131 (2007).

[113] C. Bena and G. Montambaux. Remarks on the tight-binding model of graphene. In: *New Journal of Physics* **11** (9), p. 095003 (2009).

[114] N. M. R. Peres. The transport properties of graphene. In: *Journal of Physics: Condensed Matter* **21** (32), p. 323201 (2009).

[115] L. Matthes. *Zur theoretischen Beschreibung eindimensionaler Strukturen.* Master's thesis, University of Jena (2010).

[116] C.-C. Liu, H. Jiang, and Y. Yao. Low-energy effective Hamiltonian involving spin-orbit coupling in silicene and two-dimensional germanium and tin. In: *Phys. Rev. B* **84**, p. 195430 (2011).

[117] M. Ezawa. A topological insulator and helical zero mode in silicene under an inhomogeneous electric field. In: *New Journal of Physics* **14** (3), p. 033003 (2012).

[118] K. Parlinski, Z. Li, and Y. Kawazoe. First-Principles Determination of the Soft Mode in Cubic ZrO_2. In: *Phys. Rev. Lett.* **78**, pp. 4063 (1997).

[119] A. Togo, F. Oba, and I. Tanaka. First-principles calculations of the ferroelastic transition between rutile-type and CaCl2-type SiO2 at high pressures. In: *Phys. rev. B* **78**, p. 134106 (2008).

[120] B. van den Broek, M. Houssa, E. Scalise, G. Pourtois, V. V. Afanaas'ev, and A. Stesmans. Two-dimensional hexagonal tin: ab initio geometry, stability, electronic structure and functionalization. In: *2D Materials* **1** (2), p. 021004 (2014).

[121] P. Rivero, J.-A. Yan, V. M. Garcia-Suarez, J. Ferrer, and S. Barraza-Lopez. Stability and properties of high-buckled two-dimensional tin and lead. In: *ArXiv e-prints* (2014).

[122] S. Lebègue and O. Eriksson. Electronic structure of two-dimensional crystals from *ab initio* theory. In: *Phys. Rev. B* **79**, p. 115409 (2009).

[123] L. C. Lew Yan Voon, E. Sandberg, R. S. Aga, and A. A. Farajian. Hydrogen compounds of group-IV nanosheets. In: *Appl. Phys. Lett.* **97** (16), 163114 (2010).

[124] T. H. Osborn, A. A. Farajian, O. V. Pupysheva, R. S. Aga, and L. L. Y. Voon. Ab initio simulations of silicene hydrogenation. In: *Chemical Physics Letters* **511** (1–3), pp. 101 . ISSN 0009-2614 (2011).

[125] E. Scalise, M. Houssa, G. Pourtois, B. van den Broek, V. Afanas'ev, and A. Stesmans. Vibrational properties of silicene and germanene. In: *Nano Research* **6** (1), pp. 19. ISSN 1998-0124 (2013).

[126] N. J. Roome and J. D. Carey. Beyond Graphene: Stable Elemental Monolayers of Silicene and Germanene. In: *ACS Applied Materials & Interfaces* **6** (10), pp. 7743. PMID: 24724967 (2014).

[127] P. Blöchl, O. Jepsen, and O. Andersen. Improved tetrahedron method for Brillouin-zone integrations. In: *Phys. Rev. B* **49**, pp. 16223 (1994).

[128] E. Kogan. Symmetry Classification of Energy Bands in Graphene and Silicene. In: *Graphene* **2**, pp. 74 (2013).

[129] N. D. Drummond, V. Zólyomi, and V. I. Fal'ko. Electrically tunable band gap in silicene. In: *Phys. Rev. B* **85**, p. 075423 (2012).

[130] Y. A. Bychkov and E. I. Rashba. Oscillatory effects and the magnetic susceptibility of carriers in inversion layers. In: *Journal of Physics C: Solid State Physics* **17** (33), p. 6039 (1984).

[131] G. Dresselhaus. Spin-Orbit Coupling Effects in Zinc Blende Structures. In: *Phys. Rev.* **100**, pp. 580 (1955).

[132] M. Dyakonov and V. Kachorovskii. Spin relaxation of two-dimensional electrons in noncentrosymmetric semiconductors. In: *Sov. Phys. Semicond* **20** (1), pp. 110 (1986).

[133] L. Stille, C. J. Tabert, and E. J. Nicol. Optical signatures of the tunable band gap and valley-spin coupling in silicene. In: *Phys. Rev. B* **86**, p. 195405 (2012).

[134] M. Ezawa. Spin-valley optical selection rule and strong circular dichroism in silicene. In: *Phys. Rev. B* **86**, p. 161407 (2012).

[135] C. L. Kane and E. J. Mele. Quantum Spin Hall Effect in Graphene. In: *Phys. Rev. Lett.* **95**, p. 226801 (2005).

[136] O. Pulci and F. Bechstedt. "private communication".

[137] D. Jérome, T. M. Rice, and W. Kohn. Excitonic Insulator. In: *Phys. Rev.* **158**, pp. 462 (1967).

[138] K. F. Mak, M. Y. Sfeir, Y. Wu, C. H. Lui, J. A. Misewich, and T. F. Heinz. Measurement of the Optical Conductivity of Graphene. In: *Phys. Rev. Lett.* **101**, p. 196405 (2008).

[139] B. Adolph, J. Furthmüller, and F. Bechstedt. Optical properties of semiconductors using projector-augmented waves. In: *Phys. Rev. B* **63** (12), p. 125108 (2001).

[140] A. Grüneis, R. Saito, G. G. Samsonidze, T. Kimura, M. A. Pimenta, A. Jorio, A. G. S. Filho, G. Dresselhaus, and M. S. Dresselhaus. Inhomogeneous optical absorption around the K point in graphite and carbon nanotubes. In: *Phys. Rev. B* **67**, p. 165402 (2003).

[141] P. Yu and M. Cardona. *Fundamentals of Semiconductors*. Springer, Berlin (1996).

[142] M. Lewkowicz and B. Rosenstein. Dynamics of Particle-Hole Pair Creation in Graphene. In: *Phys. Rev. Lett.* **102**, p. 106802 (2009).

[143] T. Stauber, N. M. R. Peres, and A. K. Geim. Optical conductivity of graphene in the visible region of the spectrum. In: *Phys. Rev. B* **78**, p. 085432 (2008).

[144] K. F. Mak, L. Ju, F. Wang, and T. F. Heinz. Optical spectroscopy of graphene: From the far infrared to the ultraviolet. In: *Solid State Communications* **152** (15), pp. 1341 . ISSN 0038-1098 (2012).

[145] E. Hecht. *Optics.* Addison-Wesley (2001).

[146] F. Bechstedt and R. Enderlein. Inverse dielectric function of a superlattice including local field effects and spatial dispersion. In: *Superlattices and Microstructures* **2** (6), pp. 543 . ISSN 0749-6036 (1986).

[147] U. Wurstbauer, C. Röling, U. Wurstbauer, W. Wegscheider, M. Vaupel, P. H. Thiesen, and D. Weiss. Imaging ellipsometry of graphene. In: *Applied Physics Letters* **97** (23), 231901 (2010).

[148] O. Leenaerts, H. Peelaers, A. D. Hernández-Nieves, B. Partoens, and F. M. Peeters. First-principles investigation of graphene fluoride and graphane. In: *Phys. Rev. B* **82**, p. 195436 (2010).

[149] O. Pulci, P. Gori, M. Marsili, V. Garbuio, R. D. Sole, and F. Bechstedt. Strong excitons in novel two-dimensional crystals: Silicane and germanane. In: *EPL (Europhysics Letters)* **98** (3), p. 37004 (2012).

[150] Q. Zhang, Y. Cheng, and U. Schwingenschlögl. Series of topological phase transitions in TiTe$_2$ under strain. In: *Phys. Rev. B* **88**, p. 155317 (2013).

[151] F. Geissler, J. C. Budich, and B. Trauzettel. Group theoretical and topological analysis of the quantum spin Hall effect in silicene. In: *New Journal of Physics* **15** (8), 085030 (2013).

[152] L. Winterfeld, L. A. Agapito, J. Li, N. Kioussis, P. Blaha, and Y. P. Chen. Strain-induced topological insulator phase transition in HgSe. In: *Phys. Rev. B* **87**, p. 075143 (2013).

[153] L. Seixas, J. E. Padilha, and A. Fazzio. Quantum spin Hall effect on germanene nanorod embedded in completely hydrogenated germanene. In: *Phys. Rev. B* **89**, p. 195403 (2014).

[154] C. Si, J. Liu, Y. Xu, J. Wu, B.-L. Gu, and W. Duan. Functionalized germanene as a prototype of large-gap two-dimensional topological insulators. In: *Phys. Rev. B* **89**, p. 115429 (2014).

[155] P. Tang, P. Chen, W. Cao, H. Huang, S. Cahangirov, L. Xian, Y. Xu, S.-C. Zhang, W. Duan, and A. Rubio. Stable two-dimensional dumbbell stanene: A quantum spin Hall insulator. In: *Phys. Rev. B* **90**, p. 121408 (2014).

[156] Y.-L. Song, Y. Zhang, J.-M. Zhang, and D.-B. Lu. Effects of the edge shape and the width on the structural and electronic properties of silicene nanoribbons. In: *Applied Surface Science* **256** (21), pp. 6313 . ISSN 0169-4332 (2010).

[157] M. Ezawa. Peculiar width dependence of the electronic properties of carbon nanoribbons. In: *Phys. Rev. B* **73**, p. 045432 (2006).

[158] U. Treske, F. Ortmann, B. Oetzel, K. Hannewald, and F. Bechstedt. Electronic and transport properties of graphene nanoribbons. In: *physica status solidi (a)* **207** (2), pp. 304. ISSN 1862-6319 (2010).

[159] M. Fujita, K. Wakabayashi, K. Nakada, and K. Kusakabe. Peculiar Localized State at Zigzag Graphite Edge. In: *Journal of the Physical Society of Japan* **65** (7), pp. 1920 (1996).

[160] S. Ryu and Y. Hatsugai. Topological Origin of Zero-Energy Edge States in Particle-Hole Symmetric Systems. In: *Phys. Rev. Lett.* **89**, p. 077002 (2002).

[161] T. Li, M. Lin, S. Chang, and T. Lin. Electronic properties of bearded graphene nanoribbons. In: *Journal of Physics and Chemistry of Solids* **73** (10), pp. 1245 . ISSN 0022-3697 (2012).

[162] Y.-W. Son, M. L. Cohen, and S. G. Louie. Energy Gaps in Graphene Nanoribbons. In: *Phys. Rev. Lett.* **97**, p. 216803 (2006).

[163] Y.-W. Son, M. L. Cohen, and S. G. Louie. Half-metallic graphene nanoribbons. In: *Nature* **444** (7117), pp. 347 (2006).

[164] J. Bundesmann, M.-H. Liu, i. d. I. m. c. Adagideli, and K. Richter. Spin conductance of diffusive graphene nanoribbons: A probe of zigzag edge magnetization. In: *Phys. Rev. B* **88**, p. 195406 (2013).

[165] Q. Pang, Y. Zhang, J.-M. Zhang, V. Ji, and K.-W. Xu. Electronic and magnetic properties of pristine and chemically functionalized germanene nanoribbons. In: *Nanoscale* **3**, pp. 4330 (2011).

[166] N. B. Le, T. D. Huan, and L. M. Woods. Tunable Spin-Dependent Properties of Zigzag Silicene Nanoribbons. In: *Phys. Rev. Applied* **1**, p. 054002 (2014).

[167] Z. Ni, Q. Liu, K. Tang, J. Zheng, J. Zhou, R. Qin, Z. Gao, D. Yu, and J. Lu. Tunable Bandgap in Silicene and Germanene. In: *Nano Letters* **12** (1), pp. 113 (2012).

[168] W.-F. Tsai, C.-Y. Huang, T.-R. Chang, H. Lin, H.-T. Jeng, and A. Bansil. Gated silicene as a tunable source of nearly 100% spin-polarized electrons. In: *Nat Commun* **4**, p. 1500 (2013).

[169] H. Enriquez, S. Vizzini, A. Kara, B. Lalmi, and H. Oughaddou. Silicene structures on silver surfaces. In: *Journal of Physics: Condensed Matter* **24** (31), p. 314211 (2012).

[170] W. Mönch. *Semiconductor Surfaces and Interfaces*. Springer, Berlin (2001).

[171] J. O. Hauch, M. Fonine, U. May, R. Calarco, H. Kittur, J. M. Choi, U. Rüdiger, and G. Güntherodt. The Growth of Transition Metals on H-Passivated Si(111) Substrates. In: *Advanced Functional Materials* **11** (3), pp. 179. ISSN 1616-3028 (2001).

[172] K. Novoselov. Graphene: Mind the gap. In: *Nat Mater* **6** (10), pp. 720 (2007).

[173] J. J. Boland and J. S. Villarrubia. Formation of Si(111)-(1×1)Cl. In: *Phys. Rev. B* **41**, pp. 9865 (1990).

[174] P. W. Tasker. The stability of ionic crystal surfaces. In: *Journal of Physics C: Solid State Physics* **12**, p. 4977 (1979).

[175] A. Koma. Van der Waals epitaxy – a new epitaxial growth method for a highly lattice-mismatched system. In: *Thin Solid Films* **216** (1), pp. 72 . ISSN 0040-6090. Papers presented at the International Workshop on Science and Technology of Thin Films for the 21st Century, Evanston,IL, USA, July 28-August 2, 1991 (1992).

[176] K. Saiki, Y. Sato, and A. Koma. Adsorption of Oxygen on Electron-Bombarded CaF$_2$(111) Surfaces. In: *Japanese Journal of Applied Physics* **28** (1A), p. L134 (1989).

Danksagung

An dieser Stelle möchte ich mich insbesondere bei Prof. Friedhelm Bechstedt für die exzellente Betreuung meiner Dissertation bedanken. Seine Unterstützung, sein Engagement, seine Kompetenz und sein Verständnis sowohl in fachlicher als auch in privater Hinsicht waren stets vorbildlich und werden mir immer in sehr guter Erinnerung bleiben. Die anregenden Diskussionen mit ihm über die Physik der zweidimensionalen Systeme haben zweifelsohne maßgeblich zum Erfolg der Promotion beigetragen.

Des Weiteren möchte ich mich bei Prof. Olivia Pulci und ihrem Mann Prof. Wolfgang Richter bedanken, die mich beide bei meinem einjährigen Aufenthalt in Rom sowohl in größtem Maße gefördert, ausgebildet und integriert haben, mit aber vor allem auch stets bei allen Problemen mit viel Engagement zur Seite standen. Für die immer noch andauernde erfolgreiche Kollaboration mit Prof. Olivia Pulci bin ich sehr dankbar.

Ich möchte mich bei Dr. Karsten Hannewald sowohl für seine Unterstützung bei der Bewerbung um das Carl-Zeiss-Stipendium als auch für seine kompetente Betreuung bedanken.

Mein Dank gilt auch meinen Arbeitskollegen für die stets anregenden Diskussionen und die angenehme Arbeitsatmosphäre. Hervorheben möchte ich meinen Kollegen Sebastian Küfner und meine beiden Masterstudenten Sebastian Kokott und Paul Pflugradt, mit deren Hilfe weitere interessante Fragestellungen, die im Rahmen dieser Arbeit aufgetreten sind, gemeinsam effizient bearbeitet werden konnten.

Besonderer Dank gilt meiner Familie und meiner Freundin für ihr Verständnis und ihre Unterstützung.

Abschließend danke ich der Carl-Zeiss-Stiftung für ihre finanzielle Unterstützung.

THESEN

1. Die Ladungsträger der zweidimensionalen (2D) Gruppe-IV-Honigwabenkristalle Graphene, Silicene, Germanene und Stanene verhalten sich näherungsweise wie masselose Spin-1/2 Teilchen in Dirac Bändern nahe der K- und K'-Punkte der hexagonalen Brillouin-Zone.

2. Die strukturellen, elektronischen und optischen Eigenschaften lassen sich mit Hilfe der Dichtefunktionaltheorie (DFT) sehr gut beschreiben und liefern im Vergleich mit Experimenten erstaunlich genaue Vorhersagen. Quasiteilchenkorrekturen können näherungsweise mit Hilfe eines Hybridfunktionals simuliert werden.

3. Die optische Reflexion, Transmission und Absorption zweidimensionaler Kristalle hängt allein von den Komponenten des i.A. anisotropen, frequenzabhängigen Leitfähigkeitstensors ab. Dieser kann im Rahmen der unabhängigen Quasiteilchenapproximation sehr genau bestimmt werden.

4. Ohne Berücksichtigung der Spin-Bahn-Kopplung zeigt sich für alle Gruppe-IV-Honigwabenkristalle eine universelle Infrarotabsorption von 2.3% völlig unabhängig von dem Buckling der 2D Kristalle, ihrer sp^2/sp^3-Bindung, der elektronischen Struktur, und dem verwendeten Austausch-Korrelations-Potential. Das Resultat ist gültig über einen weiten Frequenzbereich, der aber entlang der Reihe C→Si→Ge→Sn reduziert wird.

5. Unter Berücksichtigung der Spin-Bahn-Kopplung kann sowohl numerisch als auch analytisch gezeigt werden, dass eine Absorption von 4.6% in der Nähe der fundamentalen Absorptionskante erreicht werden kann.

6. Silicene, Germanene und Stanene gehören zur Gruppe der topologischen Isolatoren. Die zugehörige topologische Invariante ($\mathbb{Z}_2$ Index) kann direkt aus der mit Spin-Bahn Wechselwirkung berechneten Bandstrukturen über die Methode der Evolution von Wannier Ladungszentren bestimmt werden. Unter dem Einfluss eines homogenen elektrischen Feldes zeigt sich ein Phasenübergang zu einem trivialen Isolator.

7. An der Oberfläche der entsprechenden Nanoribbons entstehen metallische Oberflächenzustände, die allerdings nicht die erwartete lineare Dispersion eines topologischen Zustandes zeigen, sondern durch den Rashba-Effekt modifiziert sind.

8. Die Funktionalisierung der 2D-Honigwabenkristalle mit Halogeniden führt zu idealen topologischen Isolatoren, sofern die entstehende Bandlücke klein ist.

9. Im Gegensatz zu Graphit existiert in der Natur kein vergleichbarer geschichteter Kristall auf Siliziumbasis. Die Herstellung von Silicene ist daher eine Herausforderung. Epitaktisches Wachstum von Silicene auf Ag(111) zerstört die Symmetrie des Honigwabenkristalls und damit auch dessen einzigartige Eigenschaften. Neue gitterangepasste isolierende Substrate mit schwacher van der Waals Bindung bieten eine alternative Möglichkeit des epitaktischen Wachstums von Silicene.

Ehrenwörtliche Erklärung

Ich erkläre hiermit ehrenwörtlich, dass ich die vorliegende Arbeit selbständig, ohne unzulässige Hilfe Dritter und ohne Benutzung anderer als der angegebenen Hilfsmittel und Literatur angefertigt habe. Die aus anderen Quellen direkt oder indirekt übernommenen Daten und Konzepte sind unter Angabe der Quelle gekennzeichnet.

Bei der Auswahl und Auswertung folgenden Materials haben mir die nachstehend aufgeführten Personen in der jeweils beschriebenen Weise unentgeltlich geholfen:

1. Dipl.-Phys. Sebastian Küfner durch die gemeinsame Bearbeitung der in den Abschnitten 1.7, 3.1 und 3.2.2 dargestellten Fragestellungen,

2. Dipl.-Phys. Sebastian Kokott im Rahmen seiner unter meiner Betreuung angefertigten Masterarbeit, durch die gemeinsame Bearbeitung der in den Abschnitten 4.2 und 4.3 dargestellten Fragestellungen,

3. Dipl.-Phys. Paul Pflugradt im Rahmen seiner unter meiner Betreuung angefertigten Masterarbeit, durch die gemeinsame Bearbeitung der in den Abschnitten 4.1 dargestellten Fragestellungen,

4. Prof. Dr. sc. nat. Friedhelm Bechstedt als betreuender Hochschullehrer.

Weitere Personen waren an der inhaltlich-materiellen Erstellung der vorliegenden Arbeit nicht beteiligt. Insbesondere habe ich hierfür nicht die entgeltliche Hilfe von Vermittlungs- bzw. Beratungsdiensten (Promotionsberater oder andere Personen) in Anspruch genommen. Niemand hat von mir unmittelbar oder mittelbar geldwerte Leistungen für Arbeiten erhalten, die im Zusammenhang mit dem Inhalt der vorgelegten Dissertation stehen.

Die Arbeit wurde bisher weder im In- noch im Ausland in gleicher oder ähnlicher Form einer anderen Prüfungsbehörde vorgelegt.

Die geltende Promotionsordnung der Physikalisch-Astronomischen Fakultät ist mir bekannt.

Ich versichere ehrenwörtlich, dass ich nach bestem Wissen die reine Wahrheit gesagt und nichts verschwiegen habe.

Jena, den 15. März 2015   ....

Lebenslauf

Persönliche Daten

Name	Matthes
Vorname	Lars
Geburtsdatum	17.02.1986
Geburtsort	Zwickau
Nationalität	Deutsch
Familienstand	ledig

Ausbildung

1992-1996	Grundschule Glauchau-Rothenbach
1996-2004	Georgius-Agricola-Gymnasium Glauchau
2004	Abitur (Abschluss: 1,3 mit Auszeichnung)
10/2005-09/2010	Stipendiat der "Stiftung in memoriam Rudolf Felix Weissbach", Physikstudium, Friedrich-Schiller-Universität Jena
29.09.2010	Physik Diplom, Friedrich-Schiller-Universität Jena Abschluss: 1,0 mit Auszeichnung
10/2010-01/2011	Wissenschaftlicher Mitarbeiter am Institut für Festkörpertheorie und -optik an der Friedrich-Schiller-Universität Jena
01/2011-02/2012	Stipendiat der Marie-Curie Stiftung im Projekt CLERMONT4, wissenschaftlicher Mitarbeiter am Institut "Teorie di Fisica della materia", Universität "Tor Vergata", Rom (Italien)
seit 03/2012	Stipendiat der Carl-Zeiss-Stiftung zur Promotion am Institut für Festkörpertheorie und -optik an der Friedrich-Schiller-Universität Jena

Jena, den 15. März 2015 ....